Università degli Studi di Napoli "Federico II"

Scuola Politecnica e delle Scienze di Base

Ph.D. Thesis

Doctoral Programme

in

Industrial Engineering

Ultralight Radar Sensor for Autonomous Operations by Mini- and Micro-UAS

Supervisors

Prof. A. Moccia

Prof. A. Renga

Candidate

Antonio Fulvio Scannapieco

April 2017

Allons-y!

Abstract

In recent years the boost in operations by mini- and micro-UAS (Unmanned Aircraft Systems, also known as Remotely Piloted Aircraft Systems - RPAS - or simply drones) and the successful miniaturization of electronic components were experienced. Radar sensors demonstrated to have favorable features for these operations. However, despite their ability to provide meaningful information for navigation, sense-and-avoid, and imaging tasks, currently very few radar sensors are exploited onboard or developed for autonomous operations with mini- and micro-UAS. Exploration of indoor complex, dangerous, and not easily accessible environments represents a possible application for mini-UAS based on radar technology. In this scenario, the objective of the thesis is to develop design strategies and processing approaches for a novel ultralight radar sensor able to provide the miniaturized platform with Simultaneous Localization and Mapping (SLAM) capabilities, mainly but not exclusively indoors. Millimeter-wave Interferometric Synthetic Aperture Radar (mmw InSAR) technology has been identified as a key asset. At the same time, testing of commercial lightweight radar is carried out to assess potentialities towards autonomous navigation, sense-and-avoid, and imaging. The two main research lines can be outlined as follows:

Long-term scenario: Development of very compact and ultralight Synthetic Aperture Radar able to provide mini- or micro-UAS with very accurate 3D awareness in indoor or GPS-denied complex and harsh environments.

Short-term scenario: Assessment of true potentialities of current commercial radar sensors in a UAS-oriented scenario.

Within the framework of long-term scenario, after a review of state-of-art SAR sensors, Frequency-Modulated Continuous Wave (FMCW) SAR technology has

been selected as preferred candidate. Design procedure tailored to this technology and software simulator for operations have been developed in MATLAB environment. Software simulator accounts for the analysis of ambiguous areas in a three-dimensional environment, different SAR focusing algorithms, and a Ray-Tracing algorithm specifically designed for indoor operations. The simulations provided relevant information on actual feasibility of the sensor, as well as mission design characteristics. Additionally, field tests have been carried out at Fraunhofer Institute FHR with a mmw SAR. Processing approaches developed from simulations proved to be effective when dealing with field tests. A very lightweight FMCW radar sensor manifactured by IMST GmbH has been tested for short-term scenario operations. The codes for data acquisition were developed in Python language both for Windows-based and GNU/Linux-based operative systems. The radar provided information on range and angle of targets in the scene, thus being interesting for radar-aided UAS navigation. Multiple-target tracking and radar odometry algorithms have been developed and tested on actual field data. Radar-only odometry provided to be effective under specific circumstances.

Contents

1 Introduction **1**

1.1 Applications of radar technology to mini- and micro-UAS 2

1.1.1 Practical application 7

1.2 Scope and aims 9

2 mm-wave InSAR design **13**

2.1 System Architecture 13

2.1.1 State-of-the-Art Analysis 13

2.1.2 Why MMW 16

2.1.3 Why FMCW SAR 17

2.1.4 Why SAR Interferometry 23

2.1.5 Selected Scheme 23

2.2 Preliminary System Design 25

2.2.1 Ambiguities and Antenna Width 27

2.2.2 Transmitted Power 28

2.2.3 Interferometry 29

2.2.4 Design configuration 34

3 mm-wave InSAR simulation **37**

3.1 Simulation Environment 37

3.2 Scene Generation 42

3.2.1 Point Target 42
3.2.2 Ray-Tracing 44
3.3 Processing 52
3.3.1 Time-domain algorithms 53
3.3.2 Frequency-domain Algorithms 56
3.4 Assessment of Three-Dimensional Mapping Capabilities 59
3.4.1 Geometric Model 60
3.5 Results 62
3.5.1 Focusing 67
3.5.2 Ray-Tracing 69
3.5.3 Ambiguous Areas 78

4 mm-wave SAR testing 83
4.1 94 GHz SAR 83
4.2 Inertial Measurement Units 85
4.3 Results 88
4.3.1 First campaign 88
4.3.2 Second Campaign 93

5 Commercial ultralight radar sensor 98
5.1 24-GHz SENTIRE Radar 98
5.2 Characterization 102
5.3 Tests and Results 103
5.3.1 Sensing performance 103
5.3.2 Imaging 111

6 Radar Odometry 115
6.1 Radar-aided Navigation 115
6.2 Target Detection 121

6.2.1 Range-Bearing Estimation 121
6.2.2 CFAR Detector 125
6.3 Multiple-Target Tracking 130
6.3.1 Global Nearest Neighbor 130
6.3.2 Track Handling 131
6.3.3 Extended Kalman Filter 133
6.4 Radar Odometry 136
6.5 Experimental Results and Validation 137
6.5.1 Operative setup and scene 137
6.5.2 Target Detection 140
6.5.3 Multiple-Target Tracking 143
6.5.4 Radar Odometry 146
6.5.5 Real-Time Capabilities 149

7 Conclusions **152**

Bibliography **156**

List of Figures

2.1 Comparison between *PRI* (a) in FMCW SAR and (b) in conventional pulsed SAR. Plots not to scale for clarity. 20

2.2 System architecture. 24

2.3 Design process guidelines: block diagram. 26

2.4 FMCW ambiguity in range: first sweep reflection from furthest target (red line) is between transmitted signal (black line) and second sweep reflection from closest target (blue line) so that furthest target is imaged closer. 28

2.5 Interferometric observation geometry. 30

2.6 Percentage error between true and approximated differential interferometric phase under various operating conditions (the three curves correspond to $\theta = 15°$, $\theta = 45°$, $\theta = 75°$). 32

2.7 Critical baseline for various operating conditions. For each plot $dr =$ 10 cm and $\Delta h = 10$ cm have been considered. 33

2.8 Effect of height variation on critical baseline. For each plot $dr = 10$ cm has been considered. 35

3.1 Block scheme for software system simulator. 39

3.2 3D view of analyzed scenario. 40

3.3 Platform and sensor moving in simplified operational scenario. Platform and target position vectors, line of sight unit vector, velocity vector, and target distance to antennas are depicted, too. Dimensions are not to scale for clarity. 41
3.4 Reference frames and rotations. 43
3.5 Schematic of 2D grid values. Areas associated to value 0 represent the propagating medium; cells having values ranging from 1 to 8 are the walls. Receiving antenna is represented by value 9. Size of cells is not to scale for clarity. 47
3.6 Example of reflections due to an object (rectangle, bold) in the scene. Position of antennas is revealed by black circle. 47
3.7 2D geometry: example of rays intercepted by receiving antenna. Transmitting and receiving antennas are oriented towards the bottom-right corner and gray circle shows their location. Blue dotted and red dashed rays indicate the borders of transmitted beam, whereas inner rays are depicted in black. The energy is reflected back to both the antenna and the top-left corner: some rays hit the antennas, hence they are not propagated towards the top-left side of the grid (transparent area). The figure represents a detail of the total grid. 48
3.8 3D view of reflected rays: black dot represents the position of antennas, blue crosses are the points where reflection occurs. Only a small part of the whole control volume is shown, for clarity. 52
3.9 Point Target Response for a 30° squint angle straight trajectory: BPA 63
3.10 Fluctuating target: examples of amplitude and phase distribution. . . 65
3.11 BPA -10 dB range. 5 realizations. Nominal condition, i.e. point target on absorbing background, in thick black line. 65
3.12 BPA -10 dB azimuth. 5 realizations. Nominal condition, i.e. point target on absorbing background, in thick black line. 66
3.13 *Target 1*: $\mathbf{P_1} = [15.00, 7.79, 0.00]$ (m); *Target 2*: $\mathbf{P_2} = [14.85, 7.65, 0.00]$ (m) 68
3.14 *Target 1*: $\mathbf{P_1} = [15.00, 7.79, 0.00]$ (m); *Target 2*: $\mathbf{P_2} = [14.75, 7.55, 0.50]$ (m) 69

3.15 Example of images for different heights of antennas. *Target 1*: $\mathbf{P_1} = [15.00, 7.79, 0.00]\,(\mathrm{m})$; *Target 2*: $\mathbf{P_2} = [14.75, 7.55, 0.50]\,(\mathrm{m})$ 70

3.16 *Target 1*: $\mathbf{P_1} = [15.00, 7.79, 0.00]\,(\mathrm{m})$; *Target 2*: $\mathbf{P_2}\,(t_N = 0\mathrm{s}) = [14.75, 7.55, 0.50]\,(\mathrm{m}) - \mathbf{v_2} = [1.000, 0.373, -0.100]\,(\mathrm{m\,s^{-1}})$ 71

3.17 *Target 1*: $\mathbf{P_1} = [15.00, 7.79, 0.00]\,(\mathrm{m})$; *Target 2*: $\mathbf{P_2}\,(t_N = 0\mathrm{s}) = [14.75, 7.55, 0.50]\,(\mathrm{m})$ 72

3.18 Case 1: observation of edge without reflections impinging on antenna. (a) radar echoes due to backscattering only, after FFT; (b) difference between radar echoes due to both reflections and backscattering and echoes due to backscattering, after FFT; (c) ray geometry, with magnified area highlighted in black; (d) magnification of ray geometry. . . 73

3.19 Case 2: observation of edge with reflected rays incident on antenna. (a) radar echoes due to backscattering only, after FFT; (b) difference between radar echoes due to both reflections and backscattering and echoes due to backscattering, after FFT; (c) ray geometry, with magnified area highlighted in black; (d) magnification of ray geometry and position of antenna (black circle). 75

3.20 Dihedral corner observation. Illuminated area at a certain point and time during trajectory. Thick dotted lines indicates the illuminated areas during trajectory. 76

3.21 Focused image for dihedral corner observation. 77

3.22 Trihedral corner observation. Thick black lines represent two additional edges seen during observation. Thick dotted lines indicates the illuminated areas during trajectory. 77

3.23 Case 2: observation of edge with reflected rays incident on antenna. (a) radar echoes due to backscattering only, after FFT; (b) difference between radar echoes due to both reflections and backscattering and echoes due to backscattering, after FFT; (c) ray geometry, with magnified area highlighted in black; (d) magnification of ray geometry and position of antenna (black circle). 79

3.24 Plane OAED. Ambiguous area (shaded) and contributions: intersection angle (green contour), resolution (blue contour), and pixel size (red contour). For clarity, the distance between two close isolines does not represent true system resolution. 82
3.25 Total unambiguous area (in red, about 47% of control volume surface) for position and velocity reported in Table 3.7. Not observable walls are not depicted in figure. 82

4.1 Assembly of FHR's 94 GHz SAR. 84
4.2 Envisaged flight geometry. 85
4.3 Schematics for decoding data from DJI A2 Controller. 86
4.4 First campaign. Track and scenery. 89
4.5 View of test site. Red line represents the rail. Courtesy of Google Maps. 90
4.6 Projections of trajectory in North-East-Down reference frame. IMU data in red, GPS data in blue. 92
4.7 Visual outputs of data from Teensy. 92
4.8 Full Scene RDA. 93
4.9 Single CR RDA Focusing. 93
4.10 Two CRs RDA Focusing. 94
4.11 Second campaign. 95
4.12 View of test site. Red line represents the path of the van. Courtesy of Google Maps. 95
4.13 View of the scene. 96
4.14 Full Scene BPA. 97

5.1 Assembly of SENTIRE Radar front-end and patch antennas. 99
5.2 Reference frame for radar sensor. 101
5.3 Unambiguous bearing angle interval as function of receivers separation L. In black, unambiguous bearing interval for SENTIRE Radar. . . . 101
5.4 -3dB decay (top left - red line) and bearing angle (bottom left - red box) for CR at $y = 2.00$m. On the right: magnification. 104

5.5 -3dB decay (top left - red line) and bearing angle (bottom left - red box) for CR at $y = 5.00$m. On the right: magnification. 104
5.6 Identification of two close targets (red) in the scene. Normalized magnitude and bearing angle as function of range (left), magnification (right). 105
5.7 Range, magnitude and bearing angle for the three brightest targets at each acquisition time. The scene contains only flying quadrotor. . . . 106
5.8 Magnitude (left) and bearing angle (right) as function of time and range for a scene containing a CR and a quadrotor. 106
5.9 Experimental setup with flying quadrotor. 107
5.10 Magnitude of range compressed data showing the motion of quadrotor.. 107
5.11 Range, magnitude and bearing angle for the three brightest targets at each acquisition time. The scene contains only flying quadrotor. . . . 108
5.12 Magnitude and Bearing angle as function of time and range for a complex scene containing a CR and man-made objects. White and black boxes indicate phases of platform motion. 109
5.13 Magnitude and Bearing angle as function of time and range for a complex scene containing a CR and man-made objects. White and black boxes indicate phases of platform motion. 112
5.14 Range and bearing angle information for the targets extracted at each acquisition time by means of CFAR algorithm (in black). Confirmed tracks representing relative motion of CR are depicted in blue. Baseline history provided by GPS is depicted in red. 113
5.15 Magnitude of range-compressed matrix resulting from straight motion of trihedral CR. 113
5.16 Measurements for motion of CR. From top to bottom: range, range rate, Doppler frequency, bearing angle. 114

6.1 Reference frame for radar activities: (a) schematics with respect to antennas and (b) geometry for bearing angle estimation. 119
6.2 Schematics for the entire process of radar-aided navigation. 120

6.3 Range processing operations at time step n for a-th channel. 123
6.4 Magnitude and Bearing Angle Estimation at time step n. Two channels are active. 124
6.5 Effects of high or low threshold on target detection. 126
6.6 CA-CFAR schematic. 127
6.7 OS-CFAR schematic. 129
6.8 Outputs of CA-CFAR (red) and OS-CFAR (blue) with an actual scene. The parameters for CA-CFAR are $\alpha_{CA} = 8.53$, and $N_{CA} = 16$. The parameters for OS-CFAR are $N_{OS} = 24$, $k_{OS} = 18$, and $\alpha_{OS} = 5$. The probability of false alarm is $P_{fa} = 10^{-3}$ for both cases. 129
6.9 Multiple-Target Tracking schematics. 130
6.10 Track handling schematics. 132
6.11 Setup: radar, laptop, gps receiver, camera, and platform. 138
6.12 Algorithm for combined radar and GPS data acquisition. 139
6.13 Test site and environment for measurements. Three CRs are visible in red, blue, and green boxes. 140
6.14 Path covered during platform motion as provided by GPS solution. Red, blue, and greed dots are CRs. Magenta and azure squares represent starting and ending points, respectively, during the 300s-long data collection campaign. 141
6.15 Magnitude (left) and bearing angle (right) maps as function of range and time. 142
6.16 Output of OS-CFAR detector: range (left) and bearing angle (right). . 143
6.17 Output of OS-CFAR detector and range to CRs provided by GPS receiver. 144
6.18 Comparison of detections provided by OS-CFAR detector (empty circles with same colour meaning as in Figure 6.16) with measurements associated to tracks (thin lines with different colours for each track). . 145
6.19 Comparison of measurements associated to tracks (top) with smoothed data provided by EKF (bottom). 146

6.20 Number of firm tracks, tentative tracks, and detections at each time step during the experimental campaign. Red lines represents the average values. 147
6.21 Details of firm tracks used for radar odometry. Range (top) and bearing angle (bottom). 148
6.22 North-East trajectory. 148
6.23 Errors in North-East plane. 149
6.24 Errors in Forward-Cross range plane. 150

List of Tables

1.1 Activities with ultralight radar sensors: summary. 6
1.2 Key issues for a novel mini-UAS based SAR system. 10

2.1 Main features of existing compact lightweight SAR systems (N/A = not available). 15
2.2 Input parameters for system design. 25
2.3 Constant parameters for system design. 27
2.4 Selected working parameters. 36

3.1 Dimensions of control volume 40
3.2 Set of basic actions required in 2D RT algorithm. 49
3.3 Point Target Response for a side-looking observation 64
3.4 Fluctuating target: Point Target on -20dB background 66
3.5 Fluctuating target: Point Target on -10dB background 67
3.6 Additional parameters for observation. 80
3.7 Position and velocity of the antenna halfway through the integration time. 81

4.1 Characteristics of integrated lens antenna (ILA) for 94 GHz center frequency. 84
4.2 Performance of XSens MTi-G-710 GNSS 88
4.3 Position of CRs during experimental campaign. 90
4.4 Acquisitions during experimental campaign. 91

4.5 Settings for the 94-GHz radar. 91
4.6 Settings for the 94-GHz radar. 96

5.1 Characteristics of Antennas 100
5.2 Radar Performance: Nominal Accuracy 100
5.3 Results of radar measurements. 103
5.4 Radar parameters during first campaign. 105
5.5 Radar parameters and GPS data during second campaign. 111

6.1 Radar Settings 138
6.2 OS-CFAR Settings 142
6.3 MTT Settings 144
6.4 Statistics of errors 149
6.5 Offline processing times 151

Chapter 1

Introduction

Unmanned Aircraft Systems (UAS) are commonly defined as a uninhabited aerial vehicles able to attain stable flight operation thanks to a control system which can be programmed to follow a certain flight path or can be remotely controlled from a ground station. More precise definitions are being proposed and UAS can be viewed as an entire system comprising, in addition to the aircraft platform carrying the payloads (often referred to as Unmanned Aerial Vehicle, UAV), the control station, the payloads, the system of communication between the aircraft and the control station, the navigation systems, and support equipments [1]. This last definition, i.e., the UAS as a whole system, enables different classification schemes. Most of them are based on types of air vehicles and their autonomy [1, 3, 2]. Several other classifications are however in use depending on applications, such as military classification and classifcation based on operational altitude and collision [3].

The considerable amount of research on and industrial attention to UAS over the years is mainly due to their capability to perform dull, dirty or dangerous (DDD) roles [1], as well as to economic reasons. Indeed, testing and research, both civilian and military, can be carried out more cheaply and less hazardously than with manned systems [1]. Some examples of the civilian applications for

UAS are agriculture, search and rescue, coastline and sea-lane monitoring, powerline inspection, monitoring and control of road traffic [1].

Additionally, in the last years a strong interest grew towards miniaturized UAS and their applications. Two main classes of UAS can be referred to as miniaturized UAS, namely Micro Aerial Vehicles (MAVs or Micro-UAS) and Small- (or Mini-) UAS [2, 3]. Although specifications for the two classes are not univocally defined, under the category of MAVs can be grouped all the UAS weighing less than 5 kg, whereas all UAS, whose weight is up to 30 kg, can be labeled as small- or mini-UAS [3]. One of the reasons for the wide spread of these systems can be found in the miniaturization of flight control systems and payloads. Typical sensors housed onboard mini- and micro-UAS range from cameras, either electro-optical/infrared (EO/IR) [4]-[7] or RBG-D [8], to inertial sensors [5],[7] and Global Positioning System (GPS) receivers [5]. Sense-and-avoid (SAA) and autonomous navigation represent largely investigated applications with these sensors [9]. On the contrary, fewer investigations are available in literature about the use of radars as payloads of mini- and micro-UAS at present time, although they can be possibly exploitated in several fields of application.

1.1 Applications of radar technology to mini- and micro-UAS

Examples of radar payloads for larger-scale UAS exist, such as autonomous UAV navigation and simultaneous localization and mapping (SLAM) in harsh or complex environments by means of radar odometry, investigated by Brigham Young University [10]. Other examples are the radar-based solution proposed by Massachussets Institute of Technology to comply with Federal Aviation Administration (FAA) requirements [11], i.e. an electronically scanned radar, and

a multichannel Frequency Modulated Continuous Wave (FMCW) radar exploiting digital beamforming [12] developed by TNO in cooperation with Rockwell Collins for SAA. However, the constraints on size, weight, and power (SWaP) have often represented a limit to usage of radars onboard mini- and micro-UAS, despite their ability to operate under any illumination condition and provide instant access to range information. Nevertheless, some radar sensors compliant with mini- and micro-UAS restraints have been developed recently, such as a very lightweight radar to be placed on rotorcraft UAV for SAA and air traffic control purposes developed by University of Denver [13], a lightweight K-band radar manifactured by IMST GmbH [14], and a lightweight C-band radar manifactured by Time Domain Inc. [15].

Potential applications of ultralight radars can be summarized as follows:

Radar-Aided Navigation Autonomous navigation systems currently rely on measurements from both Inertial Measurement Unit (IMU) and GPS sensor to be given as input to a Kalman Filter, thus correcting the drift of IMU itself [10]. However, when GPS signal is not available, different solutions have to be found in order to compensate the limited performance of small and cheap IMUs with which MAVs can be equipped. Typical algorithms for GPS-denied navigation are based on visual odometry [16] and exploit change in perspective of consecutive images to estimate relative motion. Effectiveness of these algorithms is strongly related to performance of electro-optical sensors, which can degrade owing to adverse illumination condition. Radar, on the contrary, is independent of illumination condition and its resolution is independent of range distance. In addition, the presence of large amount of strong radar reflectors in the scene represents complication for target tracking. Moreover, depending on the selected radar wavelength and relative attitude between radar antennas and targets, some targets can be seen whereas other ones result not

visible [17].

Sense and Avoid Sense-and-avoid tasks are gaining increasing relevance in the framework of micro-UAS and, more in general, UAS activities. Indeed, the objective is to operate these systems alongside manned aircraft in civil integrated airspace [12]. Future operation scenarios for small and micro-UAS, such as UAS Traffic Management (UTM) [18], will also require low altitude drone-to-drone sense and avoid capabilities. Radar-based solutions for SAA are necessary to provide range and velocity information on non-cooperative targets. In addition, angle information can be obtained by either monopulse [19] or interferometric techniques [20], even though it is not as accurate as high-performance visual solutions. Other solutions for angle determination account for scanning radar beam or digital beamforming [12]. Again, proper detection of targets can become difficult when dealing with scenes having a large amount of targets, owing to initiation and maintenance of tracks. Fusion of data from multiple sensors, both radar and vision-based, could be an effective way to enhance SAA capabilities.

Imaging Radar imaging, especially Synthetic Aperture Radar (SAR) technique, represents a valuable task to be performed with the help of MAVs under any illumination conditions. Radar signal has the ability to pass through common obscurants and therefore even images of complex and dangerous environments could be collected [21]. SAR images have enhanced resolution in azimuth with respect to real aperture radars [22] and three-dimensional maps of environments could be achieved by means of either SAR interferometry [23], tomography [24], or radargrammetry [25]. Indeed, MAV capability to attain stable autonomous flight on a repetitive course at different height enables these techniques. Disadvantages of

radar imaging could be represented by less intuitive interpretation of images, which however provide direct information on range, and side-looking mounting geometries required to avoid ambiguities [22]. In addition, motion compensation due to non-ideal MAV trajectory [26] could be challenging, owing to performance of other on-board sensors.

Table 1.1 summarizes main advantages, disadvantages, and challenges related to radar technology for each application. Furthermore, it is worth noting that enhanced manufacturing techniques for miniaturizing sensors allow MAVs to be equipped with both electro-optical and radar sensors, thus improving performance and exploiting the paired set of advantages.

Finally, it is important to highlight that impressive developments with miniaturized radar sensors have been reached also in the automotive field [27]. Advanced Driver Assistance Systems (ADAS), indeed, exploit both Short- or Mid-Range Radars (SRR or MRR) and Long Range Radars (LRR). SRR and MRR operate around a car when in motion to detect possible impacts with obstacles and trigger automatically safety measures. They are permitted in 24 GHz and 79 GHz frequencies [28]. Examples are the bi-static multimodal radar with four independent receive channels and digital beam forming MRR by Bosch [29] and SRR by Continental [30]. LRR are used instead in 77 GHz band to assist Adaptive Cruise Control (ACC) and novel functionalities. Examples are LRR4, able to perform data fusion with its own control unit, by Bosch [31], the multi-channel single-chip LRR by STMicroelectronics [32], and LRR by Continental [33]. All these sensors are very light and small and have operative distances that can be extremely interesting for UAS purposes. As an example, Bosch' MRR has been also exploited in UAS-oriented application requiring sensor fusion [34], thus showing the possible interaction between automotive and UAS environments.

Table 1.1: Activities with ultralight radar sensors: summary.

	Advantages	Disadvantages	Challenges
Radar Aided Navigation	• all time/all weather • resolution independent of range • direct range and velocity measurements	• difficult interpretation with many scatterers in the scene • wavelength and relative attitude may affect measurements	• data association
Sense and Avoid	• all time/all weather • direct range, angle, and velocity measurements	• difficult interpretation/detection with many scatterers in the scene • possible hard trade-off among requirements in detection range/angular coverage/resolution/scan rate (small RCS of targets, possible need of multiple antennas/scanning systems)	• data fusion to assist visual-based sensors
Imaging	• all time/all weather • not affected by obscurants	• image distortions • not intuitive interpretation of images	• motion compensation to perform SAR processing (low performance navigation sensors)

1.1.1 Practical application

Outdoor flying unmanned vehicles have received remarkable attention and extensive research. On the contrary, there is still much to be done in the area of indoor or urban autonomous operation both for vehicle navigation and for monitoring or exploration. The application to unknown building interiors and very cluttered urban or natural environments is one of the most demanding envisioned for UAS, since it requires the real time capability: (i) to detect and identify very different objects, such as buildings, walls, caves, infrastructures or underground facilities, in problematic and unpredictable illumination conditions; (ii) to navigate through complex shaped passageways, avoiding even non-stationary obstacles; and (iii) to gather and relay information. Use of very compact-size and extreme lightweight mini-UAS or MAVs, differently than in outdoor applications, represents an additional requirement when indoor flight operations must be performed. Target mission scenarios include high risk indoor inspection, e.g., nuclear power plant failure and leakage or tunnel roof fall in mine, but also search for survivors in cluttered dense urban environment or indoor, such as underground railways or industrial warehouse. Pipeline inspection and Nuclear Biological or Chemical (NBC) emergency reconnaissance represent additional dangerous applications that could take full advantage from small UAS and MAV operations. Completely different scenarios but similar capabilities are required in planetary exploration. Specifically, in past decades rovers have emerged as one of the most important tools for planetary exploration. Important drawbacks of rover systems deal with the limited coverage they can achieve and uncertainty in terrain. For planetary and planet-like bodies, when a significant atmosphere is present, above limitations can be overcame by aerial vehicles. In addition to Earth, several planets, such as Venus, Mars, Jupiter, Saturn, Uranus, and Neptune, but also the Saturn moon Titan, are endowed with an adequate atmosphere. Aerial vehicles proposed and investigated

for planetary exploration include [35, 36, 37] airplanes and gliders, helicopters, balloons, and airships. The most investigated solutions are based on lighter-than-atmosphere robotic airships combining the long-term airborne capability of balloons with the maneuverability of airplanes or helicopters.

The introduced applications involve flight operation in GPS-denied and substantially unknown environments with potentially large communication latency (planetary explorations) or extended communication blackout periods (indoor emergencies). Accomplishment of two basic functions is required to carry out these tasks: fully autonomous navigation with obstacle detection/avoid capability and high resolution 3D mapping and monitoring of the target area, including moving target detection. Unless the small UAS is provided with hovering capability, autonomous navigation presents clearly the most stringent time requirements. Regarding obstacle avoidance, in theory accurate geometric models of the operational environment combined with thematic information and description of all the present objects could reduce the need for continuous and real-time sensing. However, those data are often neither updated nor available at the required spatial resolution and accuracy. Furthermore, unexpected obstacles, for instance consequent to an accident that is required to investigate, can appear anytime and anywhere, hence real-time mapping capabilities are required too.

The set of data needed to perform these tasks cannot be provided by sensors potentially adequate under conventional operating conditions, such as laser scanner and optical cameras, owing to their physical size, weight, strong dependence on illumination conditions and possible poor visibility caused by environmental factors. Conversely, radar sensors are able to operate in any illumination condition and microwave carrier frequencies allow for coherent signal detection to be performed, thus resulting in significantly increased sensitivity and instant access to range information. In addition, high resolution 3D mapping can be provided by combining SAR technique with radar interferometry [22, 23]. This also makes

velocity information available via Doppler processing, which is a valuable feature for sensors operating on board moving platforms. Finally, millimeter wave (MMW) radar technology has been receiving an increasing interest for application in small UAS [26, 38] thanks to the limited size and power requirement and the capability to penetrate smoke and fire [39, 40].

This novel application, whose key issues are summarized in Table 1.2, encompasses all the activities that can be achieved by ultralight radar sensors and miniaturized UAS. In addition, it can open the way to research on indoor autonomous operations by miniaturized UAS and requires a novel ultralight radar sensor.

1.2 Scope and aims

In the presented scenario, the scope of this research is to develop design strategies and processing approaches for a novel ultralight radar sensor able to provide the miniaturized platform with SLAM capabilities, mainly but not exclusively indoors. In addition, the sensor has to guarantee very high 3D resolution and accuracy, and capability to perform real-time onboard processing in order to support autonomous navigation, exploration and mapping in completely unknown and unstructured environments. Millimeter-wave Interferometric Synthetic Aperture Radar (mmw InSAR) technology has been identified as a key asset. At the same time, testing of commercial lightweight radar developed for MAVs is carried out to assess current capabilities to be compliant with requirements for complex mission scenarios involving integration of autonomous navigation, sense-and-avoid, and imaging.

The two main research lines can be outlined as follows:

Long-term scenario research Development of very compact and ultralight Synthetic Aperture Radar able to provide mini- or micro-UAS with very

Table 1.2: Key issues for a novel mini-UAS based SAR system.

Main Constraints	
Mass	< 1 kg
Size	< 1500 cm^3
Maximum dimension	< 30 cm
Antenna maximum length	< 10 cm
Power consumption	< 10 W
Real-Time on-board processing	
Expected Performances	
3D Mapping without ground truth	
3D geometric resolution	10–20 cm
Field-of-view	Hemispherical
Operation in presence of smoke and fire	
Possible Technical Solutions	
SAR	
Radar Interferometry	
Millimeter Wave Radar	

accurate 3D awareness in indoor or GPS-denied complex and harsh environments.

Short-term scenario research Assessment of true potentialities of current commercial radar sensors in a UAS-oriented scenario.

Within the framework of long-term scenario research, after a review of state-of-art SAR sensors, Frequency-Modulated Continuous Wave (FMCW) SAR technology has been selected as preferred candidate. Design procedure tailored to this technology and software simulator for operations have been developed in MATLAB environment. Software simulator accounts for the analysis of ambiguous areas in a three-dimensional environment, different SAR focusing algorithms, and a Ray-Tracing (RT) algorithm specifically designed for indoor operations. The simulations provided relevant information on actual feasibility of the sensor, as well as mission design characteristics. Additionally, field tests have been carried out at Fraunhofer Institute FHR with a mmw SAR. Processing approaches developed from simulations proved to be effective when dealing with field tests.

A very lightweight FMCW radar sensor manifactured by IMST GmbH has been tested for short-term scenario research. The codes for data acquisition were developed in Python language both for Windows-based and GNU/Linux-based operative systems. The radar provided information on range and angle of targets in the scene, thus being interesting for radar-based UAS navigation. Multiple-target tracking (MTT) and radar odometry algorithms have been developed and tested on actual field data. Radar-only odometry provided to be effective under certain circumstances, but an integration with IMU housed onboard the UAS platform could guarantee improved performance.

The thesis is organized as follows. Chapter 2 and Chapter 3 describe the design process and the results of simulations for a novel mm-wave InSAR, respectively. Chapter 4 illustrates the outcomes of experimental campaigns with a

mm-wave SAR for small UAS developed at Fraunhofer Institute FHR. Chapter 5 presents the testing of a commercial lightweight radar sensor and its potential concerning mini-UAS activities. Finally, Chapter 6 discusses key issues and results of radar odometry with a mini-UAS.

Chapter 2

mm-wave InSAR design

Indoor autonomous missions, for instance indoor inspection in emergency missions, damage assessment or search for survivors in dangerous environments, or, more in general, operations in GPS-denied, complex, and unknown environments can be accomplished by means of miniaturized UAS and ultralight radar sensors. However, at current time, no such radar sensors able to satisfy the mission requirements listed in Table 1.2 are available. Hence, design process is the first step towards its realization. In this Chapter, a review of state-of-art lightweight SAR is illustrated to assist decisions about the system architecture. Key technologies and main issues and outcomes of design process are then presented and discussed.

2.1 System Architecture

2.1.1 State-of-the-Art Analysis

The novel ultralight radar sensor has to work in the millimeter-wave spectrum and exploit SAR interferometry (see Table 1.2). A state-of-the-art analysis is mandatory to understand trends and key characteristics of recently developed

and existing lightweight SARs.

In the last decade several compact and lightweight SARs have been developed and tested for different purposes and applications. Table 2.1 lists the most relevant systems together with their main features, as available in the open literature. All of them are devoted to outdoor operations, such as surveillance and remote sensing applications, and work in side-looking mode with limited pointing capability.

None of these systems satisfies all the constraints of Table 1.2. Real-time onboard operation is rarely enabled, resolutions can be not sufficient, and, in most cases, mass and power requirements exceed small platform availability. Nonetheless a few interesting features can be highlighted. MiniSAR by Sandia National Labs [41] and MISAR by EADS [38] both include a double gimbal structure which allows mechanical steering of the antenna to be achieved, thus making possible SAR interferometry along multiple directions. In both cases two separated antennas, one for transmission and one for reception are accommodated to implement a FMCW scheme. More than half of the listed sensors exploit this architectural scheme, even though without a gimbal structure.

In addition, it is worth noting that all the sensors working in millimeter-wave spectrum [38, 42, 50, 58] use a FMCW scheme.

Finally, it is important to remark that ARBRES X-Band SAR [59] and MetaSensing X-Band SAR [60] make use of three antennas, namely two receiving and one transmitting for performing FMCW single pass interferometry.

Table 2.1: Main features of existing compact lightweight SAR systems (N/A = not available).

	Mass (kg)	**Size** (cm^3)	**Power Consump.** (W)	**Transm. Power** (W)	**Resolution** (m)	**Max Range** (km)	**Bandwidth** (MHz)	**Carrier Frequency** (GHz)	**Scheme**	**Real Time Processing**	**Single Pass Interferometry**
LUAVR [42]	9	32,774	100	1	0.1	10	1800	35	FMCW SAR	Yes	No
MISAR [38, 43]	4	10,000	100	1	0.5	4	300	35	FMCW SAR	No	No
BYU MicroSAR [44, 45]	2.7	2295.38	16	1	1	0.7	90	5.55	FMCW SAR	No	No
MiniSAR [41]	14	250	250	60	0.3	10	3000	16.8	Pulsed SAR	Near-real time	No
NuSAR [46, 47]	8.62	N/A	160	25	0.3	0.7	500	9.75	Pulsed SAR	Yes	No
PicoSAR [48, 49]	10	10,797	300	1	0.3	20	768	9.7	Pulsed SAR	Yes	No
MINISARA [50, 51]	2.5	7296	N/A	1	0.07	2.97	2000	34	FMCW SAR	N/A	No
BYU MicroASAR [52]	3.3	1880.71	35	1	0.75	N/A	200	5.43	FMCW SAR	No	No
SlimSAR [53, 54]	4.54	N/A	150	4	0.23	N/A	660	9.28	FMCW SAR	No	No
NanoSAR [55]	0.91	1674	15	1	0.3	1	500	10.25	Pulsed SAR	No	No
NanoSAR B [56]	1.59	1458.49	30	1	0.3	4	N/A	N/A	Pulsed SAR	No	Yes
NanoSAR C [57]	1.18	1409.29	25	1	0.3	3	N/A	N/A	Pulsed SAR	No	Yes
MIRANDA [58]	2.2	4459.13	20	0.1	0.15	2	1000	94	FMCW SAR	No	No
ARBRES SAR [59]	2.5	5950	50	N/A	1.5	N/A	100	9.65	FMCW SAR	N/A	Yes
MetaSensing SAR [60]	N/A	N/A	N/A	N/A	0.4	N/A	450	9.65	FMCW SAR	N/A	Yes

2.1.2 Why MMW

Operations in millimeter-wave spectrum have been selected as a requirement for novel radar. This is because the very nature of envisaged application requires the miniaturization of radar system and the capability of high-resolution measurements, even in adverse or dangerous environmental conditions. Millimeter-wave radar technology represents an optimal solution towards the fulfillment of those requirements [21]. Indeed, shorter wavelengths allow MMW radar sensors both to be smaller and lighter than their counterparts in microwave region and to possess an enhanced Doppler resolution. In addition, a wide bandwidth can be transmitted more easily, thus enabling high resolution even in range direction [61]. A further advantage is represented by the reduced beamwidth dimensions that allow less defocusing and smearing when handling returns from moving targets [62].

Few studies are available in literature concerning the capability of millimeter wavelengths to operate through smoke, dust and flames and each of them deals with a particular case or carrier frequency. In [63] it has been shown that for a 94 GHz system the negative effects due to dust decrease if the visibility increases and an attenuation of 10 $\mathrm{dB\,km^{-1}}$ has been found with a 0.5-m visibility. Experimental test demonstrated an absorption of 0.02 $\mathrm{dB\,m^{-1}}$ through a high-density (3-m visibility) dust-cloud for radar system operating at 94 GHz in [64]. Fire could be the most problematic element to deal with. When weakly ionized fires are addressed, the absorption of the signal is strongly influenced by both the temperature of the fire and the frequency of the signal. However, the most relevant problem is the phase variation of the signal when passing through flames [40]. On the contrary, the most relevant effect of hydrocarbon flames is the scintillation, that causes 1.5 dB losses for a 97 GHz signal, whereas attenuation through a 0.5-m fire is lower than 1 dB [39].

Finally, it is worth highlighting that even in the few windows available in

MMW region of the electromagnetic spectrum the signal is heavily absorbed if long distances are addressed. On the contrary, limited loss is present for small distances [65]. Therefore, for the selected close-range applications no major drawbacks can be individuated if a millimeter wave carrier frequency is chosen.

2.1.3 Why FMCW SAR

According to this state-of-art analysis, FMCW SAR is a preferred choice for lightweight radar sensors and for operations with millimeter waves. FMCW radar transmits a frequency modulated signal, which is usual in SAR, but in continuous wave differently from most realizations. Received echo, which is delayed by round trip delay τ associated with target-range distance, is mixed with transmitted signal [66]. For a linear frequency modulation the output of mixing process, namely the beat signal, has two Fourier components at different frequencies. The first component is a signal centered at constant frequency lower than the carrier frequency [67]. The second component is a residual signal centered approximately at twice the carrier frequency which has less energy with respect to former component [66] and is filtered out. The process involving both the mixing of transmitted and received signals and the low-pass filtering of beat signal is also called *deramp-on-receive* and the output is

$$s_B(t) = A\,\mathrm{rect}\left(\frac{t-\tau}{T}\right)\exp\left\{2\pi j\left(f_C\tau + \frac{B\tau}{T}t - \frac{B\tau^2}{2T}\right)\right\} \tag{2.1}$$

where t is the time referring to signal transmission/reception at light velocity c, B is the transmitted bandwidth, f_C represents the carrier frequency, and T is the sweep period. The last phase contribution in beat signal (2.1) is an unwanted phase term called Residual Video Phase (RVP).

The aforementioned low, constant frequency in beat signal, which is computed by differentiating the phase term of beat signal with respect to time, is labeled as beat frequency. Beat frequency holds strong relevance in FMCW

radar as it is directly proportional to target range by the ratio between propagation velocity and bandwidth of transmitted signal thus allowing the system to compute range by measuring beat frequency [21]. The theoretical value for range resolution is [66]

$$dr = \frac{c}{2B} \tag{2.2}$$

Actually, Equation (2.2) is equivalent to conventional pulsed radar theoretical range resolution [22, 68]. However, it is important to remark that FMCW range compressed signal is obtained in frequency domain rather than in time domain.

FMCW scheme guarantees decisive advantages with respect to conventional pulsed SAR especially when compact systems have to be realized. Continuous transmission, *i.e.* unity duty cycle $\eta = 1$, involves less transmitted peak power, which makes possible significant simplifications in the power generation and conditioning unit along with a strong reduction in power requirements with respect to pulsed systems. In addition, *deramp-on-receive* relies on the sampling of beat signal bandwidth B_B instead of the whole transmitted bandwidth B. This means that even GHz bandwidth can be easily handled by MHz sampling frequency f_S, because $B_B \ll B$, thus allowing simpler and cheaper hardware equipment.

FMCW particular features in comparison to traditional pulsed technology are consequent to the motion during continuous transmission. A better understanding of motion effects on signal is given by [69] in which it is reported the following equation for the beat signal in the two-dimensional spatial frequency domain

$$S_B\left(K_r, K_x\right) = \exp\left(jK_x vt\right) \exp\left(jR_0\sqrt{K_r^2 - K_x^2}\right) \tag{2.3}$$

where K_r and K_x are the spatial frequencies in range and azimuth directions, respectively, v is the platform velocity, R_0 is the distance of closest approach. The second exponential in Equation (2.3) coincides with beat signal of conventional pulsed SAR in two-dimensional spatial frequency domain, whereas the

first is a space invariant term that takes into account the motion during transmission. This term becomes equal to one in conventional SAR because of the start-stop approximation, which assumes that the radar is stationary during the pulse transmission-reception because $v \ll c$. Start-stop approximation is traditionally exploited to explain raw SAR images formation [22]. As a direct consequence of Equation (2.3), in general, conventional algorithms for SAR image formation would result in FMCW SAR image degradation. More complex reference functions have to be adopted in these cases [70].

However, specific conditions exist in which start-stop approximation can be considered valid for FMCW SAR too. Even though continuous transmission is used, it is possible to define the concept of Pulse Repetition Interval (PRI) for FMCW radar as the sweep duration, *i.e.*, the time the transmitted frequency takes to shift from the minimum to the maximum frequency, or equivalently the time between the start of two consecutive sweeps. It is clear that the last definition leads to almost similar PRI meaning as for pulsed SAR, although it refers to sweep instead of chirp (see Figure 2.1). Based on the introduced PRI, Pulse Repetition Frequency can be defined as the reciprocal of the PRI.

The Nyquist sampling theorem requires PRI to be small enough in order to sample properly azimuth Doppler history. In detail, provided that sampling requirements are satisfied [70], each sweep represents a sample of the Doppler history in the same way as a pulse of conventional SAR. Hence, both fast time t and slow time t_N (*i.e.*, referring to radar motion at velocity v) can be introduced for FMCW SAR too. On the other hand, a longer sweep duration would produce several samples in the azimuth Doppler history within each sweep, thus making start-stop approximation less acceptable.

As in conventional SAR, FMCW SAR target response exhibits a Doppler bandwidth, B_D, generated by the variation of observation angle and therefore

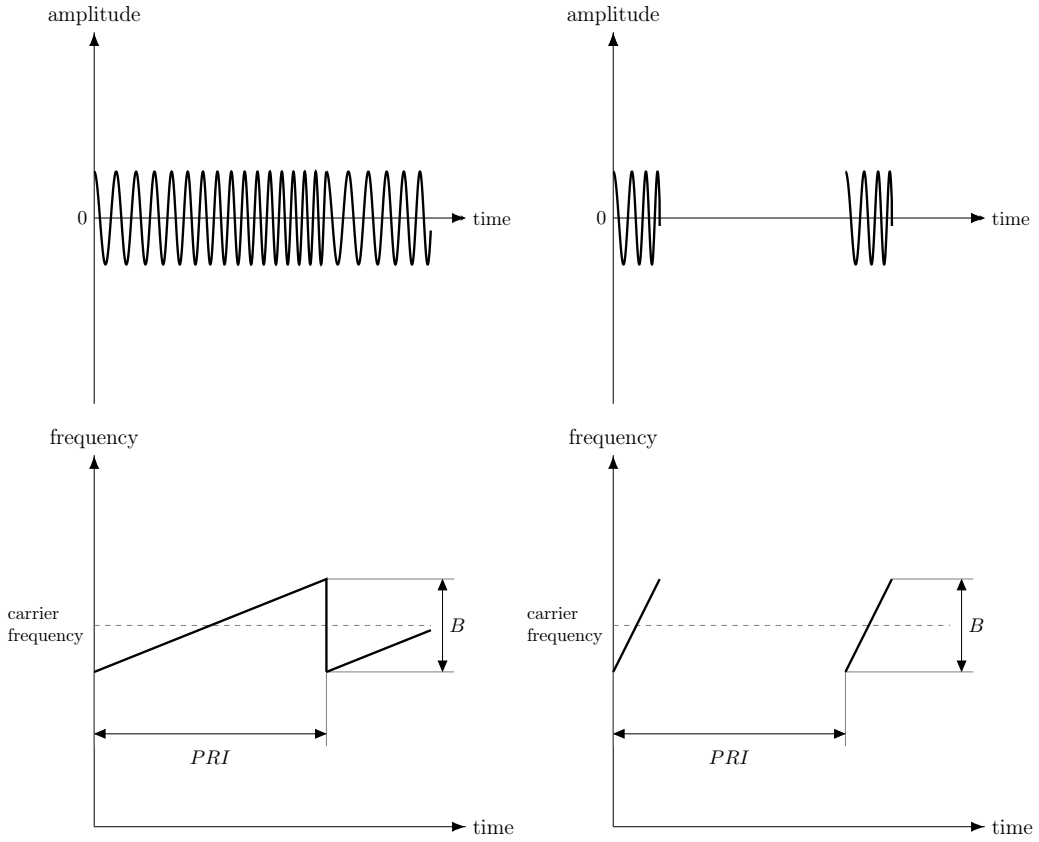

(a) FMCW SAR **(b)** Conventional pulsed SAR

Figure 2.1: Comparison between *PRI* (a) in FMCW SAR and (b) in conventional pulsed SAR. Plots not to scale for clarity.

by the variation of radial velocity

$$B_D = 2\frac{v}{\lambda}\left[\sin\left(\theta_{sq} + \frac{\theta_{\text{az}}}{2}\right) - \sin\left(\theta_{sq} - \frac{\theta_{\text{az}}}{2}\right)\right] \tag{2.4}$$

where λ is carrier wavelength, θ_{sq} is the squint angle and θ_{az} is the beamwidth in azimuth direction. Hence, provided that proper motion compensation algorithms are exploited [66, 70], theoretical FMCW SAR azimuth resolution is

$$da = \frac{v}{B_D} = \frac{l_{\text{az}}}{2} \tag{2.5}$$

where l_{az} is the antenna length. Equation (2.5) is exactly the same equation that holds for conventional pulsed SAR.

As expected, the result of range and azimuth compression is a bi-dimensional *sinc* function multiplied by two complex exponentials, the former depending on both minimum platform to target distance and a reference distance R_{ref} used for the processing [71], the latter depending only on the reference distance and system parameters. Namely

$$\begin{aligned} s\left(f_R, t_N\right) = \operatorname{sinc}&\left[\pi\left(f_R + \frac{R_0 - R_{\text{ref}}}{cPRI}2B\right)\left(PRI - 2\frac{R_0}{c} - \frac{v^2 t_N^2}{cR_0}\right)\right]\cdot \\ \operatorname{sinc}&\left[B_D\left(t_N - \frac{x_0}{v}\right)\right] B_D \exp\left[-j\frac{4\pi}{\lambda}\left(R_0 - R_{\text{ref}}\right)\right] \exp\left(-j\pi\frac{B}{PRI}\tau_{\text{ref}}^2\right) \end{aligned} \tag{2.6}$$

where f_R is the range frequency, x_0 is the position of target along the azimuth direction with respect to center scene, and τ_{ref} is the time delay of echo at reference range R_{ref}, which corresponds to range from center scene. The first exponential resembles the exponential term of pulsed SAR 2D-focused signal and again can be exploited to perform interferometry [22]. Moreover, it has to be noted that signal (2.6), unlike pulsed SAR 2D-focused signal, is better described in range-time domain, as range frequency f_R is directly proportional to range in FMCW SAR. The mapping between range frequency and range can be expressed for linear frequency modulation as

$$R = f_R\frac{cPRI}{2B} \tag{2.7}$$

Finally, the amplitude of the resulting signal depends on Doppler bandwidth.

The implementation advantages of FMCW SAR must be weighed against some drawbacks that this scheme exhibits. In general, data processing is more complex with respect to pulsed SAR because deramp-on-receive produces the unwanted RVP that must be removed. In addition, moving targets can introduce ambiguities in range measurement. Indeed, owing to longer observation time compared to a conventional system, targets can move through several resolution cells within a sweep [70], causing the Doppler effect not to be negligible. Several solutions have been proposed to correctly determine range even in presence of moving targets, including triangular frequency modulation [66, 67] to determine range and Doppler information within a single time interval. Non-linearities in transmitted and received signals cause additional erroneous phase term in beat signal, therefore leading to deteriorated range resolution [70]. Typical algorithms for non-linearities correction work under the assumption that non-linearity effects depend linearly on time delay, which is true for small distances (which is the case of indoor applications), whereas falls for long range observations and causes the computational load to increase. Hardware and software solutions are known in literature [66, 70], such as Voltage Controlled Oscillator (VCO) and Direct Digital Synthesizer (DDS), or approaches based on approximations of non-linearity. Finally, the simultaneous signal transmission and reception generate signal leakage in the reception chain. Specifically, due to the extremely high transmitted-to-received power ratio, saturation or damages of equipment can occur if even a small leakage of transmitted power is present [67]. Good isolation is therefore required and typically separated transmitting and receiving antennas in both bistatic and quasi-monostatic configurations are exploited. Considering that relatively assessed solutions are today available to deal with the discussed drawbacks, and taking into account its advantages for the considered applications, FMCW SAR scheme is selected herein as a base for system

architecture.

2.1.4 Why SAR Interferometry

SAR Interferometry is a technique that exploits phase information, obtained from two or more SAR images, in order to compute target height and position in a three dimensional environment. It can be considered a well-assessed technology for conventional pulsed SAR [22, 23]. As regards FMCW SAR, 2D-focused SAR signal (2.6) shows that the phase of the azimuth *sinc* samples target range as multiple of wavelength and can therefore utilized to perform interferometry. It has to be noted that it is necessary to remove the additional contribution to phase given by the reference range distance, which is typically the distance to the center of scene illuminated by beamwidth and therefore can be different in the two images to be correlated. SAR interferometry has been successfully tested on data collected by FMCW SAR [60] and it is considered a key asset towards the operational scenario considered in this work.

2.1.5 Selected Scheme

Based on the state-of-the-art analysis, a system architecture that is potentially able to satisfy all requirements listed in Table 1.2 is shown in Figure 2.2. The selected scheme is an interferometric FMCW SAR with three antennas, one transmitting and two receiving, mounted on a double gimbal structure. Among various factors, interferometric measurement resolution and accuracy are strongly dependent on antenna separation knowledge and control. Furthermore, the proposed system is compact and operates on a single platform, *i.e.*, the two antennas could be rigidly connected and simultaneously pointed to specific targets by adequately rotating a double gimbal to change the baseline (*i.e.* antenna separation with respect to target). Hence, it is expected to achieve adequate performance.

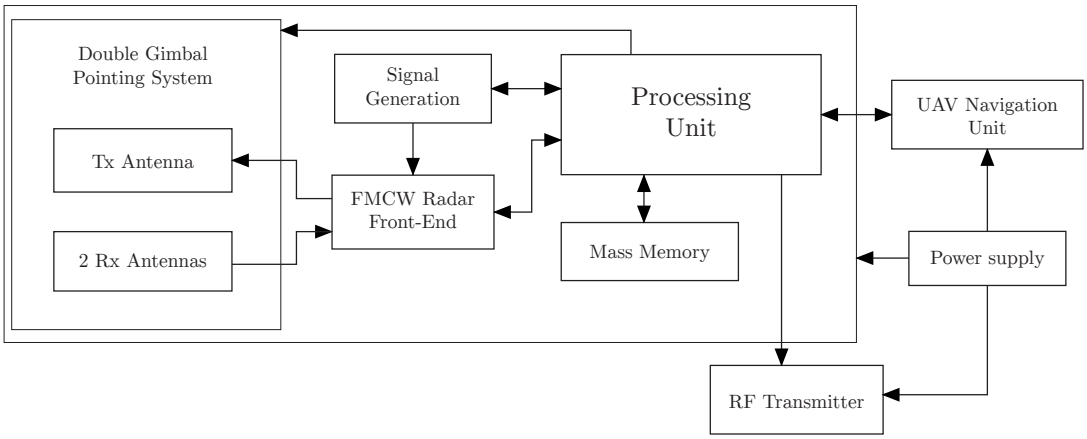

Figure 2.2: System architecture.

It is worth noting that: (i) although electronic antenna steering would be favorable for fast and accurate sweeping of all hemispherical Field-of-View, creation of adequate baseline components to extract phase measurements is based on antenna mechanical re-orientation. Consequently, design and development of a double gimbal has been considered to make easier realization of both antenna and electronics; (ii) depending on the platform selected for the mission, antenna mechanical re-orientation can be achieved by either rotation of platform itself or combined action of platform and double gimbal.

In addition, an autonomous processing unit (PU), committed to real-time on-board data processing, is included in the scheme. Radar data are stored on-board in a mass memory unit. These data are exploited by PU to directly command double gimbal pointing system. PU also sends information to UAS navigation unit via direct interface data link. Communication from the navigation unit to PU is also necessary to support image processing and data extraction. Finally, PU interfaces with Radio Frequency transmitter to send stored data to ground station via wireless data link, when available.

Table 2.2: Input parameters for system design.

Symbol	Parameter	Unit	Min. Value	Ma. Value
dr	Range resolution	(cm)	10	20
da	Azimuth resolution	(cm)	10	20
dh	Height resolution	(cm)	10	20
v	Platform velocity	($\mathrm{m\,s^{-1}}$)	0.25	2.00
θ	Off-nadir angle	(°)	15	75
θ_{sq}	Squint angle	(°)	−45	45
$R_{\max}$	Maximum distance	(m)	25.0	30.0
$R_{\min}$	Minimum distance	(m)	0.5	3.0
Δh	Height difference between two points in adjacent range cells	(cm)	5	20
N_{BIT}	Number of bits		16	32

2.2 Preliminary System Design

The design process is outlined in Figure 2.3: circles represent input parameters, which have been chosen according to system requirements (Table 1.2), system architecture (Figure 2.2) and application, whereas boxes return sought values. The input parameters of design process are chosen first. Table 2.2 lists input parameters that vary within a minimum and maximum value, whereas Table 2.3 lists the ones that assume a constant value in the implemented design process.

Resolution requirements in range, azimuth and height directions are chosen according to expected performance, whereas boundaries on platform velocity and maximum and minimum range distances depend on the application. In our case it is dynamics of the small UAS flying in indoor environment performing loitering maneuvers. In addition, a typical value for an indoor differential radar cross section has been considered. The following sub-sections report a brief explanation of particular blocks, specific for FMCW SAR design. An example of overall system characteristics are finally derived, accordingly.

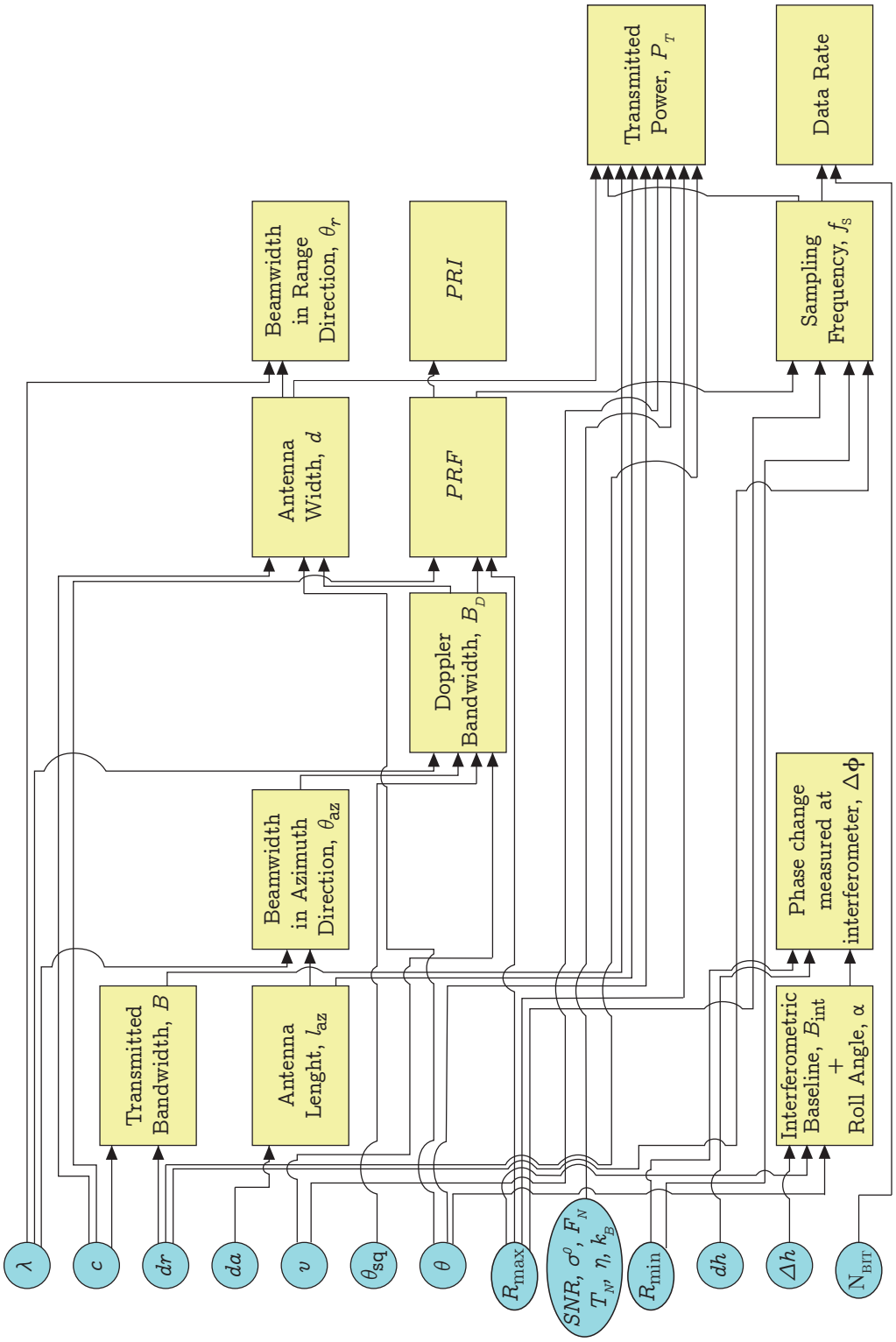

Figure 2.3: Design process guidelines: block diagram.

Table 2.3: Constant parameters for system design.

Symbol	Parameter	Unit	Value
f_C	Carrier frequency	(GHz)	94
λ	Wavelength	(mm)	3.2
c	Speed of light	$(\mathrm{m\,s^{-1}})$	$3{\times}10^{8}$
k_B	Boltzmann's constant	$(\mathrm{J\,K^{-1}})$	$1.38{\times}10^{-23}$
T_N	Temperature of system	(K)	290
F_N	Figure of noise	(dB)	15
SNR	Signal-to-Noise ratio	(dB)	20
σ^0	Differential scattering coefficient	(dB)	-20
η	FMCW SAR duty cycle		1

2.2.1 Ambiguities and Antenna Width

Range ambiguity for a FMCW radar may occur owing to the continuous transmission of a frequency modulated signal when an echo from a target arrives at receiver after the end of the sweep which generated it. As a result received signal will be mixed with a different sweep and the target will result closer than in reality (see Figure 2.4). The unambiguous range is therefore equal to the round-trip distance covered by the wave in a single sweep, namely

$$R_u = \frac{cPRI}{2} \tag{2.8}$$

However, owing to sampling theory and recalling the mapping (2.7), the maximum observable range depends also on the sampling frequency f_S as

$$R_{u,s} = f_S \frac{cPRI}{4B} = \frac{f_S}{2B} R_u \tag{2.9}$$

Therefore, under the hypothesis that the whole swath width is less than the unambiguous range, the following inequalities shall be satisfied to avoid echo

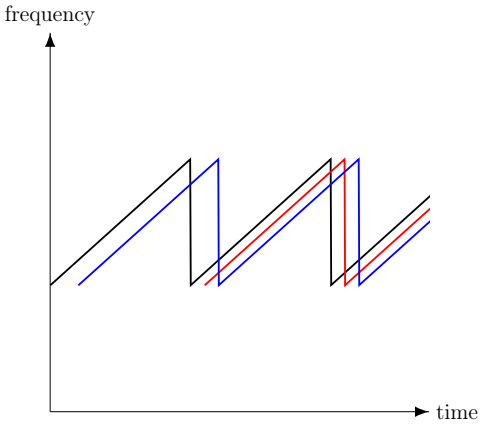

Figure 2.4: FMCW ambiguity in range: first sweep reflection from furthest target (red line) is between transmitted signal (black line) and second sweep reflection from closest target (blue line) so that furthest target is imaged closer.

ambiguities and bandwidth undersampling

$$\frac{2B}{f_S}\frac{c}{2\left(R_{\mathrm{FR}}-R_{\mathrm{NR}}\right)} > PRF > 2B_D \tag{2.10}$$

where the subscripts FR and NR refer to far and near range, respectively. The difference $R_{\mathrm{FR}} - R_{\mathrm{NR}}$ depends on antenna aperture, hence on antenna width in elevation in inverse proportion. Since considered distances and Doppler bandwidth are small and for FMCW radars $f_S \ll B$, Equation (2.10) does not yield strict bounds on antenna dimensions. Hence, antenna width d can be quite small and may be chosen according to other requirements, e.g., radar equation, heat dissipation and technological restrictions.

2.2.2 Transmitted Power

Transmitted power can be computed by the following formula derived in [72]

$$P_T = \frac{SNR\left(4\pi\right)^3 R_{\mathrm{max}}^4 k_B F_N T_N B_N}{G_T G_R \lambda^2 \sigma^0 dr_{\mathrm{gr}} da N_R N_A} \tag{2.11}$$

which takes into account range and azimuth compression gains, N_R and N_A respectively. In Equation (2.11) the subscripts T and R refer to transmitting and receiving antenna gains (G), B_N is the noise bandwidth and dr_{gr} is ground range resolution.

For rectangular antennas the gain at boresight is expressed in [73, 74] as

$$G = k_e \frac{4\pi A}{\lambda^2} \tag{2.12}$$

where k_e is an efficiency factor, typically equal to 0.65, and A the antenna area. Under the hypothesis of identical transmitting and receiving antennas and by expressing compression gains as in [75], Equation (2.11) becomes

$$P_T = \frac{SNR\ 4\pi R_{\mathrm{max}}^3 k_B F_N T_N B_N l_{\mathrm{az}} v}{\eta\ {k_e}^2 A^2 \sigma^0 dr_{\mathrm{gr}} da B} \tag{2.13}$$

Concerning the transmitted power, it is important to point out that in FMCW SAR noise bandwidth B_N is equal to sampling frequency f_S [76]. This is an additional advantage over conventional SAR, which noise bandwidth is equal to transmitted one.

2.2.3 Interferometry

Plane wave approximation (pwa) is a typical assumption exploited to perform interferometry and to compute interferometric phase ϕ. With reference to the geometry depicted in Figure 2.5, it leads to

$$\phi_1 = \frac{2\pi}{\lambda} \left(R_{2,1} - R_{1,1}\right) \approx -\frac{2\pi}{\lambda} B_{\mathrm{int}} \sin\left(\theta - \alpha\right) \tag{2.14}$$

where B_{int} is the interferometric baseline defined as the modulus of antenna separation vector and α is the baseline roll angle. In Equation (2.14) and following, ϕ_i represents the interferometric phase of the i-th point and $R_{j,i}$ the distance between j-th antenna and i-th point. Therefore, the differential phase between

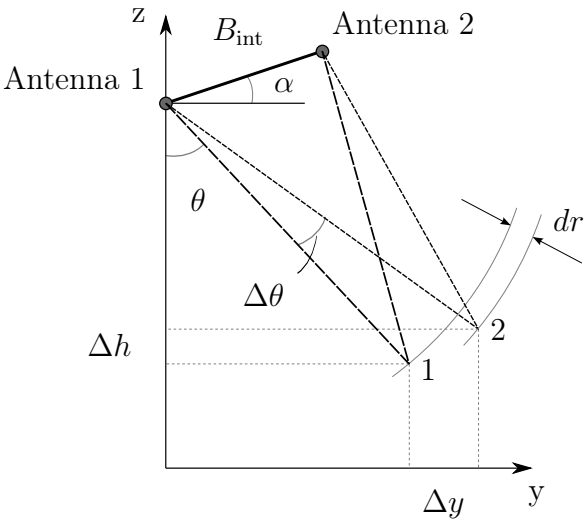

Figure 2.5: Interferometric observation geometry.

two points in adjacent range cells, with separation in height Δh and separation in slant range $dr = R_{1,2} - R_{1,1}$, is

$$\Delta\Phi_{\text{pwa}} = \phi_2 - \phi_1 = -\frac{2\pi}{\lambda} B_{\text{int}} \left[\sin\left(\Delta\theta + \theta - \alpha\right) - \sin\left(\theta - \alpha\right)\right] \tag{2.15}$$

where

$$\Delta\theta = \cos^{-1}\left(\frac{R_{1,1}\cos\theta - \Delta h}{R_{1,1} + dr}\right) - \theta \tag{2.16}$$

is the variation in off-nadir angle related to difference in height.

For a close range (cr) application, as the aim of present work is, plane wave approximation is not valid anymore. Hence, Equation (2.14) must be generalized as

$$\phi_1 = \frac{2\pi}{\lambda}\left(R_{2,1} - R_{1,1}\right) = \frac{2\pi}{\lambda}\left[\sqrt{R_{1,1}^2 + B_{\text{int}}^2 - R_{1,1}B_{\text{int}}\sin\left(\theta - \alpha\right)} - R_{1,1}\right] \tag{2.17}$$

thus leading to differential phase

$$\Delta\Phi_{\text{cr}} = \frac{2\pi}{\lambda}\left[\sqrt{R_{1,2}^2 + B_{\text{int}}^2 - R_{1,2}B_{\text{int}}\sin\left(\Delta\theta + \theta - \alpha\right)}\right.$$
$$\left. - \sqrt{R_{1,1}^2 + B_{int}^2 - R_{1,1}B_{\text{int}}\sin\left(\theta - \alpha\right)} + R_{1,1} - R_{1,2}\right] \tag{2.18}$$

The percentage error resulting from the adoption of plane wave approximation (2.15) in close range application can be calculated as

$$\varepsilon_{\Delta\Phi} = \frac{\Delta\Phi_{\mathrm{cr}} - \Delta\Phi_{\mathrm{pwa}}}{2\pi} \times 100 \tag{2.19}$$

Figure 2.6 shows the percentage error function for various of θ, $\Delta\theta$, B_{int} and R. The error increases for larger B_{int} and closer targets, as line of sight of two antennas become less and less parallel. Finally, increasing the off-nadir angle θ causes a shift of the function towards larger α, although, obviously, it is clear the periodic behavior of the function.

Interferometric Baseline

A new method to design the interferometric baseline for close range applications is required. Equation (2.18) does not allow B_{int} to be obtained directly from the other parameters, so it is necessary to address an indirect solution. The one hereby proposed envisages exploiting numerical representation of Equation (2.18), given a certain geometry, in function of a range of values for both B_{int} and α. One of the requirements for a correct reconstruction of height variation is that difference in phase between two adjacent pixel is no greater than 2π. Therefore, all the couples

$$(B_{\mathrm{int}}, \alpha) : \Delta\Phi_{\mathrm{cr}}\left(B_{\mathrm{int}}, \alpha\right) > 2\pi \tag{2.20}$$

are discarded, whereas all the other values could represent a good choice, depending on the application. The value of maximum allowable interferometric baseline

$$B_{\mathrm{int}} : \Delta\Phi_{\mathrm{cr}}\left(B_{\mathrm{int}}\right) = 2\pi \tag{2.21}$$

referred as critical baseline [23] is shown in Figures 2.7 and 2.8 for various operating conditions.

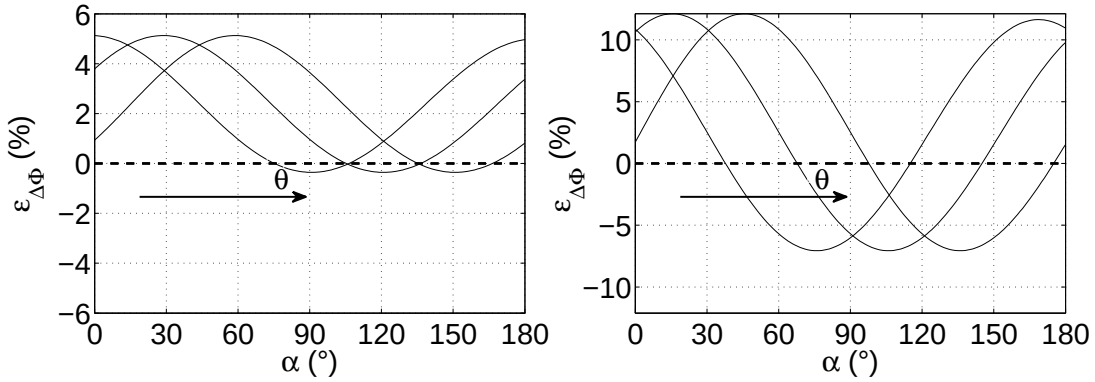

(a) $B_{\text{int}} = 3\text{cm}$, $R_{1,1} = 0.5\text{m}$, $\Delta\theta = 3°$ **(b)** $B_{\text{int}} = 3\text{cm}$, $R_{1,1} = 0.5\text{m}$, $\Delta\theta = 21°$

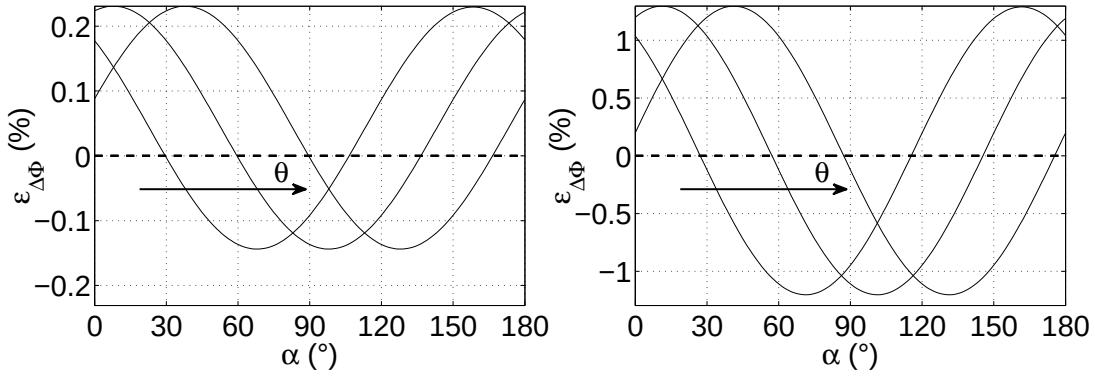

(c) $B_{\text{int}} = 3\text{cm}$, $R_{1,1} = 4.0\text{m}$, $\Delta\theta = 3°$ **(d)** $B_{\text{int}} = 3\text{cm}$, $R_{1,1} = 4.0\text{m}$, $\Delta\theta = 21°$

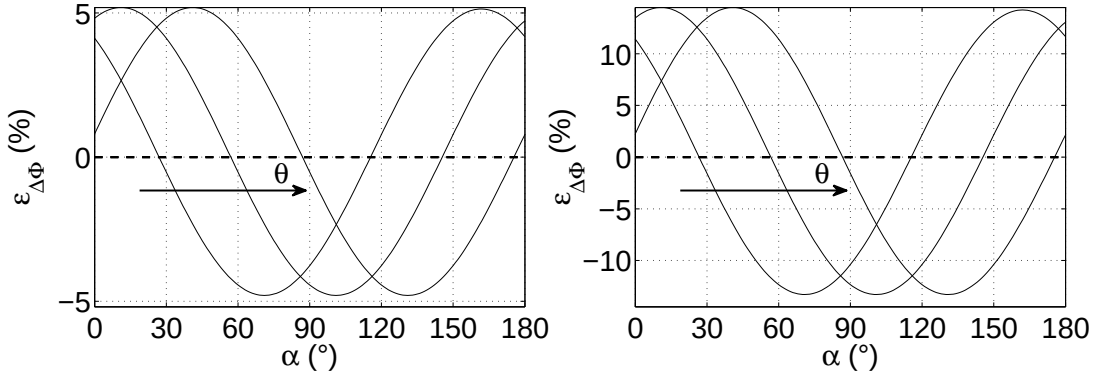

(e) $B_{\text{int}} = 6\text{cm}$, $R_{1,1} = 4.0\text{m}$, $\Delta\theta = 21°$ **(f)** $B_{\text{int}} = 10\text{cm}$, $R_{1,1} = 4.0\text{m}$, $\Delta\theta = 21°$

Figure 2.6: Percentage error between true and approximated differential interferometric phase under various operating conditions (the three curves correspond to $\theta = 15°$, $\theta = 45°$, $\theta = 75°$).

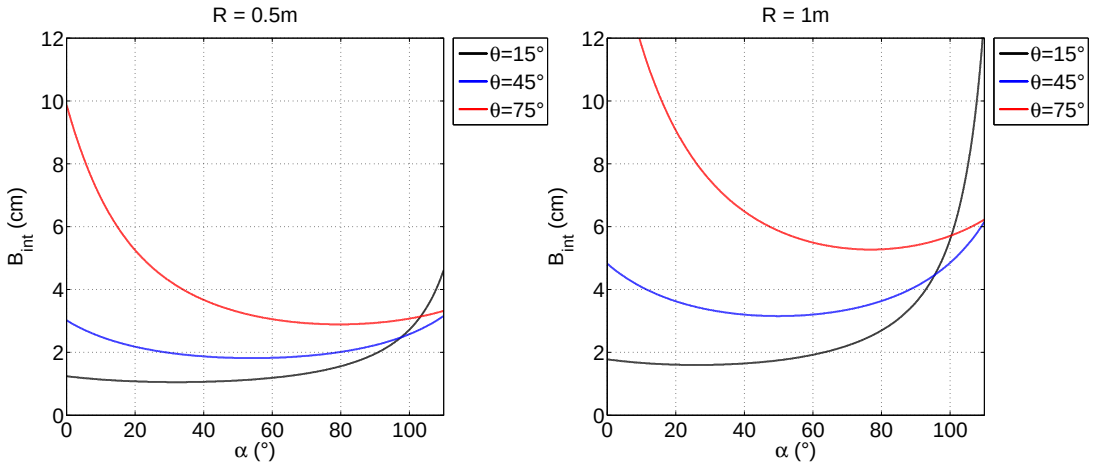

(a) $R_{1,1} = 0.5\text{m}$ **(b)** $R_{1,1} = 1\text{m}$

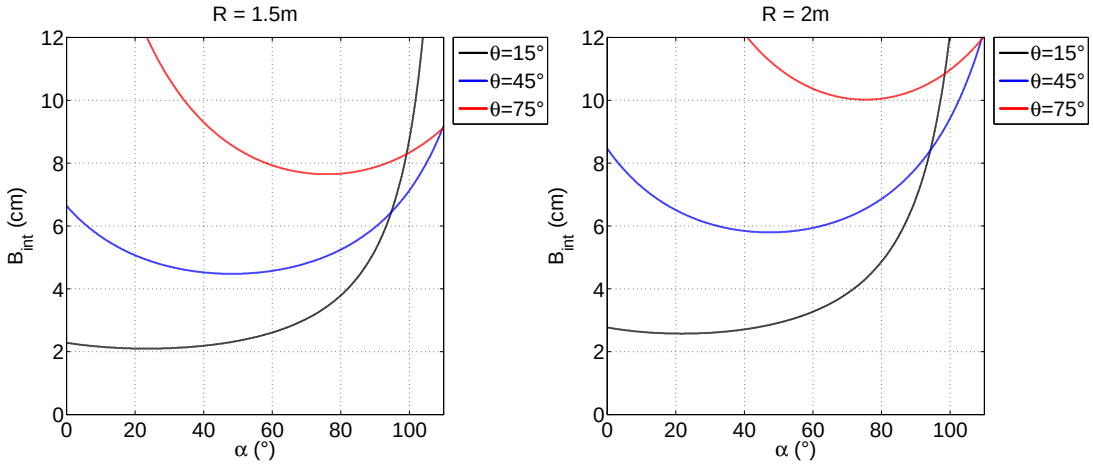

(c) $R_{1,1} = 1.5\text{m}$ **(d)** $R_{1,1} = 2\text{m}$

Figure 2.7: Critical baseline for various operating conditions. For each plot dr = 10 cm and $\Delta h = 10$ cm have been considered.

As expected, Figure 2.7 shows that when range increases, critical baseline increases as well. This means that, depending on size of antennas, a minimum interferometric baseline is achievable, thus imposing a bound on smallest distance at which it is possible to perform interferometry. Based on this consideration minimum values for $R_{\min}$ listed in Table 2.2 have to be update accordingly.

However, it has to be pointed out that this minimum distance is also strongly related to height variation between points in adjacent range cells. Namely, if Δh is smaller than expected, then interferometry can be performed at even smaller range distance (see Figure 2.8).

2.2.4 Design configuration

The most stringent input values from Table 2.2 have been chosen for theoretical three-dimensional resolution to propose a nominal design configuration. Furthermore, the envisaged mission profile, described in Chapter 1, contributed to choose both platform velocity v, small enough to move in unknown environments, and expected difference in height Δh, set equal to height resolution. Finally, the off-nadir angle θ, which influences both transmitted power P_T and interferometric performance, has been chosen so to achieve adequate baseline. It is worth noting that, being the radar designed to operate mainly indoors, at close range, then transmitted power is much lower than the values of existing compact, lightweight systems listed in Table 2.1. Nonetheless, the parameters reported in Table 2.4 must be considered as nominal ones. From the practical point of view, the system must be able to collect useful data under extremely different operating conditions depending on observation geometries, synthetic aperture formation, and effective baseline.

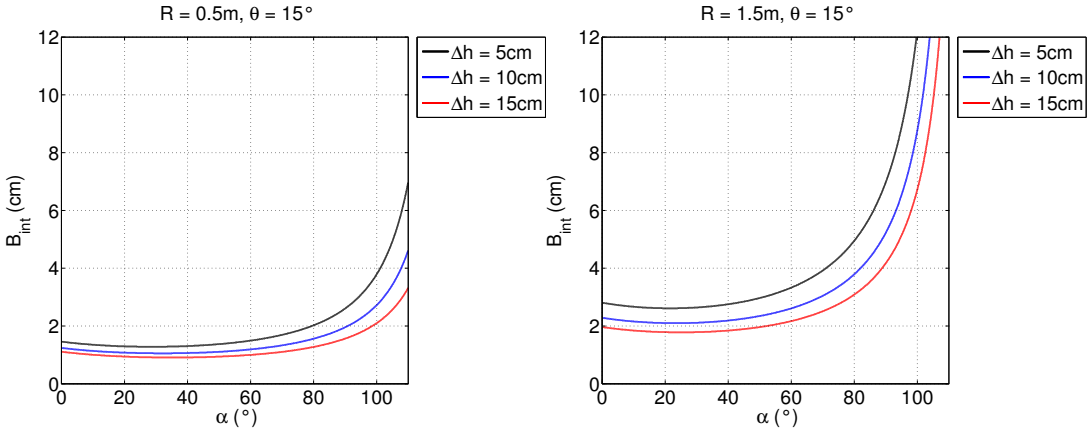

(a) $R_{1,1} = 0.5\text{m}, \theta = 15°$ **(b)** $R_{1,1} = 1.5\text{m}, \theta = 15°$

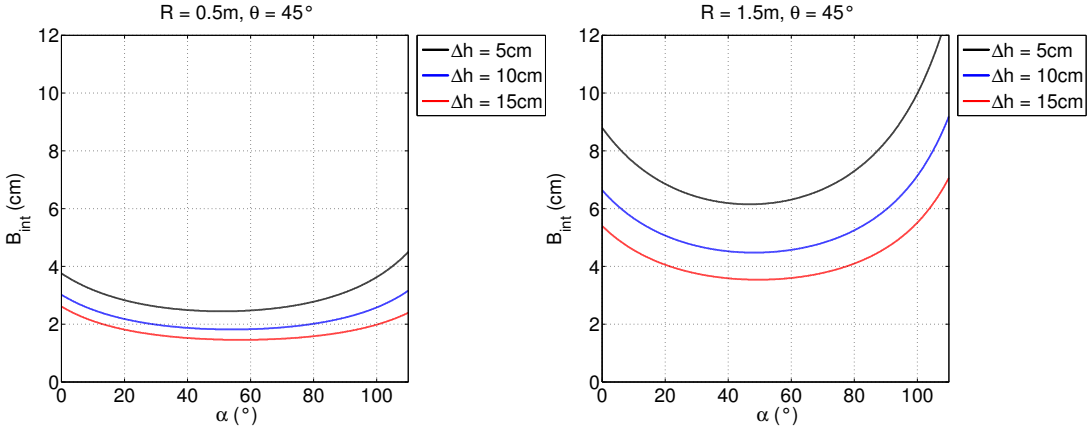

(c) $R_{1,1} = 0.5\text{m}, \theta = 45°$ **(d)** $R_{1,1} = 1.5\text{m}, \theta = 45°$

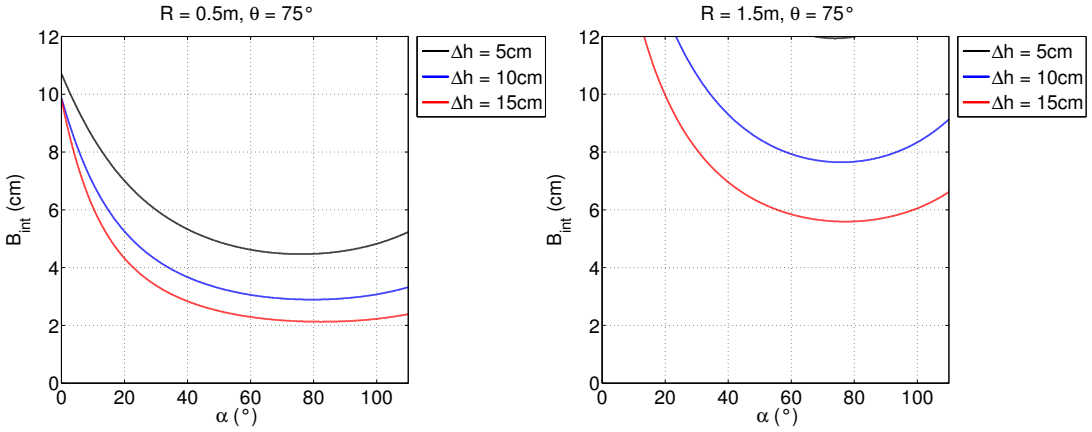

(e) $R_{1,1} = 0.5\text{m}, \theta = 75°$ **(f)** $R_{1,1} = 1.5\text{m}, \theta = 75°$

Figure 2.8: Effect of height variation on critical baseline. For each plot $dr = 10$ cm has been considered.

Table 2.4: Selected working parameters.

Symbol	**Parameter**	**Unit**	**Value**
dr	Range resolution	(cm)	10
da	Azimuth resolution	(cm)	10
v	Platform velocity	($\mathrm{m\,s^{-1}}$)	0.50
θ	Off-nadir angle	(°)	60
R_{max}	Maximum range	(m)	30
R_{min}	Minimum range	(m)	1.5
N_{BIT}	Number of bits		16
dh	Height resolution	(cm)	10
B	Transmitted bandwidth	(GHz)	1.50
f_S	Sampling frequency	(kHz)	200
PRF	Pulse Repetition Frequency	(Hz)	250
d	antenna width	(m)	0.01
θ_{r}	antenna beamwidth in elevation	(°)	18
l_{az}	antenna length	(m)	0.02
θ_{az}	antenna beamwidth in azimuth	(°)	9
P_T	Transmitted Power	(mW)	<1
α	Baseline roll angle	(°)	40
B_{int}	Interferometric Baseline	(cm)	3
$\Delta\phi$	Phase Resolution at interferometer	(°)	11
Δh	Height difference between two points in adjacent range cells	(cm)	10

Chapter 3

mm-wave InSAR simulation

The development of a software simulation environment is a key asset for successful analysis of MMW FMCW InSAR behavior in envisaged scenarios. Software-based tests, indeed, can prove effectiveness of design procedure and help in further understanding issues or problems connected to the novel sensor. In this Chapter main features and operative blocks of simulator are described. Main attention is given to scene generation process, which is also able to model indoor reflection thanks to a modified Ray Tracing algorithm.

3.1 Simulation Environment

The logic behind software simulator realized in this work is illustrated in schematic of Figure 3.1. The inputs, represented by white boxes, are parameters which depend on radar design, selected scene, and navigation information. These data are given to the blocks that perform simulation steps, represented as gray squares in Figure 3.1. The *Scene Simulator* block generates the beat signal provided by designed FMCW radar that illuminates the simulated scene and moves according to navigation information. *Data Processing* block, instead, performs SAR processing. It is worth noting that the latter block has been developed to read

and process not only simulated but also real raw data, thus providing focused SAR images even for real scenery. Finally, white rounded boxes are the outputs of simulator, *i.e.*, raw data matrix, focused data matrix and information about geometric ambiguities in the scene. The last output is necessary because envisaged missions, differently from most of conventional remote sensing applications, require the system to observe scene along directions that could be not perpendicular to the motion of platform, that is, regions in which image resolution can be degraded notably. Hence, guidelines for trajectory optimization and mission profile can be drawn.

Further insights about the inputs blocks are necessary. Each operational scenario can be conceived as a control volume that encloses platform and manifold targets. Dimensions of control volume depends on the application. Typical operational environment for the proposed system is well represented by a parallelepiped as depicted in Figures 3.2-3.3. Specifically, concerning indoor exploration, this parallelepiped can represent an example of a warehouse in which the sensor is requested to operate. The same scenario is valid also for planetary exploration, where the parallelepiped can be conceived as a relatively small control volume that encloses scatterers which vary depending on application. A fixed reference system xyz, whose axes coincide with three main dimensions of control volume, is created. Dimensions of the environment for a general indoor mission are listed in in Table 3.1. In the environment are placed also the targets. Their position and velocity are provided, as well as their radar cross section. In this work all targets are treated as points and extended targets are simulated by increasing the number of point targets per resolution cell. Furthermore, fluctuating targets and multiple reflections, which can become relevant in a close-range and MMW-based application, are also simulated. It is worth noting that attenuation due to millimeter-wave effects is not simulated in this work, even though it can be taken into account when dealing with simulations of

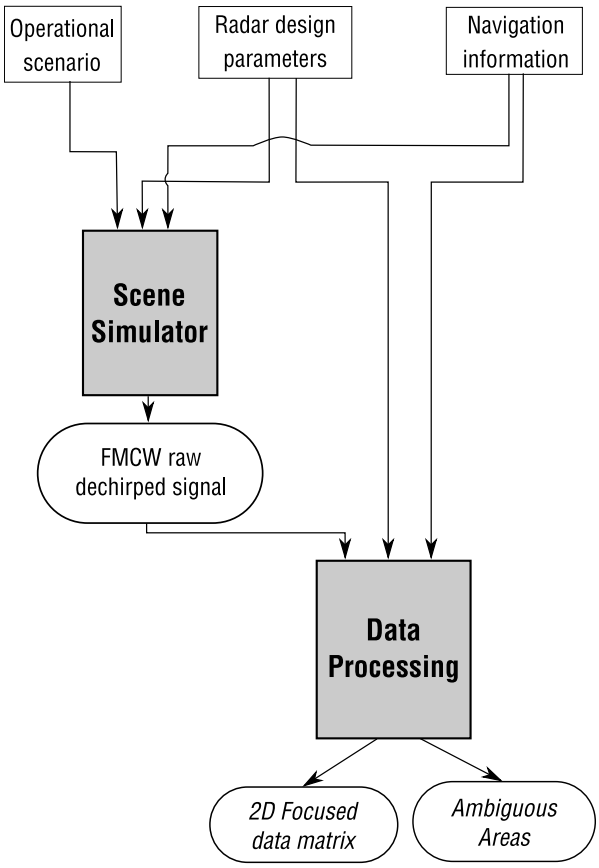

Figure 3.1: Block scheme for software system simulator.

environments filled with smoke or flames. Design parameters include both nominal parameters for radar sensor and mission requirements. Finally, the block represented by navigation information provides the simulator with information about position, velocity and attitude of the platform. In real operations, these data are provided by UAS navigation unit, which is connected to Processing Unit via direct interface data link. It is worth noting that navigation data are also necessary to support image processing and data extraction.

The content of each simulation block is explained in details in the following of the chapter.

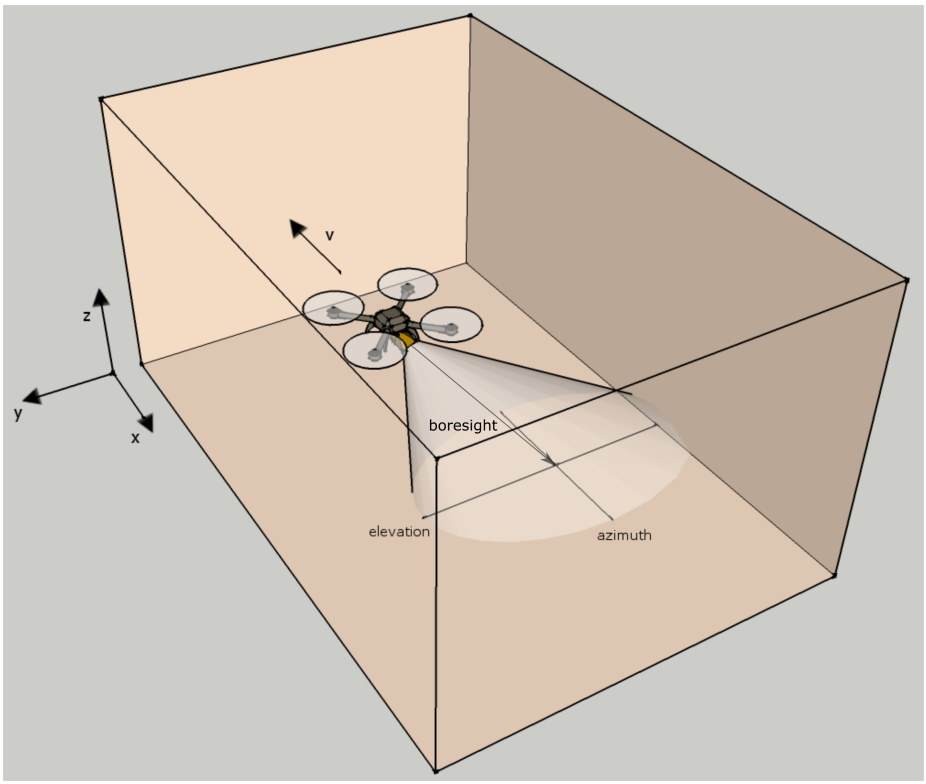

Figure 3.2: 3D view of analyzed scenario.

Table 3.1: Dimensions of control volume

x (m)	y (m)	z (m)
30	10	6

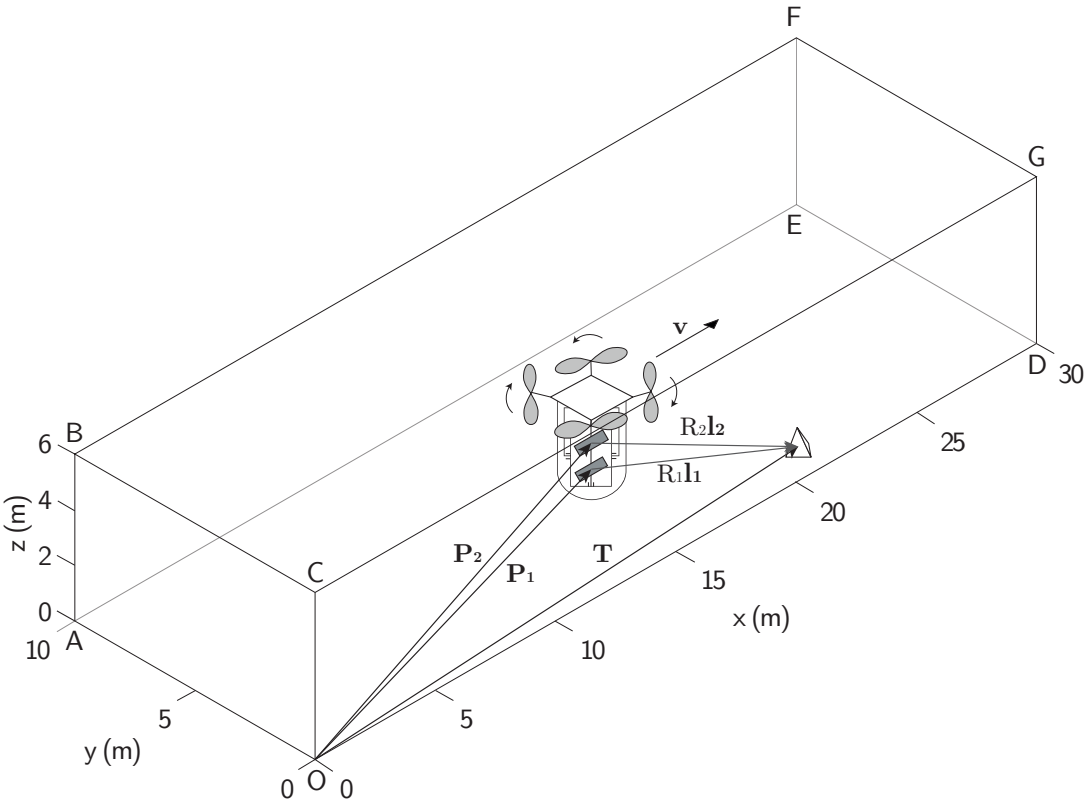

Figure 3.3: Platform and sensor moving in simplified operational scenario. Platform and target position vectors, line of sight unit vector, velocity vector, and target distance to antennas are depicted, too. Dimensions are not to scale for clarity.

3.2 Scene Generation

The scene generator is the most important block as it reproduces the FMCW raw radar signal of an envisaged scenery.

3.2.1 Point Target

For a quasi-monostatic setup (*i.e.* transmitting and receiving antennas are not physically located in the same position but the operational distance is so that a monostatic configuration approximation is valid) and neglecting effect of signal amplitude, a point target at distance R_T is described by the beat signal

$$s_B(t) = A\,\mathrm{rect}\left(\frac{t-\tau}{T}\right)\exp\left\{2\pi j\left(f_C\tau + \frac{B\tau}{T}t\right)\right\} \tag{3.1}$$

where t is the time, T is the sweep duration, the time delay due to distance is $\tau = \dfrac{2R_T}{c}$, and c is the light velocity. In Equation (3.1) RVP contribution has been considered negligible [77]. When multiple point targets are addressed, Equation (3.1) becomes

$$s_B(t) = \sum_{i=1}^{M} A_i\,\mathrm{rect}\left(\frac{t-\tau_i}{T}\right)\exp\left\{2\pi j\left(f_C\tau_i + \frac{B\tau_i}{T}t\right)\right\} \tag{3.2}$$

where M is the number of point targets. The *Scene Simulator* block rearranges signals (3.1)-(3.2) in a 2D complex-value matrix, whose i-th row represents echoes corresponding to i-th transmitted sweep.

It is worth noting that the line-of-sight, or boresight, $\mathbf{l}$ is obtained in the fixed reference xyz from the knowledge of platform attitude and observation geometry by means of products of rotation matrix. Indeed, the observation geometry represents the relative attitude of antennas with respect to platform.

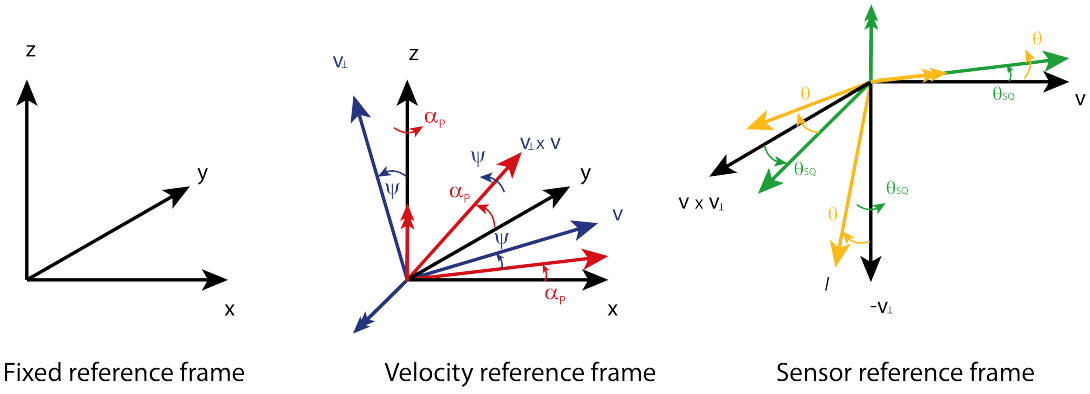

Figure 3.4: Reference frames and rotations.

Therefore, the explicit expression for $\mathbf{l}$ is

$$\mathbf{l} = \begin{bmatrix} -s(\theta_{sq})\, s(\theta)\, c(\psi)\, c(\alpha_P) - c(\theta_{sq})\, s(\psi)\, c(\alpha_P) - s(\theta_{sq})\, c(\theta)\, s(\alpha_P) \\ c(\theta_{sq})\, s(\theta)\, c(\psi)\, c(\alpha_P) - s(\theta_{sq})\, s(\psi)\, c(\alpha_P) + c(\theta_{sq})\, s(\theta)\, s(\alpha_P) \\ s(\theta)\, s(\alpha_P) - c(\theta)\, c(\psi)\, c(\alpha_P) \end{bmatrix} \tag{3.3}$$

where $c(\cdot)$ and $s(\cdot)$ represent cosine and sine functions, θ is off-nadir angle, θ_{sq} represents squint angle, α_P and ψ are the pitch and heading angle, respectively. Figure 3.4 shows reference frames and angles.

Fluctuating Target

In order to model a fluctuating point target it is necessary to introduce image speckle. The implemented approach simulates extended targets, like background, as more point targets in a single resolution cell [94]. In addition, the beat signal (3.2) is modified to account for the statistical properties of amplitude and phase of the background

$$\begin{aligned} s_B(t) =& A \operatorname{rect}\left(\frac{t-\tau}{T}\right) \exp\left\{2\pi j\left(f_C\tau + \frac{B\tau}{T}t\right)\right\} + \\ &+ \sum_{i=1}^{M_B} A_i \operatorname{rect}\left(\frac{t-\tau_i}{T}\right) \exp\left\{2\pi j\left(f_C\tau_i + \frac{B\tau_i}{T}t + \varphi_i\right)\right\} \end{aligned} \tag{3.4}$$

where A_i follows a Rayleigh distribution, depending on clutter RCS and varying on a pulse-by-pulse basis, and φ_i is an uniform phase distribution in $[0, 2\pi]$ [94]. It is worth noting that, following traditional SAR and radar literature, statistical distribution is valid only for background, whereas point targets not representing background have deterministic amplitude and phase.

3.2.2 Ray-Tracing

Reflections and diffraction phenomena could have strong impact on measurements when dealing with indoor and close-range radar applications, because multipath due to multiple reflections can occur in these scenarios. Therefore, data interpretation and analysis can benefit notably from the simulation of these physical mechanisms from both the geometric and radiometric point of view. Radiometric issues are handled by taking into account a double-lobe scattering model [78], which is able to address both scattering and reflections from extended areas. Ray Tracing (RT) algorithm is selected for dealing with geometric issues. Indeed, it follows a ray from transmission point to receiving point through resolution cells of the domain and allows the simulator to model reflection, refractions and shadows [79]. Moreover, it also provides the users with information about ray intersection with other objects in the scene. RT algorithms have been exploited for analysis of several sensors, e.g. laser [80], lidar [81],[82], radar [83],[84],[85], and applications, e.g. scene rendering and indoor wireless net design [86],[87],[88]. With specific reference to SAR imaging, it is worth noting that SAR simulators have been typically developed under the assumption of parallel rays [83],[84], which is an adequate approximation for standard remote sensing applications. However, the assumption of parallel rays is, in general, not valid for indoor applications due to short distances to travel. Hence, new approaches for indoor SAR raw data simulation are necessary.

2D geometry

The first step towards understanding the effects of indoor scattering and reflection phenomena on radar returns is a two-dimensional simulation, that is, a simulation in which echoes coming from points at different azimuth position with respect to the antenna are neglected. Indeed, even though this is not a real case, it will be shown that it helps in defining geometries and analyzing system behavior. The core of this block is an adaptation of the ray tracing algorithm proposed in [79], which is restricted to y-z plane. It is clear that with the same approach even x-y and x-z planes can be analyzed. A grid is created and the size of each cell of the grid is set as an input parameter. In the present implementation, each cell is a square and the grid is uniform but either different sampling steps for each direction or non-uniform grid distribution can be easily implemented. It is worth noting that size of cell should be smaller than expected resolution for realistic simulations. The origin of the rays is the center of the transmitting antennas and the rays are uniformly distributed around the line-of-sight direction $\mathbf{l}$ and within the beamwidth θ_R. It is worth recalling that the assumption of parallel rays [83],[84] is not used in this work owing to short distances to travel when dealing with indoor applications. Objects in the scene are modeled by assigning specific parameters to the cells whose position in the grid corresponds to position of the objects. The elements which are always present in the grid are the walls, the antennas, and the propagating medium. As shown in Figure 3.5, each of them is identified by an integer number, corresponding both to different values of normal vector and action required. Actions and normal vectors are listed in Table 3.2. It can be seen that if the ray is in the cell corresponding to the propagating medium, air in the present work, then there is no normal vector and the ray is free to travel along its path. On the contrary, if the ray reaches a cell corresponding to a wall, specular reflection mechanism is enabled. In particular, the direction of reflected ray is found according to the

formula

$$\mathbf{r} = \frac{\mathbf{d} - 2\,(\mathbf{d} \cdot \mathbf{n})\,\mathbf{n}}{|\mathbf{d} - 2\,(\mathbf{d} \cdot \mathbf{n})\,\mathbf{n}|} \tag{3.5}$$

where $\mathbf{d}$ is the direction of the impinging ray and $\mathbf{n}$ is the direction normal to the considered surface. Similarly, reflection on a random object in the scene can be simulated by association with normal vectors to cells, as shown in Figure 3.6. It is worth noting that the simulator counts how many times a ray hits either a wall or an object within the scene. The maximum allowable number of hits, N_{HITS}, before halting the ray is directly related to the number of specular reflections, $N_{\text{REFLECTION}}$, by the simple equation

$$N_{\text{REFLECTION}} = N_{\text{HITS}} - 1 \tag{3.6}$$

The assumption of two specular reflections has been formulated, so that the number of hits is three. This assumption derives from the observation that after three bounces the signal has lost most of its power owing to absorption and spread of energy. Finally, in order to model antenna effect, when the ray hits a cell filled with antenna identifier the ray itself is always halted; also, the reflection is received by the antenna only if the direction is within the beam of radar, *i.e.*

$$\mathbf{l} \cdot \mathbf{r} < -\,|\cos\,(\theta_R)| \tag{3.7}$$

where the sign "-" is due to the fact that line-of-sight and ray directions have opposite verse when the ray impinges on the antenna. Figure 3.7 shows a set of rays stopped by the antenna: in general, owing to the divergence of rays, the smallest is the distance travelled by the rays when hitting the antenna, the largest is the number of them whose path is blocked.

It is worth noting that diffraction phenomena can be modeled, too [89].

A relevant role in the proposed simulator is also played by radiometric effects. Indeed, once the geometric paths have been set, it is necessary to simulate how much energy is associated with diffusion, reflection, and absorption by the

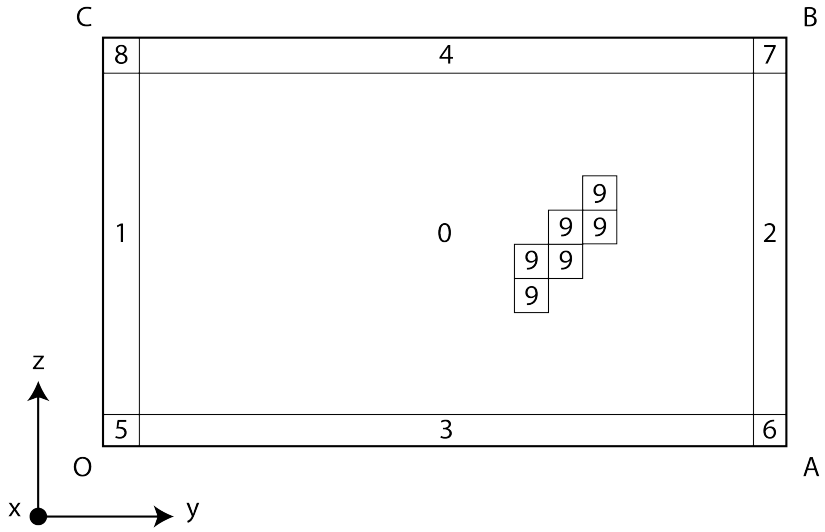

Figure 3.5: Schematic of 2D grid values. Areas associated to value 0 represent the propagating medium; cells having values ranging from 1 to 8 are the walls. Receiving antenna is represented by value 9. Size of cells is not to scale for clarity.

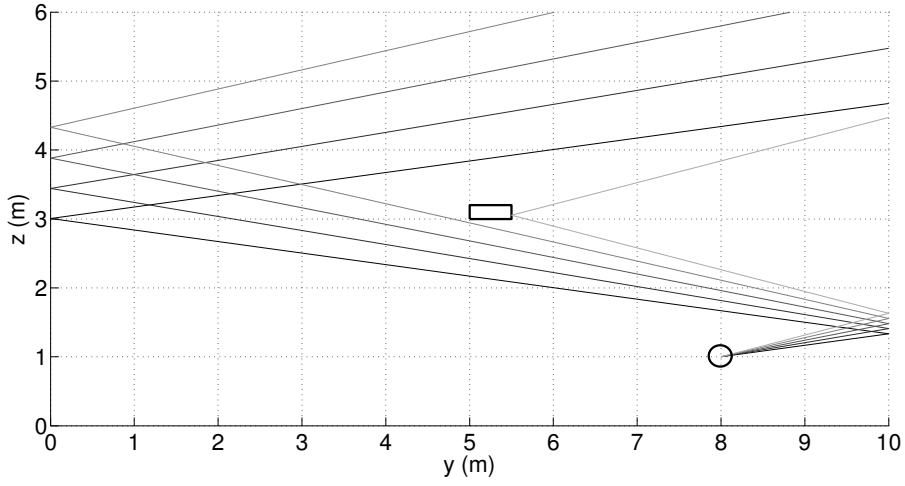

Figure 3.6: Example of reflections due to an object (rectangle, bold) in the scene. Position of antennas is revealed by black circle.

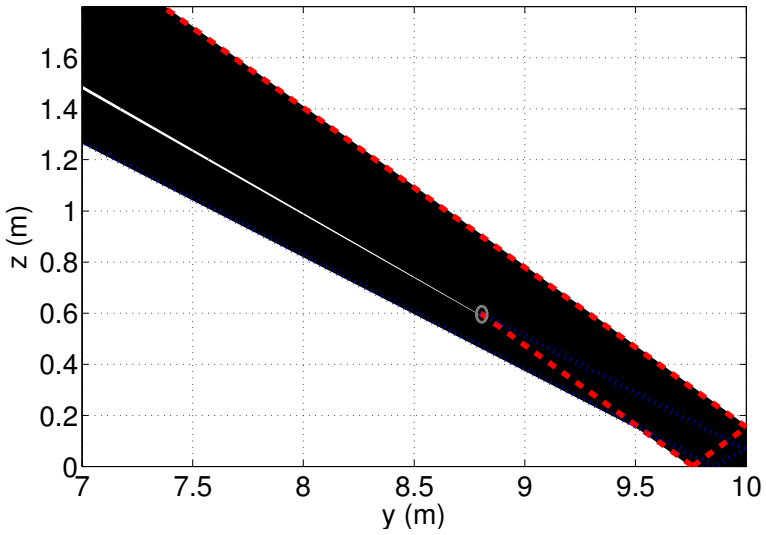

Figure 3.7: 2D geometry: example of rays intercepted by receiving antenna. Transmitting and receiving antennas are oriented towards the bottom-right corner and gray circle shows their location. Blue dotted and red dashed rays indicate the borders of transmitted beam, whereas inner rays are depicted in black. The energy is reflected back to both the antenna and the top-left corner: some rays hit the antennas, hence they are not propagated towards the top-left side of the grid (transparent area). The figure represents a detail of the total grid.

Table 3.2: Set of basic actions required in 2D RT algorithm.

Identifier	Normal vector	Action
0	Null	Keep on propagating
1	$\mathbf{n} = [1, 0]$	Compute new direction and increase hit counter
2	$\mathbf{n} = [-1, 0]$	Compute new direction and increase hit counter
3	$\mathbf{n} = [0, 1]$	Compute new direction and increase hit counter
4	$\mathbf{n} = [0, -1]$	Compute new direction and increase hit counter
5	$\mathbf{n} = \left[\frac{1}{\sqrt{2}}, \frac{1}{\sqrt{2}}\right]$	Compute new direction and increase hit counter
6	$\mathbf{n} = \left[-\frac{1}{\sqrt{2}}, \frac{1}{\sqrt{2}}\right]$	Compute new direction and increase hit counter
7	$\mathbf{n} = \left[-\frac{1}{\sqrt{2}}, -\frac{1}{\sqrt{2}}\right]$	Compute new direction and increase hit counter
8	$\mathbf{n} = \left[\frac{1}{\sqrt{2}}, -\frac{1}{\sqrt{2}}\right]$	Compute new direction and increase hit counter
9	$\mathbf{l}$	Stop ray

scatterer. In general, a geometric definition of reflectance factor R_{fac} by means of reflectance function, also called Bidirectional Reflectance Density Function (BRDF), requires the knowledge of the variation of BRDF itself with impact point and directions of both incident and scattered rays [90]. In addition, this value depends on several other parameters. The first one is the polarization of emitted wave: indeed, depending on the direction of polarization, different equations for reflectance factor are provided and R_{fac} can also become equal to zero in correspondence of Brewster's angle [91]. Then, the wavelength could significantly change reflectance values, especially when dealing with materials with strong internal scattering [90]. Surface roughness has also a role in scattering phenomena as when it is not negligible when compared with the wavelength of the incident rays, the energy is scattered more in millimeter wave than at lower frequencies [86]. Several models exist for simulating the radiometric behavior of different kinds of environments [85],[86],[92],[93]. The one hereby adopted is

an adaptation of double-lobe model proposed in [78], which has been used for taking into account realistic diffusive phenomenology in RT. The adaptation lies in the fact that a single ray is supposed to be scattered from the point where the incoming ray impinges, instead of a fan of rays. In details, when the transmitted ray hit the surface the power balance is

$$1 = \frac{P_L}{P_i} + \Gamma^2 \left(K_S^2 + K_R^2 \right) \tag{3.8}$$

where P_L is the power loss due to absorption/transmission and P_i is the incident power, K_S is the scattering coefficient with respect to reflected energy, K_R represents the reflection reduction factor coefficient and Γ^2 the reflected power with respect to incident power. The ratio $\frac{P_L}{P_i}$ is the transmission loss and depends on the wavelength, on the material of walls and roughness, too. Incident power can be described as

$$P_i = \frac{1}{4\pi R^2} G_T P_T \sigma \tag{3.9}$$

being R the distance, G_T the transmitting antenna gain, P_T the transmitted power, and σ the radar cross section (RCS). Therefore the scattering coefficient can be computed as

$$K_S = \sqrt{1 - K_R^2} \tag{3.10}$$

In addition, according to the double-lobe model [78], here reported for sake of clarity, scattered energy can be described as

$$E_S^2 = E_{S,0}^2 \left[\Lambda \left(\frac{1 + \cos \psi_B}{2} \right)^{\alpha_B} + (1 - \Lambda) \left(\frac{1 + \cos \psi_F}{2} \right)^{\alpha_F} \right] \tag{3.11}$$

where $E_{S,0}$ is the maximum scattered energy, Λ is the percentage of backscattered energy, ψ_B and ψ_F represent the difference between angle of back- and forward-specular scattering and the actual ray direction, α_B and α_F are factors that take into account the size of the beams. Scattering factor K_S is within the definition of maximum scattered energy. With the aforementioned approximation a quantity Λ of the whole scattered energy is given to backscattering contribution whereas

the remaining $(1 - \Lambda)$ amount and reflected energy are assigned to reflected rays. In addition, a further parameter is multiplied by the reflected energy, *i.e.*

$$L_{RX} = \frac{N_{\text{REFLECTED}}}{N_{\text{RAYS}}} \tag{3.12}$$

which represents the amount of reflected energy that reaches the receiving antenna, due to ray divergence. It is important to note that no backscattering returns coming from second and third hits are considered in this simulations. This approximation is due to the fact that the walls are supposed to have a uniform and very low radar cross section, therefore the energy backscattered from points hit by reflected rays is negligible. This issue will be further discussed when showing results of simulation. However, if bright targets, showing a larger value of RCS, are present in an actual scene, this approximation could be not valid. Indeed, ghost signatures due to multiple backscattered reflections from bright target not in line of sight could appear in the image, as in [91], thus causing misleading interpretation of the image itself. Finally, it is worth highlighting that, even though it is available in the framework of the simulator, fluctuating model has not been applied to 2D and 3D analyses as the principal objective is to assess dominant element in an uniform scene.

3D geometry

The 3D RT simulator is the natural extension of two-dimensional techniques discussed in previous subsection. In details, azimuthal components are enabled and squint-looking observations are allowed. Again, it is possible to set dimensions of grid voxels to be both uniform and non-uniform and reflections in the domain are computed according to Equation (3.4), even though the list of identifiers takes into account surfaces besides edges and vertices. It is worth noting that the set of actions for modeling reflections by Equation (3.5) is more complex as it handles also beamwidth in azimuth. Figure 3.8 shows a 3D scene with ray reflections scene.

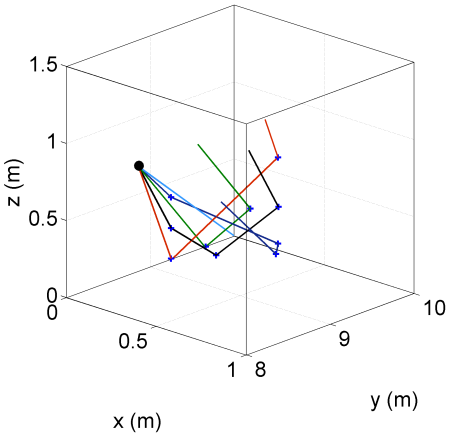

Figure 3.8: 3D view of reflected rays: black dot represents the position of antennas, blue crosses are the points where reflection occurs. Only a small part of the whole control volume is shown, for clarity.

For 3D simulations, rays are emitted for each position occupied by the transmitting antenna during the synthetic aperture must be modeled thus properly simulating FMCW raw SAR signals. In addition, being possible to observe multiple reflections from trihedral corners, the maximum number of reflections has been raised to three.

3.3 Processing

SAR focusing algorithms are well assessed in literature for conventional SAR. As for FMCW SAR, the trend is growing. However, it is useful to recall equations for each algorithm, highlighting advantages and disadvantages.

The standard implementation of these algorithms, *i.e.* referred to pulsed radar operation, has been extended to an FMCW architecture following the results presented in [26],[95]-[97].

3.3.1 Time-domain algorithms

Time-domain processing is based on the time correlation between the received signal and a reference signal in the slow time. The focused azimuth signal can be expressed as:

$$\sigma\left(\mathbf{r}_{\mathrm{T}}\right)=\int_{T_{\mathrm{int}}} s_C(\mathbf{r}_{\mathrm{T}},t_N)s^*_{\mathrm{Ref,az}}(\mathbf{r}_{\mathrm{T}},t_N)dt_N \tag{3.13}$$

in which $s^*_{\mathrm{Ref,az}}$ is the slow time reference function and T_{int} is the total coherent integration time. Equation (3.13) shows that the focused signal is maximized for a target located in the point for which the reference function is designed, whereas the contribution of the other target is cut down. In addition, it is worth noting that Equation (3.13) can be exploited for any shape trajectory, thus easing motion compensation strategies, and the effects of target Doppler history are accounted for when dealing with explicit formulation of reference function $s^*_{\mathrm{Ref,az}}$. It is clear from Equation (3.13) that correlation has to be done for each target location $\mathbf{r}_{\mathrm{T}}$. Hence, in principle a three-dimensional image can be obtained [98]. However, imaged points are usually restricted to a single plane, even though this could affect image understanding when target elevation is relevant.

Classic Back-Projection Algorithm

In [99] it is proposed a Back-Projection Algorithm (BPA), referred to as *pulse-by-pulse correlation imaging*, for bistatic SAR as:

$$\sigma\left(\mathbf{r}_{\mathrm{T}}\right)=\sum_n W\left(\mathbf{r}_{\mathrm{T}},n\right)s_C\left(\mathbf{r}_{\mathrm{T}},n\right)\exp\left\{j\frac{2\pi}{\lambda}\left[D_{Tx}\left(\mathbf{r}_{\mathrm{T}},\mathbf{r}_0,n\right)+D_{Rx}\left(\mathbf{r}_{\mathrm{T}},\mathbf{r}_0,n\right)\right]\right\} \tag{3.14}$$

where D is the relative range with respect to a reference point $\mathbf{r}_0$ in the image and W is a window function to suppress returns from sidelobes.

In [100] back-projection method for spotlight-mode SAR is derived as:

$$\sigma(\rho,\phi)=\frac{1}{4\pi^2}\int_{-\pi/2}^{\pi/2}\int_{-\infty}^{\infty}S(f,\theta_{\text{look}})\,|f|\exp\{j\rho f cos(\phi-\theta_{\text{look}})\}\,df d\theta \quad (3.15)$$

where θ_{look} represents the angle under which the target is observed and it is connected to slow time. Practically, range-compressed signals are taken in Polar Format and distributed over an annulus in the frequency domain defined by $f_{\min} \geq f \geq f_{\max}$ and $\theta_{\text{look,min}} \geq \theta_{\text{look}} \geq \theta_{\text{look,max}}$. Therefore, this method is useful when dealing with either spotlight or bistatic data. The back-projection algorithm is the discrete implementation of Equation (3.15) and it can be demonstrated as in [101] that Equation (3.15) is equivalent to Equation (3.13). It is worth noting that the ramp filter is necessary for a correct reconstruction of the signal as it cuts out lower frequencies, which cause blurring, even though it introduces also a noise.

In [95] it is proposed a BPA for FMCW SAR under the assumption of validity of stop-start approximation

$$\sigma(\mathbf{r}_{\text{T}})=\sum_{n}W(\mathbf{r}_{\text{T}},n)\,s_C(\mathbf{r}_{\text{T}},n)\exp\left\{-j\frac{2\pi}{\lambda}\left[D_{Tx}(\mathbf{r}_{\text{T}},\mathbf{r}_{\text{c}},n)+D_{Rx}(\mathbf{r}_{\text{T}},\mathbf{r}_{\text{c}},n)\right]\right\} \quad (3.16)$$

where $\mathbf{r}_{\text{c}}$ is the point at center scene and n is the pulse index, which is related to slow time by the relation $t_N = nPRI$.

The algorithms expressed by Equations (3.14)-(3.16) share a computational cost of $O(N|R_D|)$, where N is the number of pulses and $|R_D|$ is the number of points at which the reflectivity is evaluated.

Fast Back-Projection Algorithm

Either computational burden or approximations made could limit the exploitation of BPA to not real-time applications. However, the capability to focus data whatever the geometry makes this algorithm interesting and some efforts done

to reduce the number of operation without a significant drop in resolution are presented hereby.

The Fast Back-Projection Algorithm (FBPA) has been proposed in order to decrease the computational cost, which is usually not suitable with real-time applications [98]. FBPA divides the synthetic aperture in several subapertures first, *i.e.*, Equation (3.13) is rewritten as

$$\sigma\left(\mathbf{r}_{\mathrm{T}}\right)=\sum_{i=1}^{N_{\mathrm{sub}}}\sigma_{i}\left(\mathbf{r}_{\mathrm{T}}\right) \tag{3.17}$$

The images from each subaperture, $\sigma_{i}\left(\mathbf{r}_{\mathrm{T}}\right)$, have low cross-range resolution. Therefore, a coarser pixel grid in cross-range direction can be exploited to process the data, thus simplifying computational load. It is worth noting that it is convenient to use a polar grid, in order to avoid aliasing. The final image, having full resolution in both direction, is achieved by upsampling and coherently adding each subaperture image. This algorithm reduces $\sqrt{N}$ times the computational load for an $N\times N$ grid.

FMCW Modified BPA

A FMCW-based BPA has been presented in Equation (3.16). However, it can be applied only when start-stop approximation is valid and this is not always true for FMCW operations. In [95] distance to target $d\left(\mathbf{r}_{\mathrm{T}},n,t\right)=R_{Tx}\left(\mathbf{r}_{\mathrm{T}},n,t\right)+R_{Rx}\left(\mathbf{r}_{\mathrm{T}},n,t\right)$ is approximated as

$$d\left(\mathbf{r}_{\mathrm{T}},n,t\right)\approx d\left(\mathbf{r}_{\mathrm{T}},n,0\right)+v_{\mathbf{r}_{\mathrm{T}},n,0}t=d\left(\mathbf{r}_{\mathrm{T}},n\right)+v_{\mathbf{r}_{\mathrm{T}},n}t \tag{3.18}$$

where $v_{\mathbf{r}_{\mathrm{T}},n}=\left.\dfrac{\partial d\left(\mathbf{r}_{\mathrm{T}},n,t\right)}{\partial t}\right|_{t=0}$.

With approximation (3.18), the algorithm becomes

$$\sigma\left(\mathbf{r}_{\mathrm{T}}\right)=\sum_{n}W\left(\mathbf{r}_{\mathrm{T}},n\right)S\left(f+f_{D}\right)\exp\left\{-j\frac{2\pi}{\lambda}\left[D_{Tx}\left(\mathbf{r}_{\mathrm{T}},\mathbf{r}_{\mathrm{c}},n\right)+D_{Rx}\left(\mathbf{r}_{\mathrm{T}},\mathbf{r}_{\mathrm{c}},n\right)\right]\right\} \tag{3.19}$$

where f_D is the Doppler shift induced by continuous motion. Therefore, Doppler effects should be taken into account during range compression to correctly focus image.

3.3.2 Frequency-domain Algorithms

Wavenumber Domain Algorithm

Wavenumber-domain algorithm (WDA), also known as *Omega-K* Algorithm focuses data in the two-dimensional frequency domain and allows both to handle high squint angles and to deal with range-azimuth coupling. Basic steps for this algorithm are two-dimensional Fourier transform, reference function multiplication, Stolt interpolation in the frequency domain and two-dimensional inverse Fourier transform [102].

In [97] it is proposed a method to focus FMCW SAR data by omega-k. First, beat signal s_B is subject to a change of variable from fast time to range frequency. Then, the signal is Fourier transformed in azimuth direction and resulting phase is

$$\Phi = -\frac{4\pi R_0}{c}\sqrt{(f_C + f_{AZ})^2 - \left(\frac{c f_{AZ}}{2v}\right)^2} - \frac{\pi f_R^2}{K_R} \tag{3.20}$$

where f_R and f_AZ are range and azimuth frequencies, and includes range-azimuth coupling and range walk due to continuous motion during transmission/reception.

First focusing step, also known as bulk compression, is achieved by reference function multiplication in order to remove range invariant terms. The reference function is

$$\begin{aligned} H_{RFM} = &\exp\left[-\frac{4j\pi R_{ref}}{c}\sqrt{(f_C + f_{AZ})^2 - \left(\frac{v}{c}(f_C + f_{AZ}) + \frac{c f_{AZ}}{2v}\right)^2} - 2j\pi f_R \frac{f_{AZ}}{K_R}\right] \cdot \\ &\cdot \exp\left[-4j\pi (f_C + f_{AZ})\frac{R_c}{c} - 4j\pi f_R \frac{R_c}{c}\right] \end{aligned} \tag{3.21}$$

This operation is called bulk compression as only the targets at reference range are compressed properly, whereas targets at different range are less compressed the more they are distant from reference range.

Signal remapping by Stolt interpolation accounts for a refined compression that removes range-azimuth coupling and residual azimuth phase. Indeed, Stolt mapping provides a phase which is linear in range frequency thus making easier compression by inverse Fourier transform. Equation for Stolt mapping is

$$\sqrt{(f_C + f_{AZ})^2 - \left(\frac{v}{c}(f_C + f_{AZ}) + \frac{c f_{AZ}}{2v}\right)^2} \rightarrow f_C + f_{R1} \tag{3.22}$$

Final compressed image is hence achieved by a 2D Inverse Fourier Transform. It is worth noting that even though WDA is an optimum focusing algorithm [96], Stolt mapping could produce shading and multiple images in focused data [96].

Range-Doppler Algorithm

The range-Doppler algorithm (RDA) is a processing efficient algorithm for SAR focusing. One-dimensional operations are performed in range time and azimuth frequency domain and large difference in time scales of data in range and azimuth allows approximate separability of processing [103].

The RDA presented in this work is based on the modified FMCW version proposed in [26]. First step of this algorithm is range compression of beat signal s_B

$$S_B(f_R) = \exp(j2\pi f_C \tau)\,\mathrm{sinc}\left[\frac{\pi}{T}(f_B + f_D - f_R)\right] \tag{3.23}$$

where f_R is the range frequency, f_B represents the beat frequency and f_D denotes the Doppler frequency due to both the range migration of target and the continuous motion during signal transmission-reception.

Then Range Cell Migration Compensation (RCMC) is performed, *i.e.* removal of range migration and Doppler shift, in range-Doppler domain. A Fourier transform in the azimuth direction is performed and then range migration is

compensated by interpolation. Basically, as targets at same range but different azimuth are relocated to the same position in azimuth frequency domain, it is possible to correct a family of trajectories having the same closest approach range R_0 [103].

Finally, the output signal is multiplied by azimuth matched filter

$$H_{MF} = \exp\left[-j\frac{4\pi R_0}{\lambda}\sqrt{1-\left(\frac{\lambda f_{AZ}}{2v}\right)^2}\right] \tag{3.24}$$

and Inverse Fourier transform is performed in azimuth frequency direction to obtain the final compressed image.

It is worth noting that, despite being efficient because one RCMC operation corrects a whole set of targets, RCMC could be computationally expensive owing to interpolation [96].

Frequency Scaling Algorithm

Frequency Scaling Algorithm (FSA) usually focuses chirped radar data, e.g. conventional spotlight SAR data. However, it is possible using this algorithm to compress dechirped radar signals [104], as the FMCW beat signal. The FMCW version of FSA developed in [26] is presented hereby.

Fourier transform of beat signal s_B in azimuth direction is the first action to be performed. Resulting signal is

$$\begin{aligned} S\left(t, f_{AZ}\right) = &\exp\left[-j\frac{4\pi R_0}{\lambda}\sqrt{1-\left(\frac{\lambda f_{AZ}}{2v}\right)^2}\right]\exp\left[-j\frac{4\pi B R_0 t}{cT\sqrt{1-\left(\frac{\lambda f_{AZ}}{2v}\right)^2}}\right]\cdot \\ &\cdot\exp\left(j2\pi f_{AZ}t\right)\exp\left(j2\pi\frac{B}{T}t^2\right) \end{aligned} \tag{3.25}$$

Then, a scaling function and Doppler shift removal function

$$H_1\left(t, f_{AZ}\right) = \exp\left[-j2\pi f_{AZ}t + \pi\frac{B}{T}t^2\sqrt{1-\left(\frac{\lambda f_{AZ}}{2v}\right)^2}\right] \tag{3.26}$$

is multiplied by Equation (3.25). Residual Video Phase removal is achieved by Fourier transform in range direction followed by a multiplication by the function

$$H_2\left(f_R, f_{AZ}\right) = \exp\left[-j\pi \frac{\pi T f_R^2}{B\sqrt{1-\left(\frac{\lambda f_{AZ}}{2v}\right)^2}}\right] \tag{3.27}$$

and Inverse Fourier transform again in range direction.

Inverse frequency scaling is obtained multiplying by function

$$H_3\left(t, f_{AZ}\right) = \exp\left[-j\pi \frac{B}{T} t^2 \left(1-\left(\frac{\lambda f_{AZ}}{2v}\right)^2 - \sqrt{1-\left(\frac{\lambda f_{AZ}}{2v}\right)^2}\right)\right] \tag{3.28}$$

and final compression is achieved by successive Fourier transform in range direction, a multiplication by matched filter (3.24) and Inverse Fourier transform in azimuth direction.

3.4 Assessment of Three-Dimensional Mapping Capabilities

Nominal design parameters listed in Table 2.4) allow both acceptable values of SNR for the whole range of distances to be obtained and the start-stop approximation to be exploited. Concerning geometric resolution, a practically rectangular resolution element is achieved when a conventional side-looking monostatic SAR is considered. Specifically, this is possible because azimuth or along-track direction and range or across-track direction are orthogonal and sampling frequency and PRF are tuned correspondingly [105]. On the contrary, the proposed system is designed to look in general along directions not perpendicular to the motion of platform. As a result, image pixels cover no longer rectangular but differently skewed areas. Hence, in order to get satisfactory resolutions, it is of primary importance both to introduce a set of figures of merit to decide whether an image is acceptable or not and to evaluate system performance in control volume.

3.4.1 Geometric Model

Target position in three-dimensional space is determined by the intersection of three surfaces

$$R = \|\mathbf{P} - \mathbf{T}\| \tag{3.29a}$$

$$f_D = 2\frac{\mathbf{v} \cdot \mathbf{l}}{\lambda} \tag{3.29b}$$

$$\varphi = \frac{2\pi}{\lambda}(R_2 - R_1) \tag{3.29c}$$

namely range sphere, Doppler cone and phase hyperboloid [23].

Given a Cartesian coordinate system, whose origin is in the vertex O and axes along the edges of parallelepiped OD, OA and OC in Figure 3.3, $\mathbf{P}$ and $\mathbf{T}$ represent antenna and target position in Equations (3.29) whereas $\mathbf{l}$ represents the line of sight vector. It is worth noting that, if plane wave approximation is valid [23], phase hyperboloid (3.29c) degenerate in a cone.

Range Sphere - Doppler Cone Intersection

Gradient method can be exploited to assess the effects of pixel shape in presence of squint angle within the whole three-dimensional environment. The application of the gradient method requires the introduction of more general definitions of range and Doppler or azimuth directions as the direction of fast time gradient $\overrightarrow{\nabla t}$) and Doppler frequency gradient $\overrightarrow{\nabla f_D}$, respectively [106]. In addition, a further hypothesis of motion at constant velocity within the integration time is assumed. It is worth noting that the gradient method, traditionally applied considering terrain, can be extended to each wall in case of indoor navigation to get a three-dimensional awareness.

Characteristics of range and Doppler isolines, caused by intersection of both range sphere and Doppler cone with walls, are analyzed herein. In detail, the

unambiguous area is defined in the plane of each wall as the geometric locus which simultaneously satisfies the following three criteria:

- the angle Ω of intersection between iso-range and iso-Doppler contour lines falls within the interval $[\Omega_{\min}, \Omega_{\max}]$,
- the spatial resolutions computed along range and Doppler directions are not lower than required in Table 1.2,
- the area of an illuminated pixel (*i.e.*, the area bounded two adjacent iso-range and iso-Doppler lines) is smaller than a threshold A_{pixel} related to required cell resolution.

Consequently, the ambiguous area is the complement of the unambiguous one. Aforementioned criteria physically mean that within the ambiguous area the shape of resolution cell does not allow target position on the wall plane to be established with desired accuracy, owing to the size of resolution cell and geometry of both isolines and pixel. Furthermore, it is worth noting that a phase value can be assigned to a point observable in both range and Doppler domain, that is a point which lies in unambiguous area, thus making possible interferometry.

Layover

Layover is a well-known geometric distortion of SAR images affecting targets which have the same range and velocity relative to platform in three-dimensional space [72, 105]. Layover does not affect the capability to image an area of interest but can cause the inversion of the position of scatterers and geometric distortion, resulting in interpretation problems. With reference to the considered control volume, the most critical zones interested by layover are edges and angles generated by the intersection of two or three walls, which have at least two layovered points [105]. However, this is not a specific problem of the proposed

system since it affects any radar observation and SAR data processing algorithms do not typically remove layover areas. In addition, the exploitation of multi-aspect InSAR data has demonstrated good capabilities in terms of recognition and removal of layovered areas [107]. Even though these techniques have been tested on different scenarios, *i.e.*, layover generated by small and large buildings in urban areas, they are expected to be useful for the proposed system. Indeed, since it is expected that required multi-aspect interferometric acquisitions will constitute system operating mode in order to increase the percentage of covered area within the control volume (see Section 3.4.1), proposed and successfully experienced techniques to cope with layover will be certainly exploited.

3.5 Results

Point Target analysis

The first operative condition handles a point target on a completely absorbing background observed in side-looking geometry. No windowing functions are applied for sidelobes level reduction. The results in range and azimuth directions are listed in Table 3.3. and sorted by time required to complete the focusing procedure. All simulations are performed by an Intel Core i7-4790 processor working at 3.60 GHz. Therefore, the time values should be related only to that kind of processor. Nonetheless, comparisons among the different processing times represent an indication of the computational load each algorithm involves. The fastest algorithm is the RDA, whereas the BPA needs a time that is 2 orders of magnitude longer. In range direction all algorithms show similar performance, namely Impulse Response Width (IRW) approximately equal to 0.88 range bins with a variation of less than 10% around this value, Peak Side Lobe Ratio (PSLR) lower than -13 dB with a difference of 0.26 dB between the maximum and the minimum values, and Integrated Side Lobe Ratio (ISRL) slightly lower

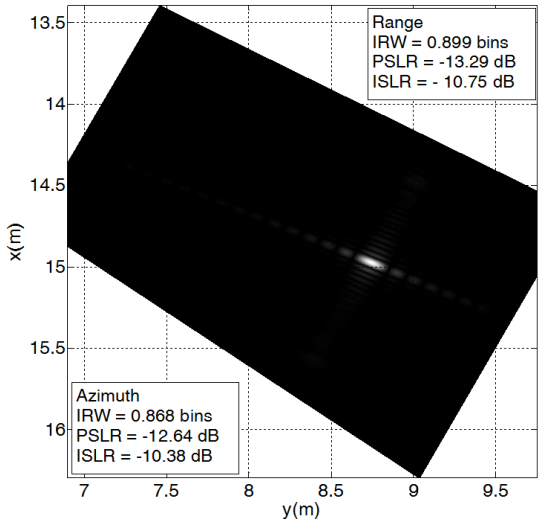

Figure 3.9: Point Target Response for a 30° squint angle straight trajectory: BPA

than -10 dB. All the results are predictable [75]. In azimuth direction, instead, some differences between algorithms appear: the PSLR ranges from -12.59 dB to -11.50 dB but is always slightly greater than -13 dB; a difference of 2 dB is present between the best and worst computed ISLR. Windowing function should be therefore considered in future applications. The second operative condition arises from the consideration that envisaged operations could require unusual observation geometry with high-squint angle and not necessarily straight trajectories. However, for sake of simplicity, a straight trajectory with 30° squint angle has been tested. BPA yields again a bi-dimensional sinc with required resolution centered at target position whereas the frequency-based algorithms fail in both resolution and positioning. The magnitude of PTR for BPA and RDA is depicted in Figure 3.9. Even though BPA still does not allow real-time focusing, it is able to fit different uncommon scenarios.

The dimensions of control volume adopted in present work are listed in Table 3.1. A point target at position $\mathbf{T}_P = [15.0, 8.0, 0.0]\,(\mathrm{m})$ is imaged, with the platform initially located at $\mathbf{P}_0 = [14.8, 1.4, 4.5]\,(\mathrm{m})$. The platform is observing scene in side-looking mode and moves at constant speed $\mathbf{v} = [0.5, 0.0, 0.0]\,(\mathrm{m})$.

Table 3.3: Point Target Response for a side-looking observation

	Time (s)	IRW (bins)		PSLR (dB)		ISLR (dB)	
		Range	Azimuth	Range	Azimuth	Range	Azimuth
BPA	48.85	0.881	0.882	-13.36	-12.57	-10.16	-9.91
WDA	1.35	0.898	0.882	-13.19	-12.59	-10.06	-9.92
RDA	0.45	0.884	0.868	-13.10	-12.27	-10.07	-10.90
FSA	0.71	0.896	0.920	-12.57	-11.50	-10.18	-9.01

Each cell contains at least 9 point targets representing background. For the sake of simplicity, a unit radar cross section σ has been selected for the point target, whereas two different mean radar cross sections have been selected for background, respectively 10dB and 20dB smaller than point target RCS. Histograms showing occurrences of amplitude values for a single pulse are depicted in Figure 3.10a and Figure 3.10a and the phase is shown in Figure 3.10a.

Table 3.4 and Table 3.5 list the focusing results of the four implemented algorithms for a background having -20 dB and -10 dB intensity, respectively. Performance in terms IRW, PSLR, and ISLR is shown for each algorithm. Specifically, the first and the second row refer to the performance in range and azimuth direction, respectively. Results show that, in the considered scenario, fluctuations do not affect IRW. In addition, a -20 dB background gives results similar to the ones for completely absorbing background (see Table 3.3). This result suggests that further simulations can be carried out considering point targets only. On the contrary, a background with stronger intensity raises sidelobes' level and energy of about 3 dB. This can be seen also in Figure 3.11 and Figure 3.12 where BPA results are depicted: depending on the actual realization of the statistical distributions, cases exist in which some peak lobes can be even higher than -10 dB.

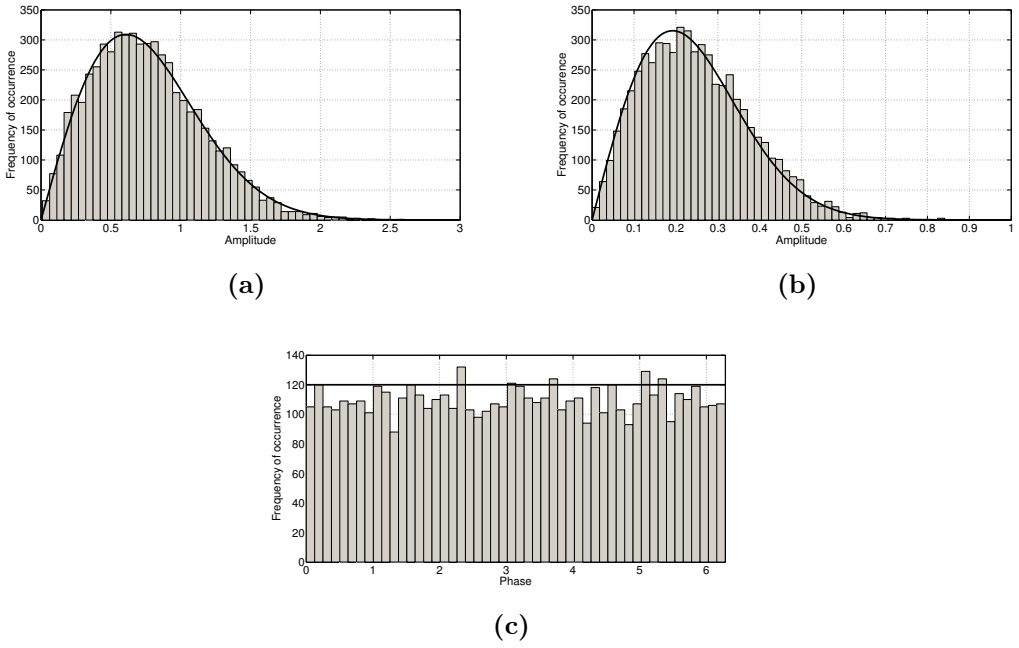

Figure 3.10: Fluctuating target: examples of amplitude and phase distribution.

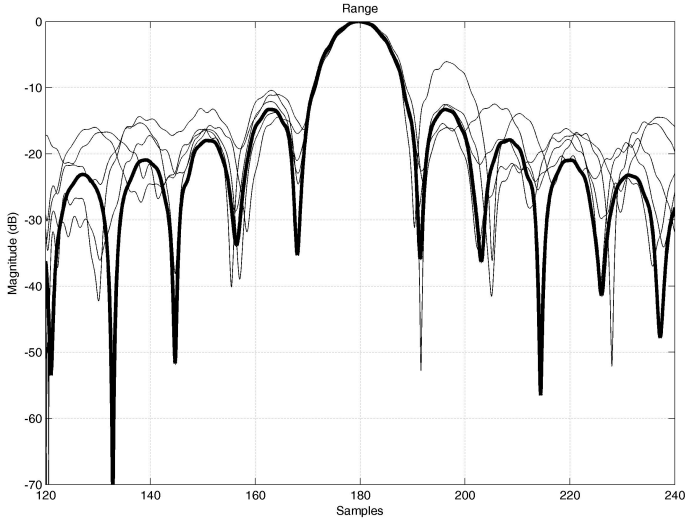

Figure 3.11: BPA -10 dB range. 5 realizations. Nominal condition, i.e. point target on absorbing background, in thick black line.

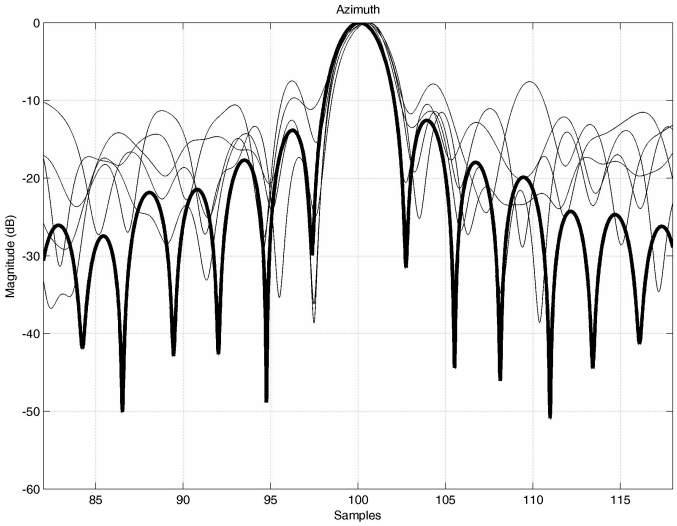

Figure 3.12: BPA -10 dB azimuth. 5 realizations. Nominal condition, i.e. point target on absorbing background, in thick black line.

Table 3.4: Fluctuating target: Point Target on -20dB background

	IRW (bins)		PSLR (dB)		ISLR (dB)	
	Mean	Variance	Mean	Variance	Mean	Variance
BPA	0.865	0.006	-13.192	0.269	-10.686	0.134
	0.823	0.003	-12.682	0.298	-9.695	1.054
WDA	0.887	0.004	-13.1026	0.244	-10.217	0.134
	0.809	0.003	-12.670	0.272	-10.258	0.141
RDA	0.883	0.004	-13.145	0.248	-10.335	0.132
	0.799	0.003	-12.632	0.270	-10.037	0.341
FSA	0.887	0.011	-12.925	0.216	-10.571	0.153
	0.841	0.005	-11.615	0.2336	-9.600	1.035

Table 3.5: Fluctuating target: Point Target on -10dB background

	IRW (bins)		PSLR (dB)		ISLR (dB)	
	Mean	Variance	Mean	Variance	Mean	Variance
BPA	0.859	0.081	-10.195	1.850	-6.636	1.309
	0.832	0.020	-9.905	1.312	-3.625	3.356
WDA	0.874	0.038	-10.104	1.839	-5.604	1.268
	0.807	0.033	-10.414	1.356	-5.818	1.287
RDA	0.878	0.053	-10.284	1.887	-5.924	1.213
	0.809	0.020	-10.5896	1.264	-4.982	1.551
FSA	0.873	0.112	-9.691	1.952	-6.125	1.338
	0.809	0.043	-7.068	3.105	-5.395	1.533

3.5.1 Focusing

Point Target Response Analysis has been treated in [77, 108], showing that BPA requires about 50 times the time needed by frequency domain algorithms. It is therefore useful to show some relevant results of focusing techniques. The first case handles two targets observed in side-looking geometry lying in the same plane (see Figure 3.13) which is the reference plane for BPA: both targets are imaged in the right position. Frequency domain algorithms are independent from reference plane and image targets in range-azimuth plane.

The second case deals with two targets at different height (see Figure 3.14): BPA places the first one in the right position, whereas the second in the reference plane at different y-coordinate.

It is possible to predict position in the image of an illuminated target which is not in the reference plane. For sake of simplicity, let us assume that the antenna moves along a straight trajectory parallel to x axis at costant height and that x-coordinate of the target in the image is equal to x-coordinate in

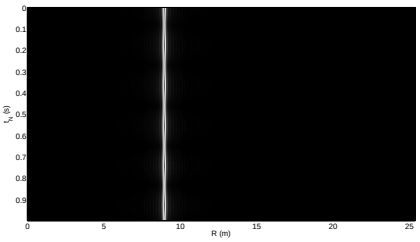

Range-slow time signature.

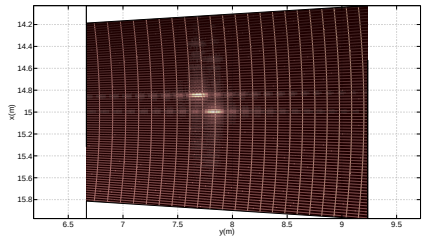

2D Focused signal. Isolines are depicted, too.

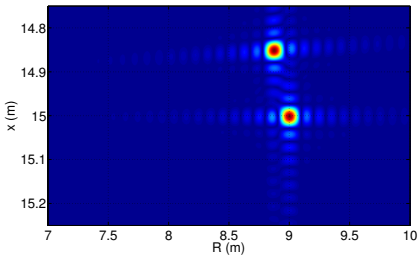

WDA

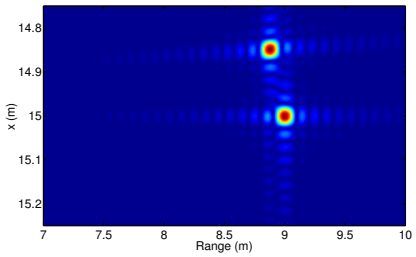

RDA

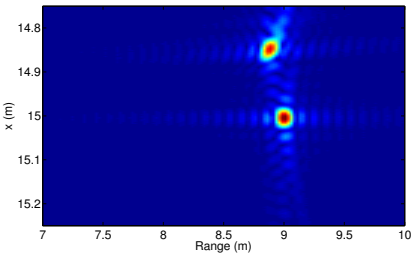

FSA

Figure 3.13: *Target 1*: $\mathbf{P_1} = [15.00, 7.79, 0.00]\,(\mathrm{m})$; *Target 2*: $\mathbf{P_2} = [14.85, 7.65, 0.00]\,(\mathrm{m})$

the plane. Therefore, as the position in the image depends on the minimum approach range, it follows that

$$y_{\mathrm{image}} = y_{\mathrm{ant}} + \sqrt{(z_{\mathrm{ant}} - z_{\mathrm{target}})^2 + (y_{\mathrm{ant}} - y_{\mathrm{target}})^2 - (z_{\mathrm{ant}} - z_{\mathrm{ref}})^2} \qquad (3.30)$$

Figure 3.15 shows that for WDA range position is shifted depending on the height of antennas but there is no error in positioning.

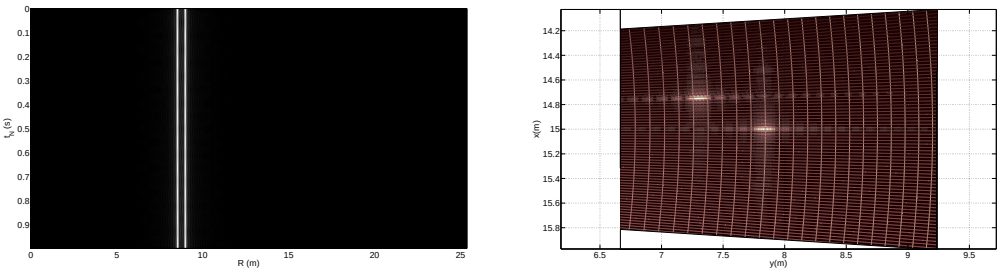

Range-slow time signature. BPA

Figure 3.14: *Target 1*: $\mathbf{P_1} = [15.00, 7.79, 0.00]\,(\mathrm{m})$; *Target 2*: $\mathbf{P_2} = [14.75, 7.55, 0.50]\,(\mathrm{m})$

It is clear that even in simplified geometry in BPA it is not possible to obtain true position from a single image, as it would mean to solve one equation - (3.30) - in two unknowns.

Moreover, an image with a target moving at a velocity $\mathbf{v_2} = [1.00, 0.37, -0.10]$ $(\mathrm{m\,s^{-1}})$ (see Figure 3.16) is presented: the moving point target is defocused and smeared but is visible. Its position in the final image is at azimuth coordinate where closest approach range is achieved.

Finally, two sets of images for squint-looking observation are illustrated (see Figure 3.17). When medium squint angle is adopted, e.g. 15°, frequency domain algorithms are able to focus data properly. On the contrary, for high squint observations, e.g. 35°, target resolution gets worse.

3.5.2 Ray-Tracing

2D geometry

A proper set of parameters able to model the observed scene is necessary to implement both RT and double-lobe model properly. In more detail and as discussed in Section 3.2.2, the capability of a surface either to scatter or to absorb the incidence energy depends on several parameters, including surface

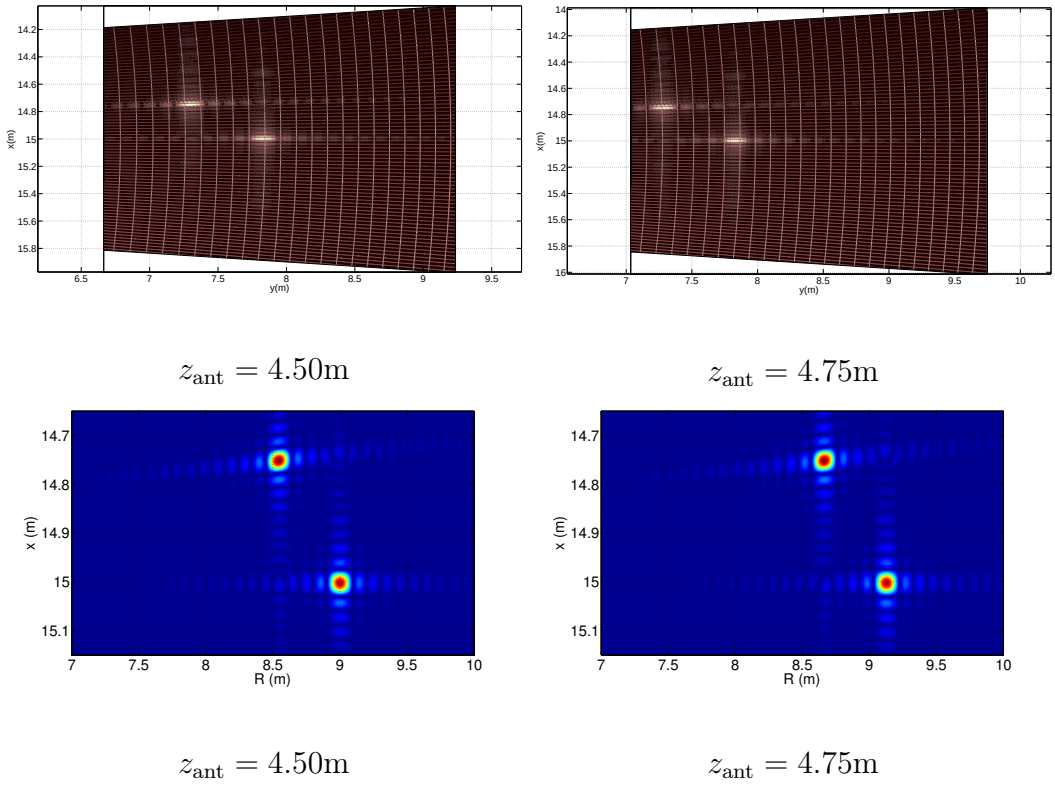

Figure 3.15: Example of images for different heights of antennas. *Target 1*: $\mathbf{P_1} = [15.00, 7.79, 0.00]\,(\text{m})$; *Target 2*: $\mathbf{P_2} = [14.75, 7.55, 0.50]\,(\text{m})$

roughness, material, signal wavelength and polarization. In the present example, transmission loss and reflection coefficient are set to -7.0dB and -7.5dB, respectively. These values are representative, in millimeter wave region, of walls made of concrete [86]. In addition, $\Lambda = 0.1$ is chosen by considering that, in general, backscattered energy is lower than the amount scattered along and around specular direction. This value leads to an energy level of backscattering returns coming from second and third hits at least 9 times lower than energy level from multiple reflections, thus making acceptable the approximation previously presented. Since nominal parameters have been found by assuming $\sigma^0 = -20\text{dB}$, that value has been kept even in the present section. Moreover, in order to analyze the effects of reflections, simulations are conducted with backscattering

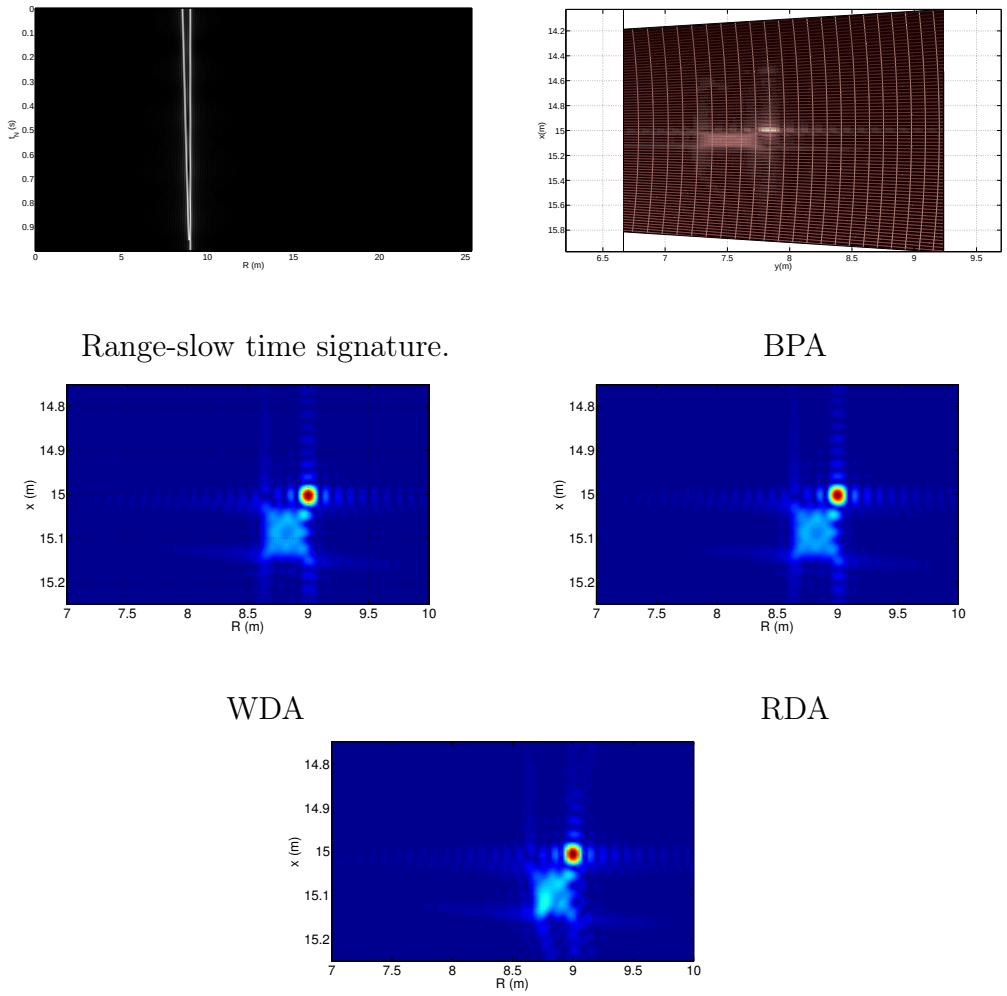

Figure 3.16: *Target 1*: $\mathbf{P_1} = [15.00, 7.79, 0.00]\,(\mathrm{m})$; *Target 2*: $\mathbf{P_2}\,(t_N = 0\mathrm{s}) = [14.75, 7.55, 0.50]\,(\mathrm{m}) - \mathbf{v_2} = [1.000, 0.373, -0.100]\,(\mathrm{m\,s^{-1}})$

effects only and backscattering plus reflections. In addition, it is worth highlighting that uniform wall has been modeled by locating several point targets on absorbing background in each cell, and the number of point target depends on the number of rays. Overall, 300 rays have been used in the two-dimensional simulation.

Two different cases are analyzed. The first case is depicted in Figure 3.19.

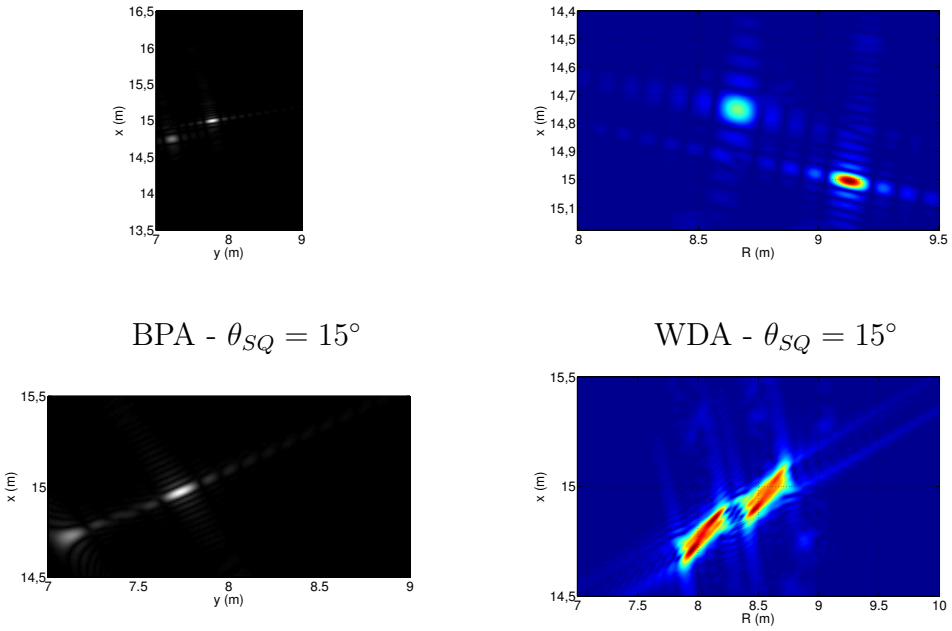

BPA - $\theta_{SQ} = 15°$ WDA - $\theta_{SQ} = 15°$

BPA - $\theta_{SQ} = 35°$ WDA - $\theta_{SQ} = 35°$

Figure 3.17: *Target 1*: $\mathbf{P_1} = [15.00, 7.79, 0.00]\,(\mathrm{m})$; *Target 2*: $\mathbf{P_2}\,(t_N = 0\mathrm{s}) = [14.75, 7.55, 0.50]\,(\mathrm{m})$

The antenna is at position $\mathbf{P}_0 = [8.8, 0.6]\,(\mathrm{m})$ and the off-nadir angle $\theta = 57°$ (see plots in Figure 3.19c and Figure 3.19d respectively). The reflected rays are not incident on the antenna, so that the difference in amplitude between backscattered echoes and complete echoes is zero (see plot in Figure 3.19b). The echoes coming from the scene (Figure 3.19a) show a higher peak shifted towards the boresight direction (indicated as Center Scene, CS) followed by a smaller one corresponding to Far Range (FR): this is mainly due to the accumulation of targets in the Near Range (NR). The second case considers the antenna located at $\mathbf{P}_0 = [8.0, 1.0]\,(\mathrm{m})$, that is farther from the wall than in previous case. The off-nadir angle is $\theta = 60°$ in this second case. The results are depicted in Figure 3.19. The reflected rays (Figure 3.19a) hit back the antenna and generate a small contribution (Figure 3.19b) in distribution of echoes. The variation of amplitude

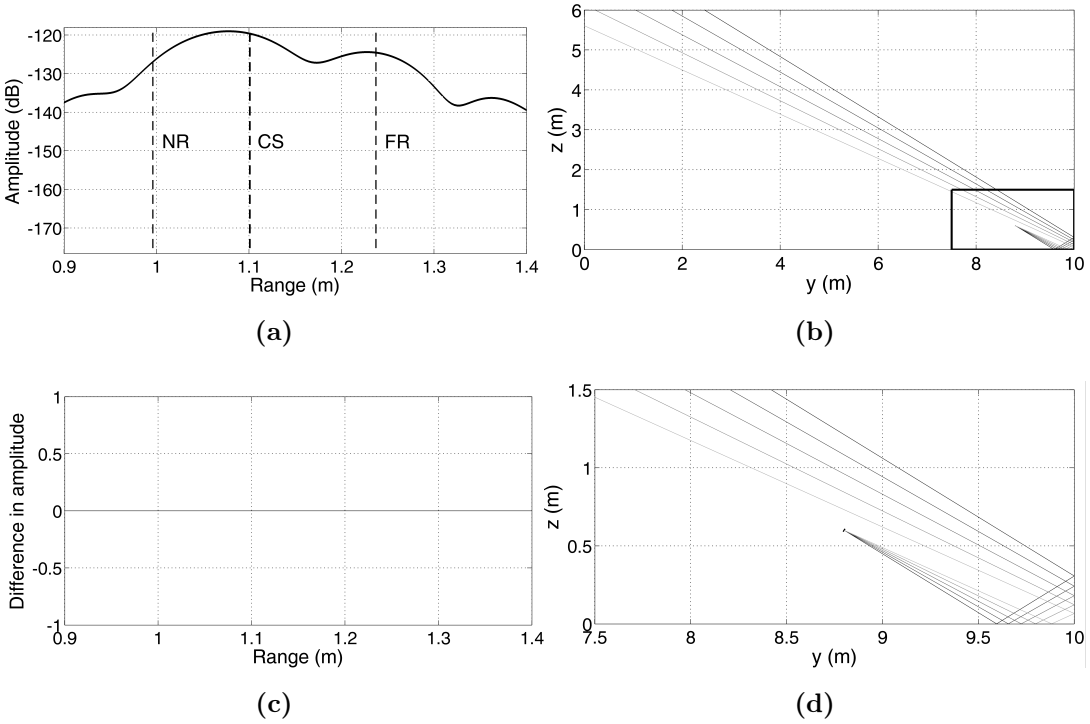

Figure 3.18: Case 1: observation of edge without reflections impinging on antenna. (a) radar echoes due to backscattering only, after FFT; (b) difference between radar echoes due to both reflections and backscattering and echoes due to backscattering, after FFT; (c) ray geometry, with magnified area highlighted in black; (d) magnification of ray geometry.

given by incoming reflected rays is about four orders of magnitude lower than amplitude due to backscattering. This result could be explained by observing that the parameter (3.12), which accounts for divergence of rays, is much smaller than unit. It is worth noting that the peak of reflected energy is in range bins corresponding to the area of backscattering returns. This could be expected as the geometry is the one of a corner reflector. Concerning the peak shifted towards FR, this is due to layover [105] and not to reflected rays. The results obtained by 2D analysis suggest that reflections from uniform surfaces do not affect the detection and recognition of typical indoor walls. This is in agreement with the experimental results presented in [91]. Specifically, ghost returns individuated in [91] are generated by multiple reflections and backscattering from the bright targets located outside the main beam of the antenna. With specific reference to an unknown environment, the main outcome of the 2D analysis is that a single data take from a single location is not adequate for a correct interpretation of the radar response. Multiple observations are mandatory for surfaces characterized by larger radar cross section or when extended target are present much brighter than the walls.

3D geometry

In this section the distances associated to minimum time delay, the maximum time delay and boresight observation are labeled as Near Range (NR_{3D}), Far Range (FR_{3D}), and Center Scene (CS_{3D}), respectively. Even though the terms are similar, these labels should not be confused with same terms usually used in remote sensing applications, and referred to the elevation plane of the antenna. The first example is illustrated in Figure 3.20 and represents a side-looking observation of the dihedral intersection edge between x-y and x-z planes, at such a distance that trihedral corner is not seen. The antennas are moving at a constant velocity $\mathbf{v} = [0.5, 0.0, 0.0] \left(\mathrm{m\,s^{-1}}\right)$ and initial position is $\mathbf{P}_0 =$

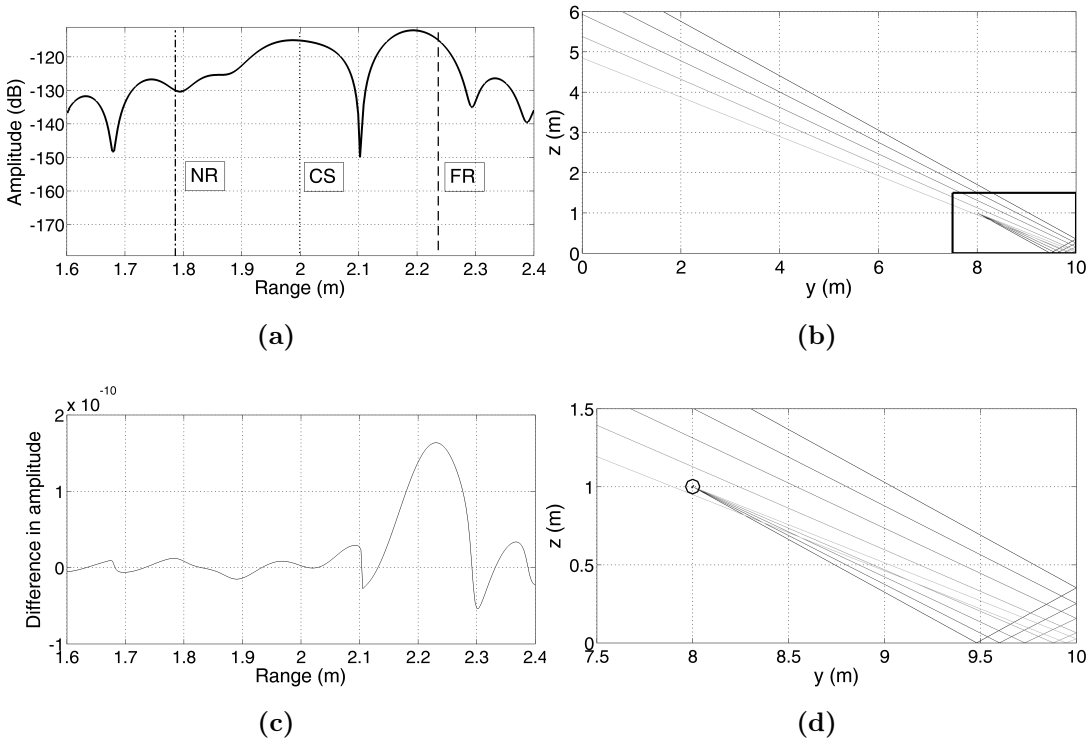

Figure 3.19: Case 2: observation of edge with reflected rays incident on antenna. (a) radar echoes due to backscattering only, after FFT; (b) difference between radar echoes due to both reflections and backscattering and echoes due to backscattering, after FFT; (c) ray geometry, with magnified area highlighted in black; (d) magnification of ray geometry and position of antenna (black circle).

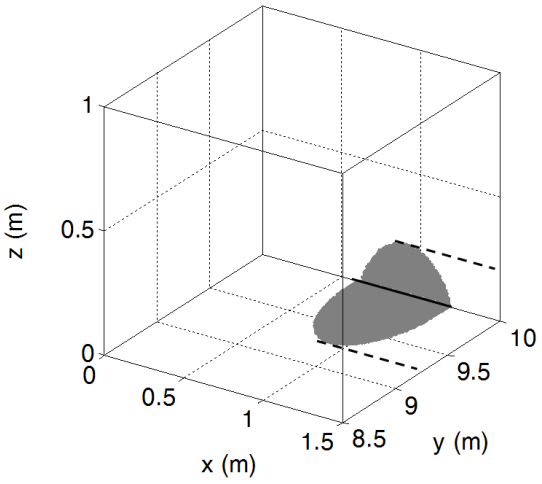

Figure 3.20: Dihedral corner observation. Illuminated area at a certain point and time during trajectory. Thick dotted lines indicates the illuminated areas during trajectory.

$[0.4, 8.0, 1.0]$ (m). The off-nadir angle is $\theta = 60°$. This is a particular geometrical case because only the rays emitted in the plane perpendicular to the motion and containing the line-of-sight vector $\mathbf{l}$ can be reflected towards the antenna. All the other diverging rays are reflected away. The focused image is shown in Figure 3.21. As expected, there is a slight change in the distribution of energy, due to presence of backscattered energy from azimuth directions behind and ahead the 2D observation plane along trajectory. The line of corner edge is not at the FR_{3D}, even though it is very close to it. Brightest peak is closest to the FR_{3D} owing to corner reflectors, layovered areas and lateral returns. It is worth noting that the capability to discriminate dihedral edges can be enhanced by the choice of millimeter wavelength, owing to typical high range resolution and smaller beamwidth. Indeed, even though layover cannot be removed, its effects can be reduced by illuminating a smaller area. In addition, better resolution reduces the spread of layovered areas in images.

In the second example, the antennas share the same motion, starting point and off-nadir angle with the previous case but a squint angle $\theta_{sq} = 15°$ is also

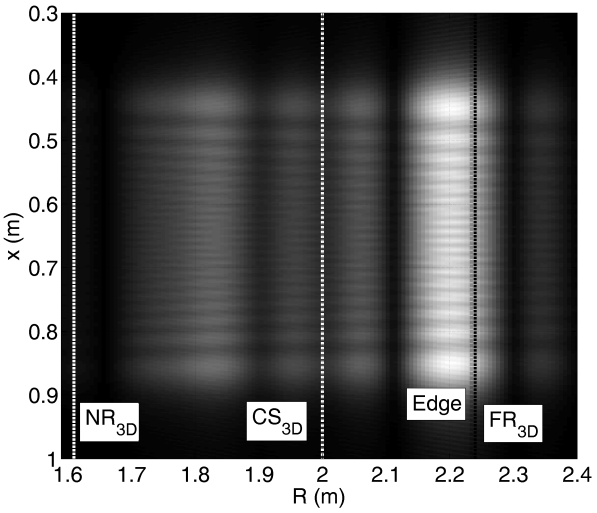

Figure 3.21: Focused image for dihedral corner observation.

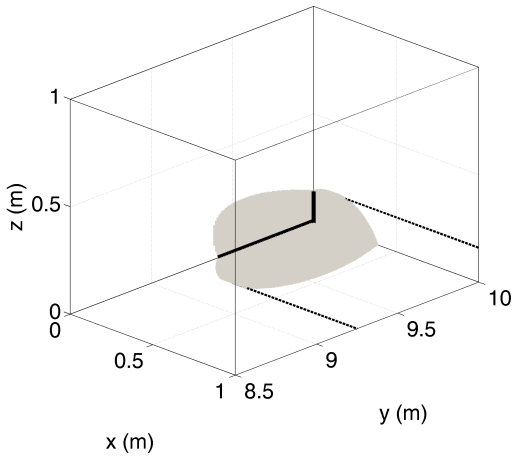

Figure 3.22: Trihedral corner observation. Thick black lines represent two additional edges seen during observation. Thick dotted lines indicates the illuminated areas during trajectory.

present. Therefore, trihedral corner, obtained by intersection of planes identified by x-y, x-z, and y-z directions, is illuminated, even though not at boresight, thus simulating a more general geometry (see Figure 3.22). Figure 3.23a shows the range compressed matrix: the bright signature in the first 30% of integration time is due to illumination of both intersection of three walls and points affected by layover. As the antennas move away from the trihedral corner, the range signature moves as well in bins associated to larger range. Then, in the remaining part of integration interval the signature of intersection of two walls is present. The final image, focused using the WDA algorithm, is shown in Figure 3.23b. The feature generated by the dihedral illumination can be easily recognized. Moreover, a brighter horizontal line appears within different range cells, owing to the trihedral corner and the intersection edges between both x-y and y-z planes and x-z and y-z planes. Therefore a trihedral corner reflector could be located by seeking the intersection of two orthogonal lines within the image. This is an example of information provided by the developed simulator which can be used to support the achievement of 3D awareness of the radiometric and geometric behaviors of the investigated radar sensor in indoor environment. Millimeter waves could be of benefit to reduce effects of layover even in presence of trihedral corners. The problem however remains and it is necessary a thorough interpretation of images.

3.5.3 Ambiguous Areas

Imaging performance is estimated considering the parameters listed in Table 3.6. The azimuth or Doppler resolution depends on the integration time or synthetic aperture duration. The integration time should be defined as the time span for which a given target is illuminated by the main lobe of the transmitting antenna and remains within the main lobe of the receiving one. For the considered system and environment the integration time is a function of the distance and of

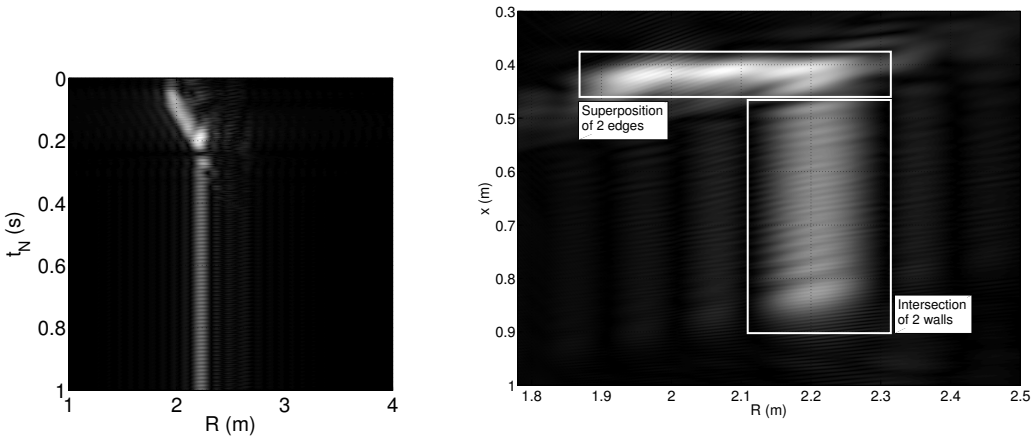

(a) **(b)**

Figure 3.23: Case 2: observation of edge with reflected rays incident on antenna. (a) radar echoes due to backscattering only, after FFT; (b) difference between radar echoes due to both reflections and backscattering and echoes due to backscattering, after FFT; (c) ray geometry, with magnified area highlighted in black; (d) magnification of ray geometry and position of antenna (black circle).

the relative geometry between the sensor and the target. Hence, it varies from point to point within the control volume. However, since this actual integration time is, in general, not known, the performance analysis is addressed in this section by supposing a constant integration time. This means that the integration time must be interpreted herein as the time span used for SAR focusing, which is assumed constant for all the imaged targets. The value for integration time reported in Table 3.6 is also compliant with possible platform dynamics and antenna apertures assumed in the simulation. As a consequence, it will exist a range of distances at which the theoretical azimuth resolution can be achieved. Farther points may suffer of worse resolution owing to increasing distance between either two close iso-range or iso-Doppler curves, which results in larger imaging pixel. Nonetheless, as shown in the following, the degraded pixel is still complaint with the minimum required resolution and pixel area threshold (Table 3.6) over sufficiently large areas within the test environment.

Table 3.6: Additional parameters for observation.

Symbol	**Parameter**	**Unit**	**Value**
T_{int}	Integration time	(s)	1
Ω_{min}	Lower bound on intersection angle	(°)	45
Ω_{max}	Upper bound on intersection angle	(°)	135
A_{pixel}	Pixel Area threshold	(m^2)	0.04
k_{res}	Minimum required resolution	(m)	0.20

Quantitatively, a preliminary analysis of mapping capability is carried out with the platform at a specific location. The antenna is located at position $\mathbf{P}$ with a velocity $\mathbf{v}$ (see Table 3.7) at half the integration time. Selected velocity and integration time give the theoretical azimuth resolution at a distance of about 3m (and synthetic aperture equal to 0.5 m), but acceptable values are

obtained even at longer distances as shown in Figures 3.24 and 3.25. In more detail, Figure 3.24 shows the three terms which contribute to ambiguous area (shaded) and the shape of resolution element within unambiguous area. The total unambiguous area is about 47% of total area and walls having observable areas are depicted in Figure 3.25. It should be noted that points lying within areas, whose size depends on distance (*i.e.*, the farther the wall, the larger the size), around the projection of velocity direction on walls are not observable owing to forward-looking ambiguities. In addition, points inside a circle, whose radius depends on distance, around projections of platform on walls are not observable owing to poor ground range resolution. Front and rear walls are not observable as the vector normal to their surfaces is parallel to velocity vector, thus resulting in parallel range and Doppler isolines. Furthermore, most of wall ABFE is not observable. It is worth noting that even though azimuth resolution satisfies requirements of Table 3.6, the effects of both ground range resolution and intersection angle Ω due to distance strongly affect the observation capability.

Table 3.7: Position and velocity of the antenna halfway through the integration time.

P_x (m)	P_y (m)	P_z (m)	v_x ($\mathrm{m\,s^{-1}}$)	v_y ($\mathrm{m\,s^{-1}}$)	v_z ($\mathrm{m\,s^{-1}}$)
15	2	2	0.5	0	0

Presented results suggest that the whole control volume can be mapped by exploiting platform agility to move and point the beam.

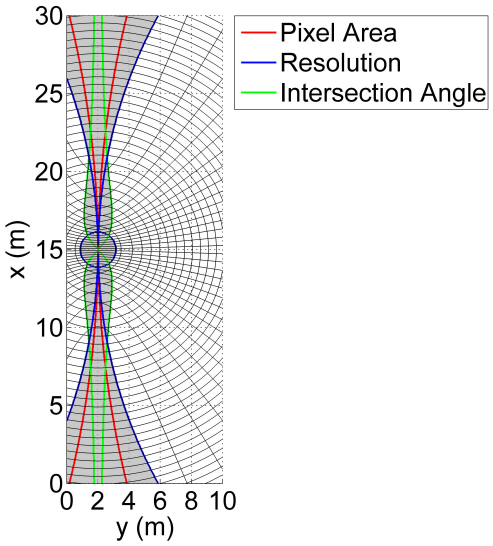

Figure 3.24: Plane OAED. Ambiguous area (shaded) and contributions: intersection angle (green contour), resolution (blue contour), and pixel size (red contour). For clarity, the distance between two close isolines does not represent true system resolution.

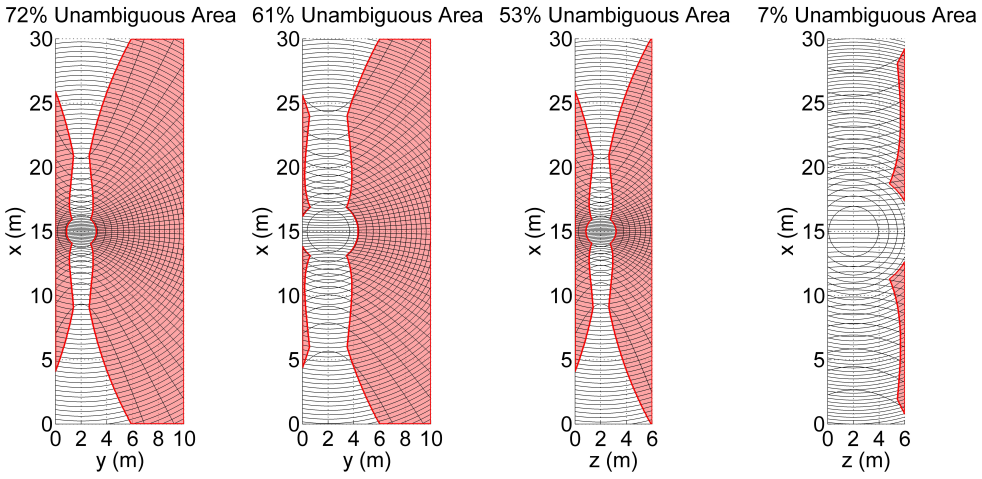

(a) Plane OAED **(b)** Plane CBFG **(c)** Plane OCGD **(d)** Plane ABFE

Figure 3.25: Total unambiguous area (in red, about 47% of control volume surface) for position and velocity reported in Table 3.7. Not observable walls are not depicted in figure.

Chapter 4

mm-wave SAR testing

Experimental campaigns with a 94 GHz SAR for high-resolution imaging under development at Fraunhofer Institute for High Frequency Physics and Radar Techniques FHR can be a valid support simultaneously to software simulator. High-resolution imaging at millimeter wave requires a very-high precision Inertial Measurement Units for the reconstruction of motion. Errors of phase larger $\frac{\lambda}{10}$ negatively affect focusing results [75, 109]. The assessment of imaging capabilities with commercial Inertial Measurement Units is one of the objective. In this Chapter the radar architecture is briefly illustrated, as well as candidate IMUs and results from preliminary campaigns.

4.1 94 GHz SAR

94 GHz radar developed at Fraunhofer FHR operates at wavelength $\lambda = 3.2$mm. The front-end guarantees phase coherent signal from pulse to pulse, enabling SAR processing. The clock frequency is $f_{\text{clock}} = 868.35$MHz. Transmission and reception of the electromagnetic signal is demanded to two integrated lens antenna (ILA) for 94 GHz center frequency [110], developed at Fraunhofer Institute IAF. The whole assembly of front-end and antennas is shown in Figure

4.1. Characteristics of antennas [110] are listed in Table 4.1.

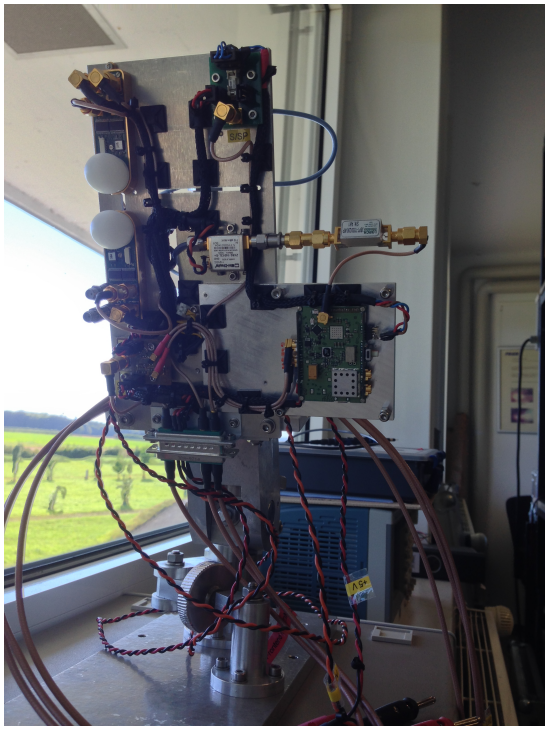

Figure 4.1: Assembly of FHR's 94 GHz SAR.

Table 4.1: Characteristics of integrated lens antenna (ILA) for 94 GHz center frequency.

Main Lobe in Azimuth Plane	9 °
Main Lobe in Elevation Plane	6 °
Antenna Gain	20 dBi

94 GHz front-end is able to operate both FMCW and Continuous Wave (CW). In CW mode it is also possible to measure micro-Doppler effects.

Currently, FMCW mode is set to generate SAR images for a platform flying at height $h = 50\text{m}$ with depression angle $\gamma = 30°$ (see Figure **??**.geo) and at maximum speed $v = 2.5\text{m}\,\text{s}^{-1}$. Therefore, the required pulse repetition frequency is $PRF = 500\text{Hz}$.

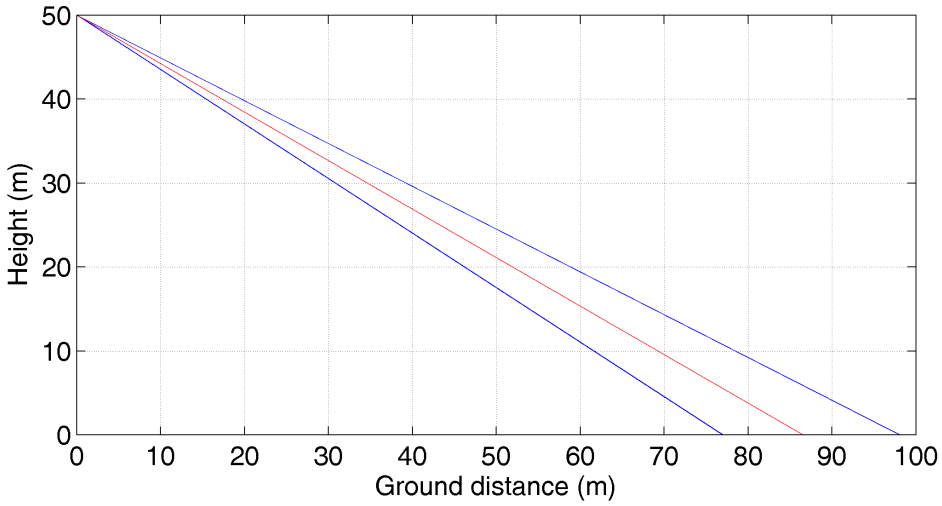

Figure 4.2: Envisaged flight geometry.

4.2 Inertial Measurement Units

Two different IMUs have been selected for imaging tests with 94 GHz, namely DJI A2 embedded IMU and XSens MTi-G-710 GNSS.

DJI A2 holds a position in the medium-high performance controllers segments and has five components: a Controller, a Power Management Unit (PMU), an IMU, a GPS-Compass Pro, and a LED. Since real-time motion compensation, direct access to IMU and GPS data is mandatory. The Controller unit of DJI A2 Flight Controller receives and elaborates data from GPS and IMU to stabilize the motion of platform and achieve a controlled flight. These data are typically sent to a ground station via a data-link and undergo two-step encryption. The first step, *i.e.* the one from Controller Unit to transmitter, is basically a XOR masking. On the contrary, the second step, *i.e.* from transmitter onboard

the platform to ground station, has a more complex and proprietary encryption system. Tackling the XOR masking represents a more convenient solution on different levels. Indeed, obtaining data directly on the platform could enable onboard motion compensation (MoCo) and makes the technique independent on transmission data link. In addition, XOR decoding is in theory simpler than decoding a proprietary encryption code.

A partial solution to decryption of DJI A2 XOR masking has been already provided in the drone community [111]. The schematics for decryption circuitry is depicted in Figure 4.3. A Teensy 3.1 board [112] has been connected to A2 CAN-bus through CAN-transceiver and power regulator. CAN transceiver reads High- and Low-Voltage outputs of CAN-bus and an Arduino-based code, supported by C-libraries, decodes the signals within the Teensy board. The datalink between Teensy board and the Processing Unit (PU), a Gigabyte BRIX, is Serial-to-USB. Furthermore, a Wi-Fi data-link enables communication between ground control station and the PU.

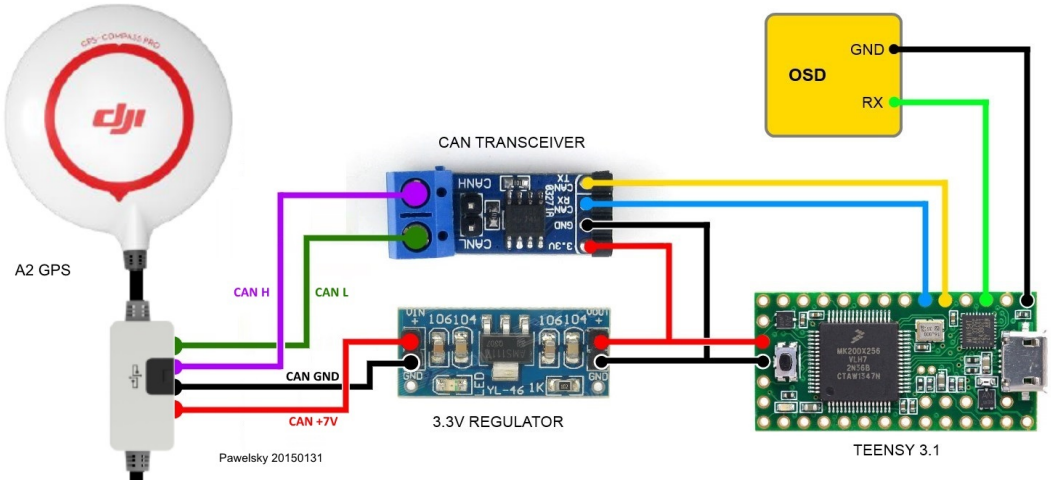

Figure 4.3: Schematics for decoding data from DJI A2 Controller.

However, not all the data required to perform MoCo are provided or require additional processing. First main issue is that roll and pitch angles are not

decoded. Hence, it is necessary to obtain an estimate from other data such as accelerations. It is of foremost importance the strapdown mounting geometry of IMU. That is, be $\{X, Y, Z\}$ the body reference frame, and be X and Z the axes that lie in the elevation plane of the radar in side-looking geometry, then the roll angle is computed as

$$\alpha_R = \text{atan2}\left(\frac{a_X}{-a_Z}\right) \tag{4.1}$$

and the pitch angle as

$$\alpha_P = \text{atan2}\left(\frac{a_Z}{\sqrt{a_X^2 + a_Z^2}}\right) \tag{4.2}$$

where a_X, a_Y, and a_Z are accelerations along the body axes. If X and Y are switched, then roll and pitch angles have to be corrected. Another problem is that GPS time has a constant offset due to a different reference time zone and is decoded as integer number, meaning that fractions of seconds are discarded. Direct consequence is that GPS signal can be received at any point within a second, thus hindering synchronization. Sub-second accuracy is therefore not feasible. This might not cause troubles if the GPS signal is stable and received each second. Finally, since they are data in output from A2 Control Unit they might be already filtered.

The A2 Controller transmits several packets (or messages). The interest is only towards three messages, whose identifiers (IDs) are '1002', '1003', and '4A44'. Message '1002' carries data from IMU and GPS time, message '1003' has data from GPS-Compass Pro, and message '4A44' reports the status of devices as well as battery level. The data are printed consecutively to serial monitor and therefore to file in ASCII format. Each message is divided in four lines. First line is the ID of message. Second line carries basic information for MoCo: GPS time, latitude, longitude, GPS height, course-over-ground angle, speed in North-East plane, vertical speed, roll angle, pitch angle, and heading angle. Third line is a

string to indicate auxiliary data. Finally, fourth line is given by the following: battery level, GPS time, number of satellites, GPS vertical speed, accelerations along body axes, height, GPS speed along North-direction, GPS speed along East-direction, and milliseconds since the beginning of acquisition code so to ease synchronization.

A more reliable and accurate solution is represented by XSens MTi-G-710 GNSS. Table 4.2 lists XSens MTi-G-710 GNSS performance [113]. Data can be retrieved directly and the user has full control on the downloaded data. For these experimental tests downloaded data are GPS time, latitude, longitude, GPS height, roll, pitch, yaw, velocities in North-East-Down frame.

Table 4.2: Performance of XSens MTi-G-710 GNSS

Gyro bias stability	Roll/Pitch Static | Dynamic	Yaw	Position / velocity
$10° \, h^{-1}$	0.2° | 0.3°	1.0 °	Yes

4.3 Results

Two experimental campaign with different IMUs have been performed. The results are reported in the following.

4.3.1 First campaign

First campaign has been carried out to test the effectiveness of A2-data and signal processing with respect to high-resolution SAR imaging. The radar, whose parameters are listed in Table 4.5, and the platform have been moved at nearly constant velocity on a rail. The length of rail is 18.4m and three corner reflectors (CRs) were in the scene (see Figure 4.4 and Table 4.3). R_0 represents the closest-

approach range and azimuth coordinate x_0 is computed from the right end of the rail. Test site is shown in Figure 4.5. Motion information is listed in Table 4.4. It is clear that for the selected wavelength even small variations of velocity cause errors in focusing. This is true even when dealing with actual UAV flight. Hence, the validity of results is not affected.

Figure 4.4: First campaign. Track and scenery.

The analysis of IMU data raised some problems. In detail, reconstruction of motion and attitude histories could be affected by drift and bias.

Concerning the motion history, the position of platform in NED reference frame has been computed by integrating velocities provided by IMU in the same reference frame. The error in positioning is evaluated by comparison with position retrieved by GPS data. Results are shown in Figure 4.6. The most evident behavior is an error in estimating the vertical motion of the platform. Indeed,

Table 4.3: Position of CRs during experimental campaign.

CR	R_0 (m)	x_0 (m)
1	≈ 11.5	≈ 6
2	≈ 17.5	≈ 10.5
3	≈ 11.5	≈ 7.5

Figure 4.5: View of test site. Red line represents the rail. Courtesy of Google Maps.

vertical motion is practically absent owing to the rail-based campaign, but IMU sees an excursion in height of several decimeters. GPS-based vertical position fits more with reality. In North-East plane the error of IMU data is larger,

Table 4.4: Acquisitions during experimental campaign.

Direction	CRs
Left ← Right	1-2-3

Table 4.5: Settings for the 94-GHz radar.

Number of samples in slow time	N_s	10000	
sampling frequency	f_S	17.43	MHz
Pulse Repetition Frequency	PRF	500	Hz
Pulse width	T	166.667	µs
Transmitted bandwidth	B	1	GHz
Carrier frequency	f_C	94	GHz
Sample Skip Factor	SSK	4	

whereas GPS shows a good accordance with trajectory depicted in Figure 4.5. It is worth noting, however, that stand-alone GPS-based position has an accuracy that depends on the number and position of satellites and it is possible that information on GPS position read by Teensy is already filtered with IMU information inside A2.

The second problem with the A2 IMU data regards the estimate of heading angle, which is provided by means of magnetic compass. When dealing with MoCo, heading angle errors have a very strong impact. Indeed, when transforming velocities from North-East-Down frame to body frame, if wrong heading angle is exploited the along-track velocity of the platform is understimated and focusing techniques become less effective. The visual outputs from Teensy data in Figure 4.7 show a behavior not fully compatible with the motion. Again, it

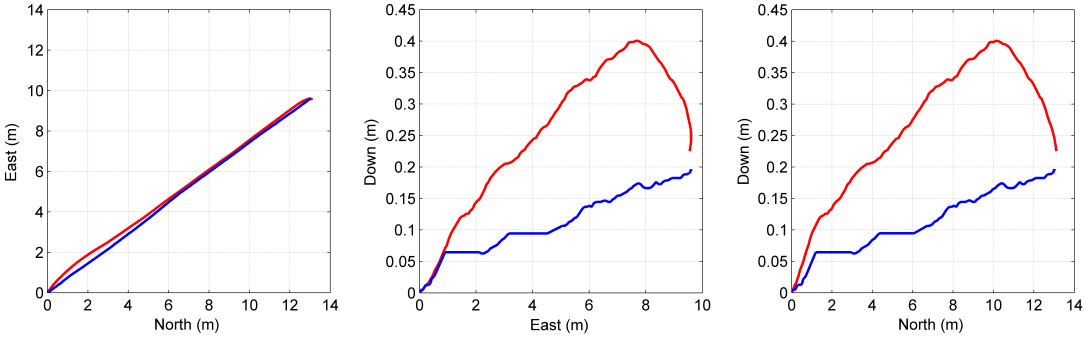

Figure 4.6: Projections of trajectory in North-East-Down reference frame. IMU data in red, GPS data in blue.

is possible that the output of A2 controller is an already filtered measurement.

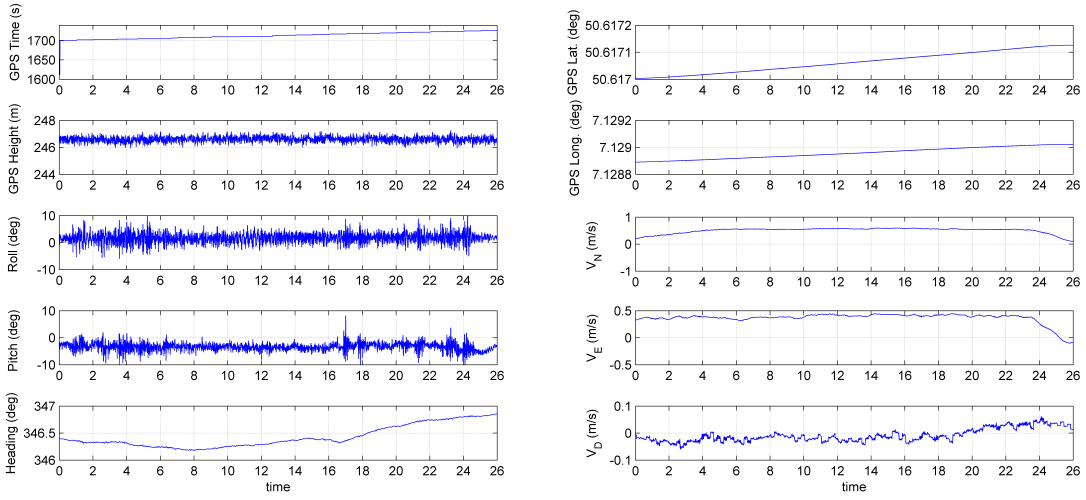

Figure 4.7: Visual outputs of data from Teensy.

Direct RDA focusing has been applied to radar data. The Single-Look Complex (SLC) image is shown in Figure 4.8. A detail of the two CRs separated in azimuth is in Figure 4.10, whereas the detail of single CR is in Figure 4.9. Since no accurate information on velocity is available the achievable resolution is coarser than theoretical and high sidelobes appear. A possible countermeasure to use this IMU is represented by autofocus algorithm.

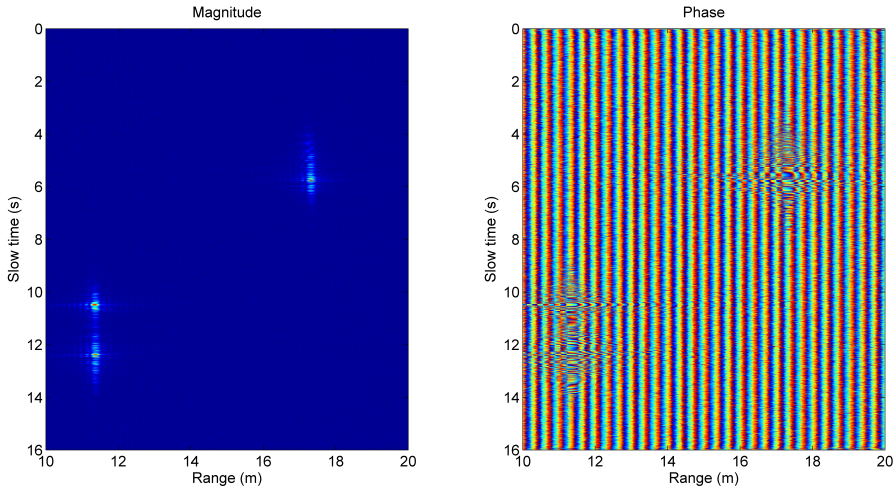

Figure 4.8: Full Scene RDA.

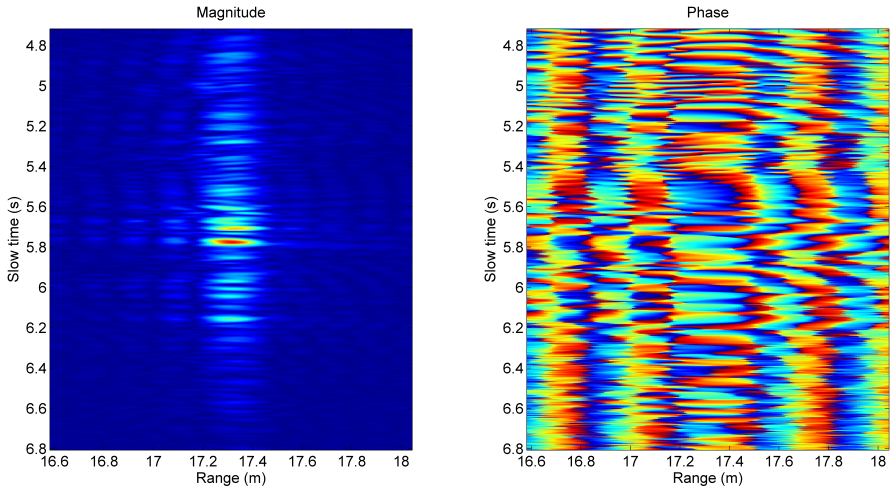

Figure 4.9: Single CR RDA Focusing.

4.3.2 Second Campaign

Second campaign has been carried out to test XSens data with signal processing for SAR imaging. The radar parameters are listed in Table 4.6. Both 94 GHz radar and XSens IMU are housed inside a van (see Figure 4.11). Test site is shown in Figure 4.12 and the illuminated scene inf Figure 4.13.

The analysis of the IMU data showed only one problem in the reading of

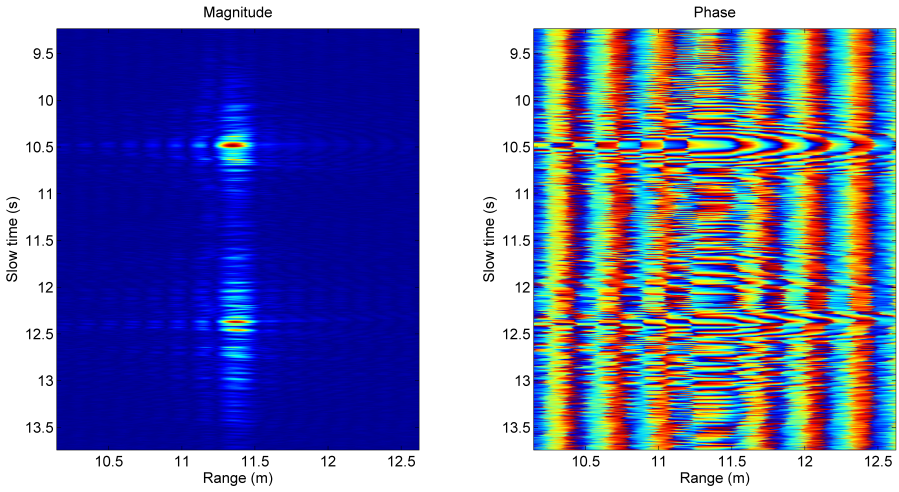

Figure 4.10: Two CRs RDA Focusing.

GPS time at certain second and minute. The bug is however fixed. Since more accurate motion data are available, the algorithm used for focusing image is Back Projection Algorithm. The Single-Look Complex image is shown in Figure 4.14. Comparison with the view of the scene in Figure 4.13 demonstrate that all targets are imaged, but even in this case an utofocus algorithm can improve final resolution.

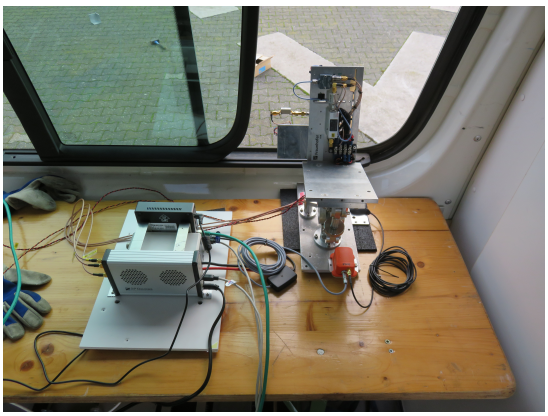

(a) Radar and XSens inside the van.

(b) Radar and van.

Figure 4.11: Second campaign.

Figure 4.12: View of test site. Red line represents the path of the van. Courtesy of Google Maps.

Table 4.6: Settings for the 94-GHz radar.

Number of samples in slow time	N_s	5000	
sampling frequency	f_S	69.72	MHz
Pulse Repetition Frequency	PRF	500	Hz
Pulse width	T	166.667	µs
Transmitted bandwidth	B	1	GHz
Carrier frequency	f_C	94	GHz
Sample Skip Factor	SSK	1	
Depression Angle	γ	20°	

(a) Scene: first part.

(b) Scene: second part.

Figure 4.13: View of the scene.

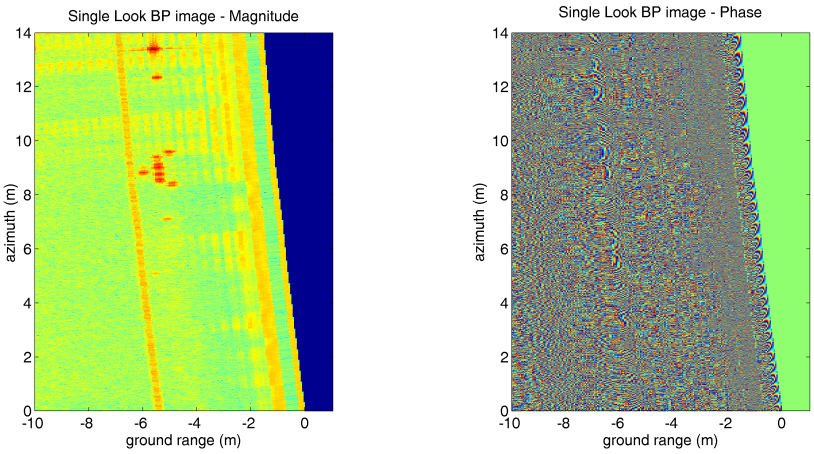

Figure 4.14: Full Scene BPA.

Chapter 5

Commercial ultralight radar sensor

Commercial ultralight radars have been recently developed [14, 15]. Their size, weight, and power fit requirements for housing onboard mini- and micro-UAS. It is therefore important to assess the performance in autonomous operation oriented scenario and evaluate the state-of-art advancement. In this Chapter an commercial very lightweight radar is presented and its performance in the framework of operations with mini- and micro-UAS are addressed.

5.1 24-GHz SENTIRE Radar

The FMCW radar 24-GHz SENTIRE Radar manufactured by IMST GmbH [14] has been selected for the present analysis. It is specifically tailored to mini- and micro-UAS operations as the radar front-end weighs 186g and its size is 133.7mm $\times$ 84.5mm $\times$ 35.6mm. It operates in K-band and its carrier frequency is 24 GHz, corresponding to a wavelength $\lambda = 1.25$cm. The set of antennas is developed by IMST GmbH. It consists of a single transmitting (Tx) and two receiving (Rx) patch antennas separated in azimuth direction. The whole as-

sembly of front-end and patch antennas is shown in Figure 5.1. Characteristics of antennas [114] are listed in Table 5.1.

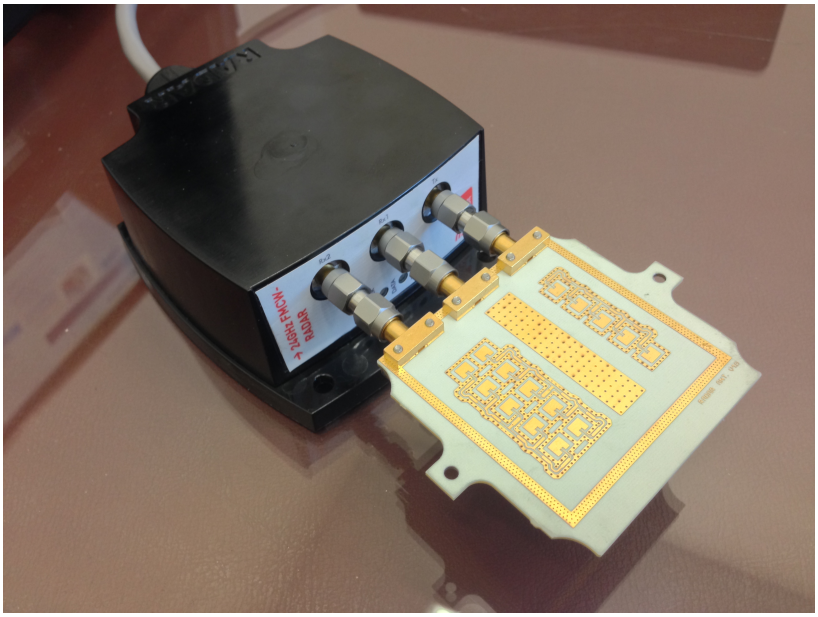

Figure 5.1: Assembly of SENTIRE Radar front-end and patch antennas.

The antennas allow for definition of reference frame of sensor: with reference to Figure 5.2, x axis represents the boresight direction, x-y plane is the azimuth plane, and x-z plane represents the elevation plane. The origin of this reference frame is in the phase center of transmitting antenna.

Working modes of SENTIRE Radar are both FMCW and Continuous Wave (CW). In FMCW mode it can measure range and, when both receiving antennas are active, bearing angle of a target, *i.e.*, it provides the position of targets in azimuth plane. Detection of targets' bearing angle θ_{bea} is possible thanks to azimuth separation between receiving antennas. Indeed, it enables phase interferometry [20]. The equation relating phase difference $\Delta\Phi_{\text{radar}}$ and the bearing angle θ_{bea} is

$$\theta_{\text{bea}} = \sin^{-1}\left(\frac{\lambda\Delta\Phi_{\text{radar}}}{2\pi L}\right) \tag{5.1}$$

where $\Delta\Phi_{\text{radar}}$ is the difference between phases Φ in the two receiving channels,

Table 5.1: Characteristics of Antennas

Tx Antenna	Main Lobe in Azimuth Plane	58 °
	Main Lobe in Elevation Plane	24 °
	Antenna Gain	9.6 dBi
Rx Antennas	Main Lobe in Azimuth Plane	70 °
	Main Lobe in Elevation Plane	24 °
	Antenna Gain	9.6 dBi
	Separation in Azimuth Direction	$\approx$ 7.1 mm

λ represents the wavelength and L is the distance between the two receivers. Since the separation between the two receiveing channels is $L \approx 7.1$mm, the unambiguous interval of bearing angle that can be measured with this technique, corresponding to the phase difference ranging from $-\pi$ to $+\pi$, is $\Delta\theta_{\text{bea},un} \approx 120°$ (see Figure 5.3). That is, $\pm 60°$ around boresight direction x. Nominal accuracy of distance and angular measurements are listed in Table 5.2 [14]. In addition, different frequency modulation are achievable. In CW mode, on the contrary, it is possible to measure Doppler content of the scene.

Table 5.2: Radar Performance: Nominal Accuracy

Distance accuracy	cm-range
Angular accuracy	$<$ 50 cm at 15 m

Finally, the radar connects and transmits data to control units, e.g. a laptop, via SPI-to-USB connection and requires FTDI D2XX libraries. Although it is tested and developed to work with units operating Windows environment, in this work the software has been also ported for GNU/Linux environment.

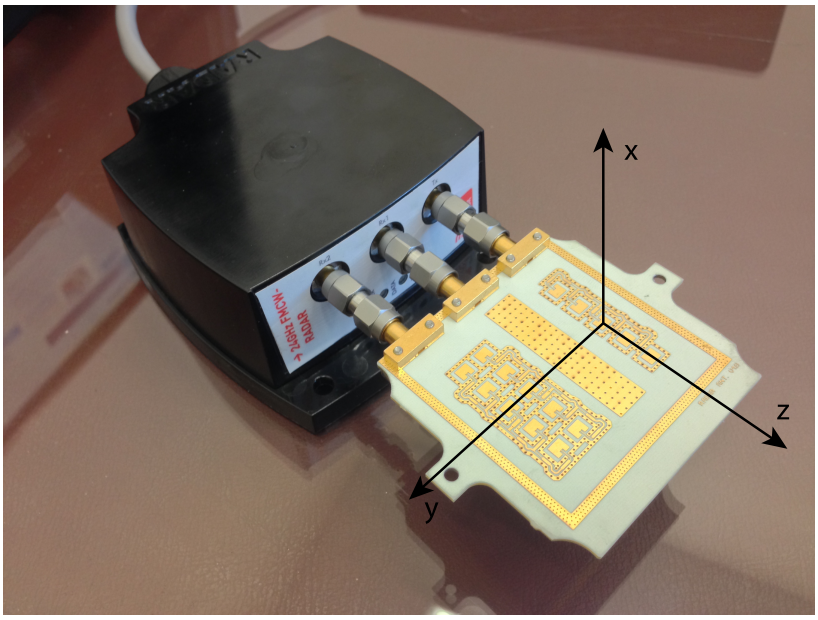

Figure 5.2: Reference frame for radar sensor.

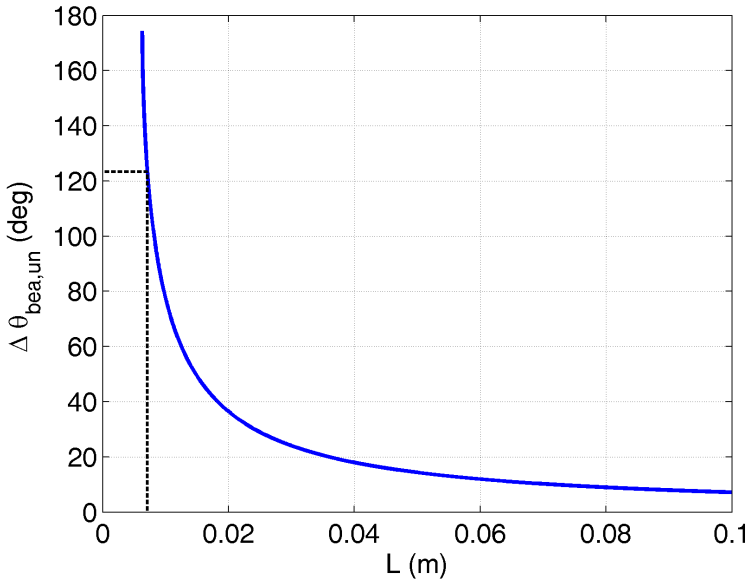

Figure 5.3: Unambiguous bearing angle interval as function of receivers separation L. In black, unambiguous bearing interval for SENTIRE Radar.

5.2 Characterization

Measurements with a single Corner Reflector (CR) on a uniform background have been collected first, in order to perform experimental characterization radar response. The reference frame hereafter exploited correspond to radar sensor reference frame. CR has been moved at different stations along azimuth direction y. Measured and true quantities have been listed in Table 5.3. Measured range, R, is compared to true range, R_e. Half-power Bandwidth (HB) range resolution is compared to expected range resolution. Finally, measured bearing $\theta_{\text{bea},_e}$ is compared to true bearing θ_{bea}. In general there is a satisfactory agreement between true and derived values of the considered parameters. As for the resolution, the results are in perfect accordance with theory regarding impulse response width. Also, sidelobes decay, not reported here, is about -13.8 dB, that is expected for a non-weighed antenna pattern [75]. Considering the limited interval of tested target range, the achieved results do not show a significant performance degradation as a function of distance and angle. It is worth noting that bearing measurement associated with detected range becomes less precise at larger azimuth angles, *i.e.* for azimuth values larger than half the beamwidth, as shown in Figs. 5.4-5.5. Additionally, the capability to discriminate two or more targets in terms of distance and bearing angle has been accounted for. Two still targets, one having high signal-to-clutter ratio (SCR) and the other having low SCR, at same azimuth coordinate and spaced in range of about 40 cm have been illuminated with a signal having $B = 1\text{GHz}$. Compressed echoes in Figure 5.6 indicate that the targets are correctly resolved. Figure 5.6 also shows an horizontal and almost flat trend for bearing angle at range locations where the two targets are. It is worth noting that the measurement of bearing angle is rapidly varying and not flat within areas that have returns from ground clutter. Based on this consideration, low-SCR targets could be identified and not confused with ground clutter. Signal noise can also be identified in near-range

Table 5.3: Results of radar measurements.

CR Position			Target Range		HB Range Resolution		Target Bearing	
x	y	z	R measured	R_e true	dr measured	dr_e true	θ_{bea} measured	$\theta_{\text{bea},e}$ true
(m)	(m)	(m)	(m)	(m)	(cm)	(cm)	(°)	(°)
4.50	0	-0.90	4.56	4.59	13.8	13.5	0.82	0
4.50	1.00	-0.90	4.69	4.70	13.6	13.5	-10.3	-12.3
4.50	2.00	-0.90	4.93	5.01	13.6	13.5	-29.2	-23.6
4.50	2.94	-0.90	5.35	5.45	13.7	13.5	-32.3	-32.6
4.50	5.00	-0.90	6.65	6.79	13.6	13.5	-38.3	-47.5

measurement, within two meters from radar.

5.3 Tests and Results

Different tests have been set up to assess the capability of radar sensor to cope with UAS-oriented operations. It is worth to mention that the whole set of raw data were calculated by computer from raw data and the highest frequency at which radar raw data were available is 9 Hz.

5.3.1 Sensing performance

Two tests have been conducted by illuminating both moving and still targets. The radar has not been housed onboard a MAV but placed in a fixed and stationary location. Radar parameters for these tests are listed in Table 5.4. In both tests,a DJI F450 quadrotor has been used for representing a moving target having not strong radar cross section (RCS) (see Figures 5.7 and 5.9). A trihedral 30-cm is the still target in first test. Stored range-compressed data from each frequency sweep have been arranged in a range-time matrix, *i.e.* a

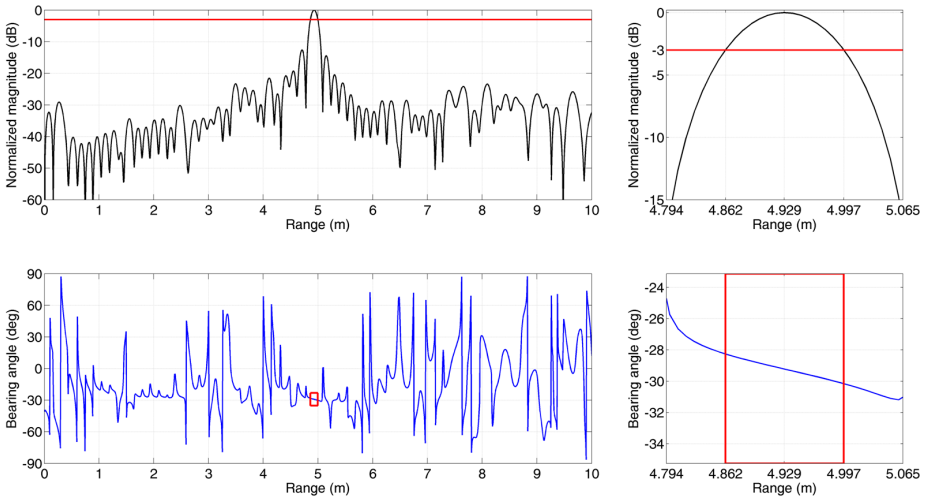

Figure 5.4: -3dB decay (top left - red line) and bearing angle (bottom left - red box) for CR at $y = 2.00$m. On the right: magnification.

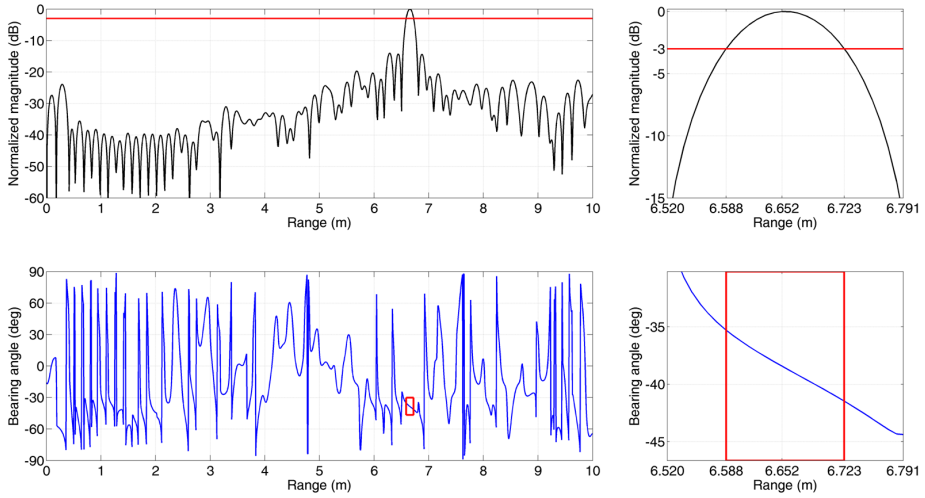

Figure 5.5: -3dB decay (top left - red line) and bearing angle (bottom left - red box) for CR at $y = 5.00$m. On the right: magnification.

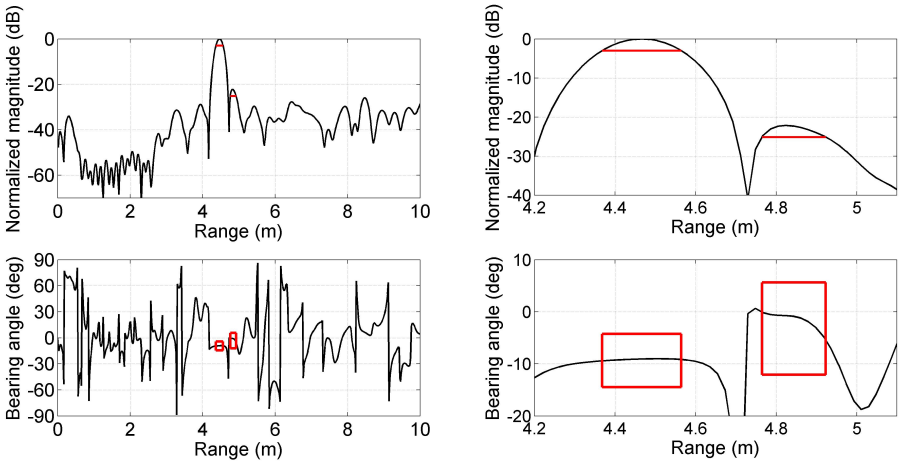

Figure 5.6: Identification of two close targets (red) in the scene. Normalized magnitude and bearing angle as function of range (left), magnification (right).

matrix whose horizontal axis is given by range and vertical axis is the acquisition time (see Figure 5.8). Both magnitudes and bearing angles are represented in Figure 5.8. The motion of quadrotor can be clearly identified. However, more in general, before being arranged in a matrix, range-compressed data for each frequency sweep can be analyzed in either real or near-real time to find range, bearing, and magnitude of targets in the scene. Ground clutter from background is present in compressed data. In addition, attitude of quadrotor affects its RCS, thus contributing together with distance to fluctuations in magnitude. Hence, epoch-wise identification of quadrotor could not be easy.

Table 5.4: Radar parameters during first campaign.

Transmitted Bandwidth	$B = 1\text{GHz}$
Frequency Modulation	Linear
Ramp Duration	$T = 1\text{ms}$
Sampling Frequency	$f_S = 208.3\text{kHz}$

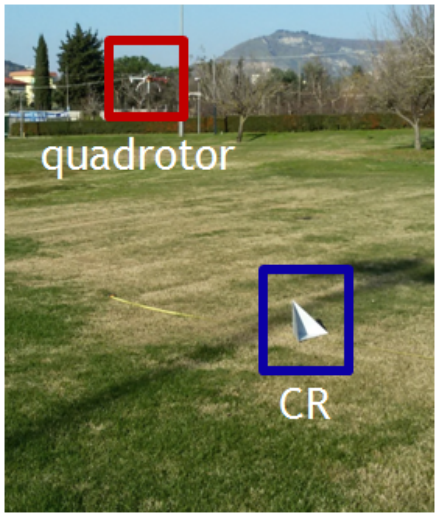

Figure 5.7: Range, magnitude and bearing angle for the three brightest targets at each acquisition time. The scene contains only flying quadrotor.

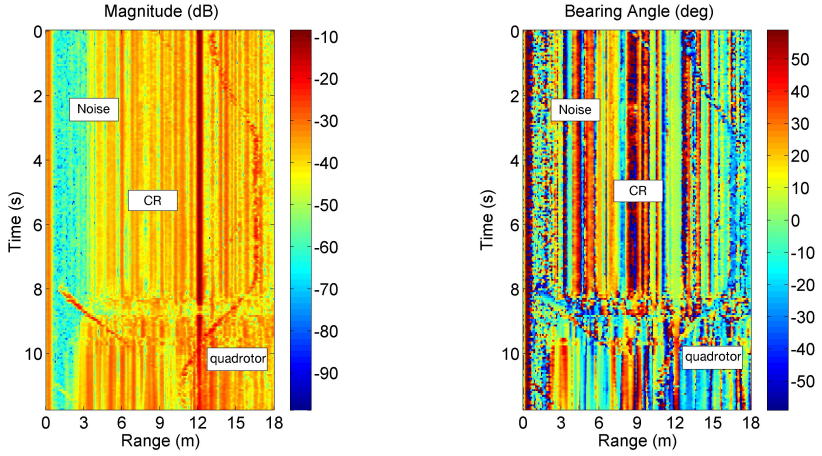

Figure 5.8: Magnitude (left) and bearing angle (right) as function of time and range for a scene containing a CR and a quadrotor.

Figure 5.9: Experimental setup with flying quadrotor.

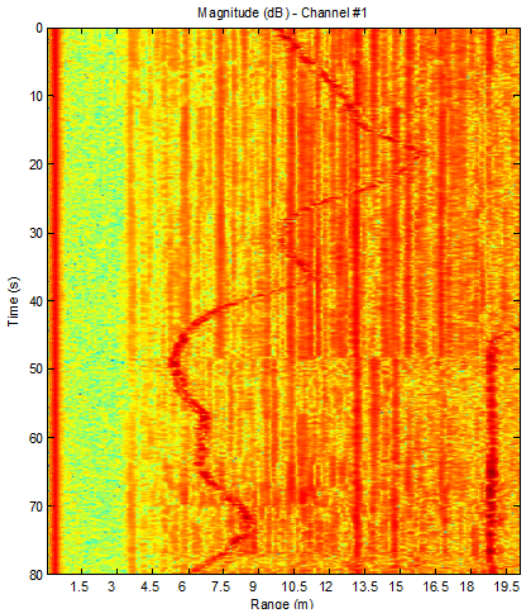

Figure 5.10: Magnitude of range compressed data showing the motion of quadrotor..

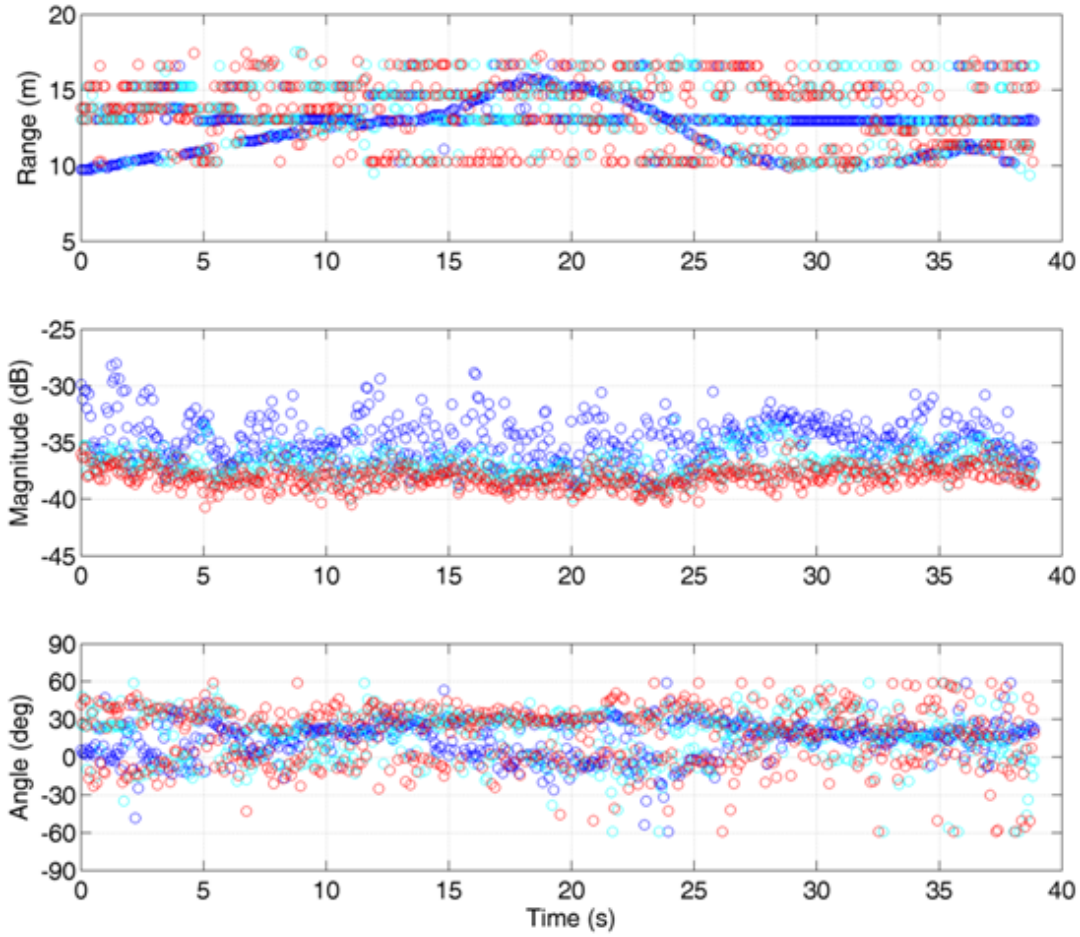

Figure 5.11: Range, magnitude and bearing angle for the three brightest targets at each acquisition time. The scene contains only flying quadrotor.

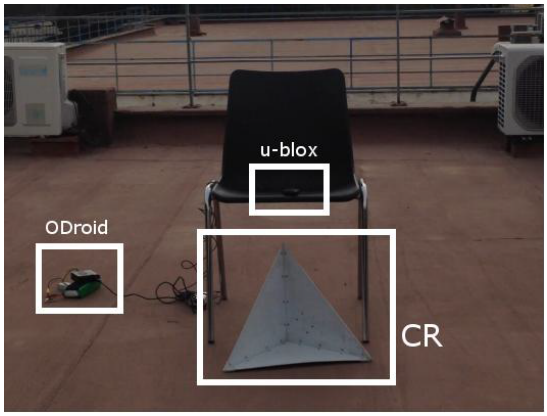

Figure 5.12: Magnitude and Bearing angle as function of time and range for a complex scene containing a CR and man-made objects. White and black boxes indicate phases of platform motion.

In the second test the still target is represented only by ground clutter as shown in Figure 5.9. Again, the motion of quadrotor is visible during a-posteriori analysis (see Figure 5.10), but real-time extraction of information is challenging. For sake of a better comprehension of the problem, range, magnitude, and bearing angle information of the three brightest targets for each scan, *i.e.* the ones whose magnitude is the highest, in the scene have been extracted from each row of range-compressed matrix. Figure 5.11 shows the whole set of extracted data sorted as function of time. Blue color is related to first brightest target, red color to second, and black color to third. Aforementioned fluctuations in peak magnitude of quadrotor can be easily noticed and combined analysis of range, angle and magnitude in necessary to track objects instead of clutter. It is worth noting that this analysis, which is based on fixed number of targets to be observed, is to ease the reader with the understanding of challenges related to radar tracking of MAVs. Indeed, the amount of targets to be potentially tracked depends on threshold on magnitude that has to be set to achieve an acceptable balance betwenn probability of false alarm and probability of detection.

Finally, radar sensor has been housed on moving platform and sensor motion

and more complex environment have been accounted for. CR and several strong man-made scatterers were observed. An u-blox GPS receiver have been housed onboard the platform and another u-blox GPS receiver has been placed above the CR and connected to an ODroid (see Figure 5.12), which ran an executable to acquire data. The GPS receivers were exploited in differential mode to provide information about the baseline between radar and CR [115]. New set of radar parameters has been selected (see Table 5.5), too. The total duration of test can be divided in five phases during which the CR was illuminated, each of them corresponding to different kind of motion. These phases can be seen in blue in Figure 5.13. During phases 1 and 2 back-and-forth motion along line-of-sight was achieved. Between first two phases the platform was rotated around radar z axis so to make the CR disappear from echoes. During phase 3 the range to the CR changed but the observation angle was kept almost constant by rotating the platform. In addition, around 180s from the start of acquisition, the platform rotated fast around z-axis clockwise and then counterclockwise, but the range was kept constant. Phase 4 accounts for straight motion along azimuth direction. Finally, during phase 5 both distance and observation angle changed. For this dataset, a Constant False Alarm Rate (CFAR) algorithm was exploited to extract information on the targets in the scene (see Figure 5.14). Radar track of CR has been extracted by means of offline tracking algorithm: it can be seen that CR and man-made objects exhibit a very similar range history, but different bearing angle. Furthermore, track of CR has been compared with baseline history provided by GPS receivers, showing that both radar and GPS measurements are in good accordance. This could be a valuable result for navigation purposes even in GPS-denied environments.

It is worth noting that the sampling frequency is different for the two experimental campaigns: this is partly due to the maximum range to be processed unambiguously. For instance, for calibration purposes and for the tests with

Table 5.5: Radar parameters and GPS data during second campaign.

Transmitted Bandwidth	$B = 1\text{GHz}$
Frequency Modulation	Linear
Ramp Duration	$T = 1\text{ms}$
Sampling Frequency	$f_S = 1401.7\text{kHz}$
Saved GPS Data	NAV-SOL - RXM-RAW

DJI F450 the maximum range to be observed was limited to $R_{\text{MAX}} = 30\text{m}$. On the contrary, test with moving platform had maximum range $R_{\text{MAX}} = 78\text{m}$. A different choice of ramp duration and transmitted bandwidth could have led to a maximum range $R_{\text{MAX}} = 300\text{m}$. These values of maximum range represent without doubts a further advantage with respect to close-range sensors, e.g. ultrasonic rangefinders [116].

5.3.2 Imaging

The data needed to perform azimuth focusing by synthetic aperture have been acquired while moving trihedral CR along a straight trajectory within the main beam in azimuth, *i.e.* the half-power beamwidth (see Figure 5.15). Range history for CR has been extracted from range-compressed matrix, thus deriving also radial velocity and Doppler frequency (see Figure 5.16). As expected, the Doppler frequency showed an almost linear dependence on time, which is desirable and encouraging for focusing purposes. However, the sampling frequency along azimuth direction, corresponding to the frequency at which raw data were available, was smaller than total Doppler bandwidth. Hence, focusing at nominal resolution has not been possible.

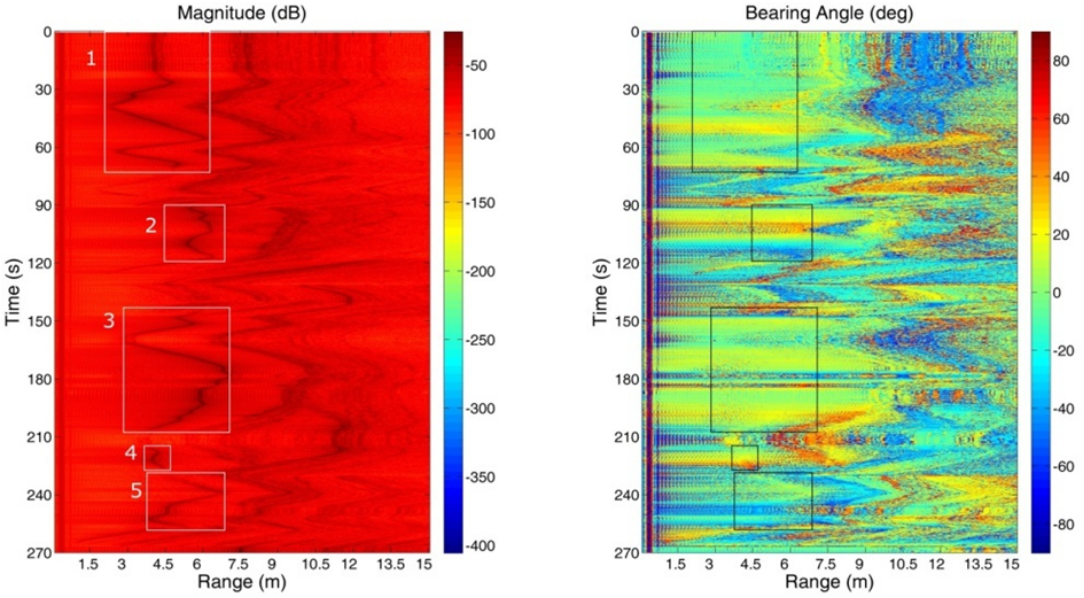

Figure 5.13: Magnitude and Bearing angle as function of time and range for a complex scene containing a CR and man-made objects. White and black boxes indicate phases of platform motion.

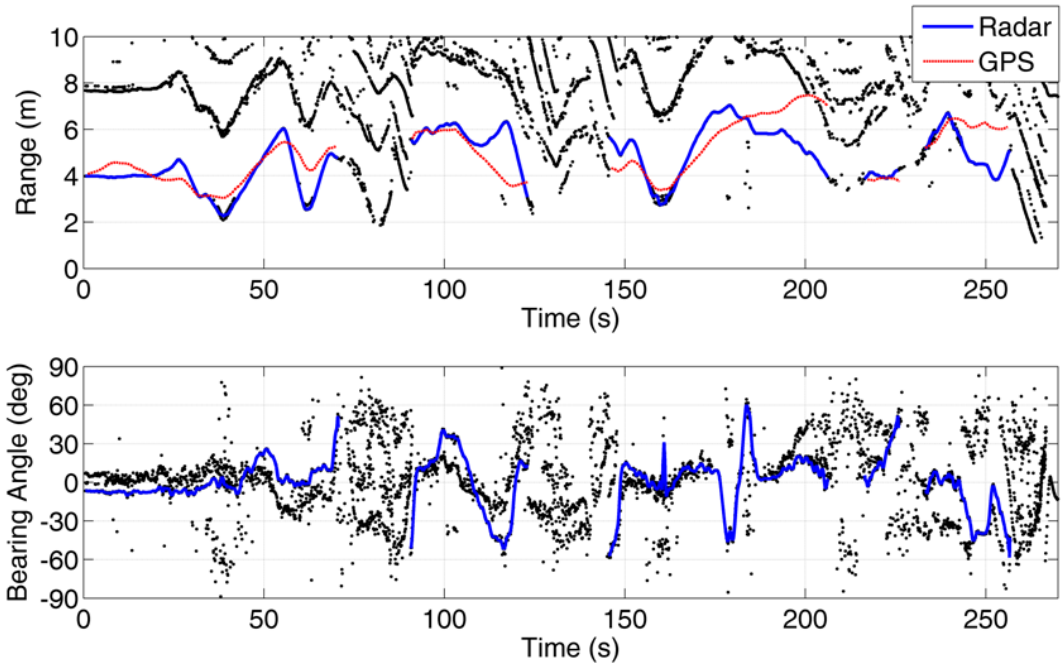

Figure 5.14: Range and bearing angle information for the targets extracted at each acquisition time by means of CFAR algorithm (in black). Confirmed tracks representing relative motion of CR are depicted in blue. Baseline history provided by GPS is depicted in red.

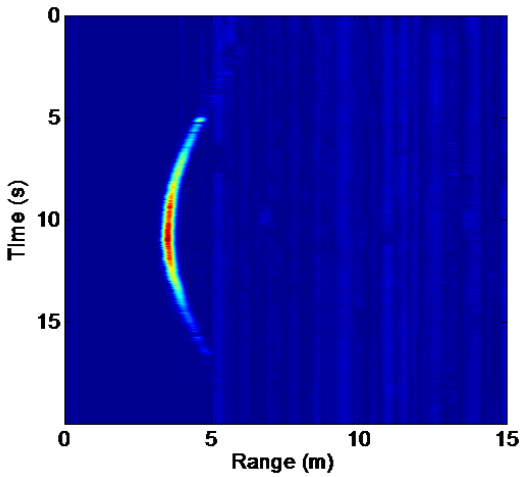

Figure 5.15: Magnitude of range-compressed matrix resulting from straight motion of trihedral CR.

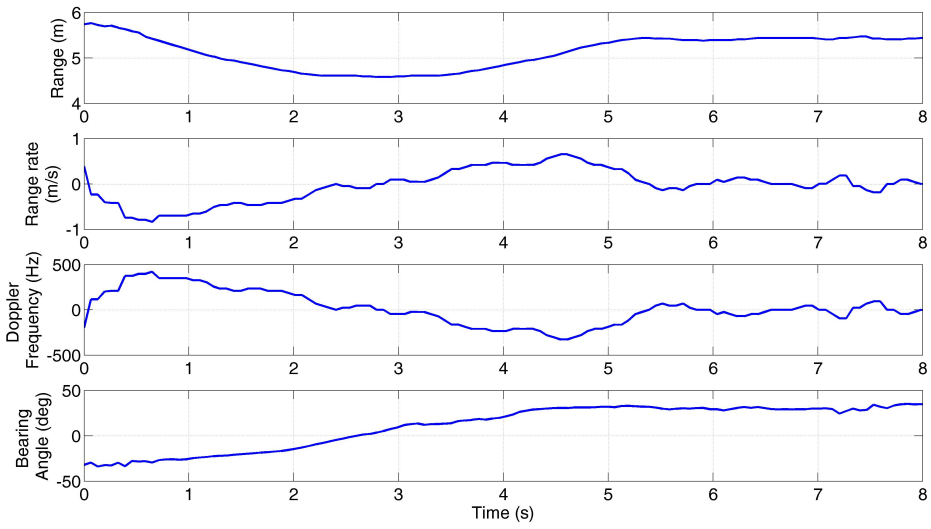

Figure 5.16: Measurements for motion of CR. From top to bottom: range, range rate, Doppler frequency, bearing angle.

Chapter 6

Radar Odometry

Autonomous navigation of UAS has been addressed with difference sensors. With reference to radar-aided navigation, a very promising technique is radar odometry. In this Chapter, the idea of radar-aided navigation by means of radar odometry is presented as well as current techniques for radar-aided navigation. The entire cycle, *i.e.* Target Detection with CFAR algorithm, Multiple-Target Radar Tracking, and Radar Odometry, is discussed in details. Finally, navigation results based on radar odometry are illustrated.

6.1 Radar-aided Navigation

Autonomous navigation systems currently rely on measurements from both Inertial Measurement Unit (IMU) and GPS receiver to be given as input to a Kalman Filter, thus correcting the drift of IMU itself [10]. However, when GPS signal is unreliable or not available, different solutions have to be found in order to bound inertial errors. Furthermore, the limited performance of small and cheap IMUs with which MAVs can be equipped generate a very fast error growth in absence of GPS estimates. Typical algorithms for GPS-denied navigation are based on LIDAR [117] and/or visual odometry [16]. Lidar-based solutions may be lim-

ited to two-dimensional environments and/or pose challenges related to sensor installation onboard micro-UAS. Visual odometry approaches exploit change in perspective of consecutive images to estimate relative motion. Effectiveness of these algorithms is strongly related to performance of electro-optical sensors, which can degrade owing to adverse illumination condition. Radar, on the contrary, is independent of illumination condition and its resolution is independent of range distance. Strong radar reflectors can be detected and tracked in subsequent scans, thus aiding navigation estimates as it is done by image features in vision-based sensing architectures. Within this framework, challenges for tracking may arise from the presence of a large amount of strong radar reflectors in the scene. Moreover, depending on the selected radar wavelength and relative attitude between radar antennas and physical objects, some targets can be detected whereas other ones result not visible [17].

Radar odometry for UAV navigation has been recently proposed, among others, by [118], [119], and [120]. In particular, [118] proposed a simulation of two-dimensional navigation solution based on data from Ultrawideband Orthogonal Frequency Division Multiplexed (UWB-OFDM) radar, mounted in side-looking geometry, as typically done in SAR, on a fixed-wing UAV, and IMU. The multiple-target tracking problem is solved in a white, uniform clutter environment with a Global Nearest Neighbor (GNN) scheme having a M-out-of-N quality filter.

The data from IMU are exploited for state prediction in an Extended Kalman Filter (EKF). [119] and [120] both focus on fixed-wing UAV. Specifically, proposed approaches are tested on data acquired by a high performance SAR flying on a Cessna aircraft.

In particular, [119] uses the Hough transform to extract point scatterers and exploits pairs of scatterers to triangulate position, by assuming constant aircraft heading. The constant-heading assumption is removed in [120], where recursive

RANSAC is exploited to track point scatterers and both absolute and relative range measurements among targets are used within an EKF-based navigation filter.

The problem and the approach presented in this work differ from these recent works in several aspects. First, an existing ultralight radar is considered which can be installed onboard a MAV without significant challenges. The assumed sensor generates both range and bearing measurements, though the latter can be coarser. Then, the present work does not focus only on fixed wing aircraft and side-looking radar installation: the main focus is on a small/micro-UAS, which can move in different directions with different speeds, hover, or even exhibit only attitude rotations, at very low altitude in a GPS-challenging scenario. This also means that the environment can be significantly cluttered, hindering reliable extraction of a large number of strong and stable scatterers. In order to understand if the information provided by a commercially available radar can support navigation in such a challenging scenario, in this work the focus is set on providing a proof-of-concept for radar-only navigation, while we will deal with radar/INS integration in future works.

The idea of radar odometry consists in detecting and tracking fixed targets to be then used to retrieve ownship motion, as it happens for odometry based on optical sensors [121].

The model of radar assumed hereby is a FMCW radar, with a single transmitting (Tx) antenna and two receiving (Rx) antennas having a certain spatial separation. FMCW radar technology is currently used to obtain small and light high range resolution sensors having a limited consumption of energy (see Chapter 1). The reference frame of radar can be defined with respect to antennas (see Figure 6.1): with reference to Figure 6.1a, x axis represents the boresight direction, x-y plane is the azimuth plane, and x-z plane represents the elevation plane. Phase centers of receiving antennas are supposed to be symmetrically

located along the y-axis around the origin of the reference frame (see Figure 6.1b).

Recalling equation (2.7), such sensor provides range information by means of the mapping

$$R = f_R \frac{cT}{2B} \tag{6.1}$$

where f_R is the range frequency, c is the speed of light, T represents the duration of frequency modulation and B the bandwidth of transmitted signal. In addition, when both receiving channels are active, the separation in azimuth enables detection of targets' bearing angle θ_{bea} (see Figure 6.1b) by phase interferometry [20]. This is achieved by using the following equation

$$\theta_{\text{bea}} = \sin^{-1}\left(\frac{\lambda \Delta\Phi}{2\pi L}\right) \tag{6.2}$$

where $\Delta\Phi$ is the difference between phases Φ in the two receiving channels, λ represents the wavelength and L is the distance between the two receivers. Figure 6.1b shows the geometry for bearing angle detection. The unambiguous interval of bearing angle that can be measured with this technique, corresponding to the phase difference ranging from $-\pi$ to $+\pi$, depends on both distance between two receivers, L, and wavelength λ. The angle estimate is only possible along the direction of separation between channels, therefore a full 3D odometer, requiring also elevation angle, is not possible with this setup. It is worth noting that, provided a different definition of reference frame, the following is valid for each radar providing range and bearing information.

In this framework, it is interesting to underline the peculiar characteristics of ultralight radar-based odometry, compared with other sensors. First, odometry is herein based on two-dimensional information, *i.e.* range and azimuth angle, which however derives from a wide three-dimensional field of regard. This mode of operation differs from both 2D LIDAR [122], which works in a single plane, unless the sensor is continuously rotated with respect to the aircraft, and 3D

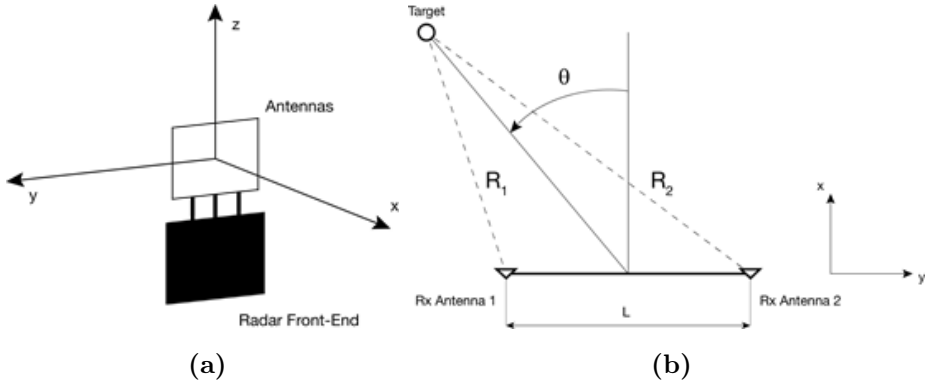

Figure 6.1: Reference frame for radar activities: (a) schematics with respect to antennas and (b) geometry for bearing angle estimation.

LIDAR [117], which directly provides a three-dimensional point cloud. Then, range and angular information is provided with an extremely different accuracy: range resolution is typically fine and approximately range-independent, while angular estimates are coarser, with a degree-level error, thus usually corresponding to a larger linear uncertainty. Moreover, interferometric processing, which provides angular measurements, assumes a single target at each range. Hence, presence of several targets at comparable ranges results in inconsistent angular measurements, to be properly filtered out by the tracking and/or the odometry algorithm. Though radar echoes are generated in the whole field of regard, extraction of strong scatterers leads to a very sparse representation, unlike passive cameras [121] or active RGB-D [123] sensors which both provide spatially dense information. Finally, besides the independence from illumination conditions, an advantage of radar-based odometry compared with vision-based systems is the direct range information, preventing scale drift phenomena which typically affect vision-inertial systems.

In particular, the proposed approach uses radar data to estimate horizontal motion and heading angle. In fact, roll and pitch estimates can be generated exploiting gravity and thus relying on onboard inertial sensors. Then, it is worth

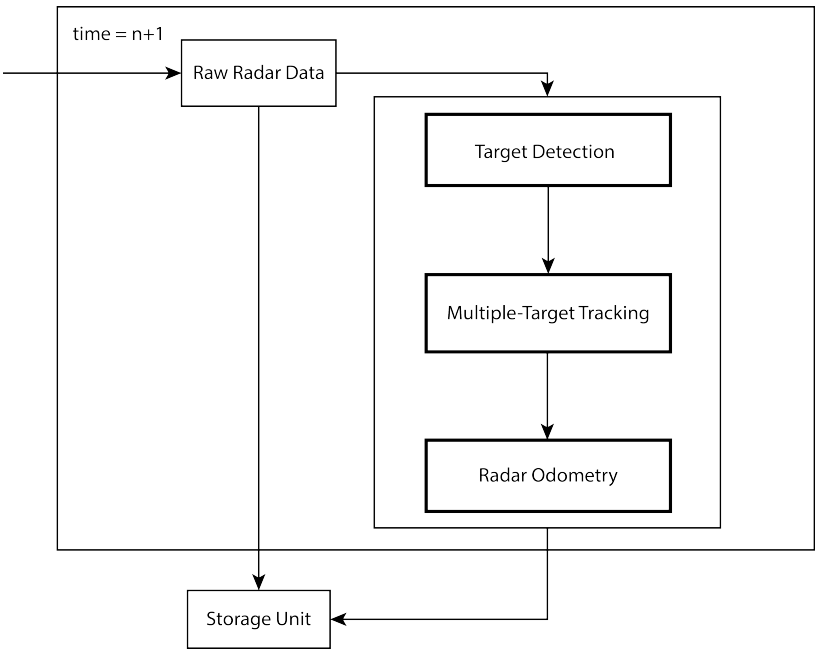

Figure 6.2: Schematics for the entire process of radar-aided navigation.

recalling that height above ground level (AGL) can be estimated based on radar data following the approach described in [124]: the idea is that the closest peak represents the first ground echo, which leads to AGL computation based on the tilt angle of the sensor. A similar approach is also presented in [119]-[120]. As regards horizontal motion and heading, range-based strategies are not adopted since heading variation is unobservable with range-only measurements. Thus in order to provide the requested proof of concept for radar-only navigation an approach is adopted for odometry exploiting both ranges and angles.

The set of operations to achieve horizontal motion and heading angle from raw radar data can be explained by means of the schematic in Figure 6.2. At each time-step radar raw data are stored in external mass unit and fed to data processor. First, the data are processed to detect targets. The output of this block, given by sparse range and azimuth information, is fed to Multiple-Target Tracking (MTT) algorithm. Finally, firm tracks are exploited to provide position and attitude determination in the x-y plane by odometry.

The following sections present a detailed discussion concerning each subset of the processor.

6.2 Target Detection

A reliable extraction of several strong and stable scatterers is necessary to achieve odometry. The Target Detection block is in charge for providing range and bearing information of these kind of scatterers in the scene. This is done in two steps, namely Range-Bearing Estimation and CFAR Detection.

6.2.1 Range-Bearing Estimation

FMCW radars mix received echoes from illuminated scene with a replica of transmitted signal. This operation is carried out in analog within the mixer and has two main advantages: i) the output of the mixer, called beat signal, is already demodulated and has a frequency bandwidth several order of magnitude smaller than the one of transmitted signal. Hence, it can be sampled more easily by analog-to-digital converters (ADC); ii) the beat signal is the sum of sinusoidal functions, whose frequency are proportional to range of each target. In a fashion, the beat signal comes already range-compressed, as the matched-filtering operation is achieved within the mixer.

In-phase, s_i, and quadrature, s_q, components of beat signal are usually sampled and stored separately for each a-th receiving channel. Each beat signal is therefore obtained as

$$s_a\left(t_R, n\right) = s_{i,a}\left(t_R, n\right) + j s_{q,a}\left(t_R, n\right) \tag{6.3}$$

where j represents the imaginary unit, t_R is fast time, i. e. the time referring to the signal transmission/reception at velocity of light, and n the index of time-step. It is worth noting that $s_{i,a}$ and $s_{q,a}$ are both real discrete-time signals,

whereas beat signal s_a is complex discrete-time signal.

Fast Fourier Transform (FFT) applied to (6.3) allows extracting the content of range information stored in the beat signal. This operation is commonly referred to as range compression for FMCW radars in literature, even though it must not be confused with standard range compression performed in pulsed radars [125] and based on matched filtering.

Resulting complex discrete frequency-domain signal for a-th channel can be expressed as

$$S_a\left(f_R, n\right) = M_a\left(f_R, n\right) exp\left\{j\Phi_a\left(f_R, n\right)\right\} \tag{6.4}$$

where f_R represents range frequency, and $M_a\left(f_R, n\right)$ and $\Phi_a\left(f_R, n\right)$ are the magnitude and the phase components, respectively. The overall process up to this point is represented in Figure 6.3. Frequency f_R ranges within the interval $\left[-\frac{f_S}{2}, \frac{f_S}{2}\right]$, where f_S is the sampling frequency. In addition, since f_R is directly proportional to range in FMCW systems, the signal corresponding to frequency subset $\left[-\frac{f_S}{2}, 0\right)$ is discarded, thus working only with positive range bins. It is worth noting that at this point, depending on both required precision in next steps and number of samples available in memory, signal (6.4) could be upsampled by *sinc*-interpolator.

When two receiving channels are enabled, *i.e.* $a = 1, 2$, bearing angle information can be extracted by phase component of (6.4) thanks to equation (6.2) . In (6.2), $\Delta\Phi = \Phi_2 - \Phi_1$. Since it is expected that separation between receivers is very small compared with the range resolution, the magnitude component of two signals (6.4) is averaged non-coherently to achieve partial clutter suppression thus obtaining the value M (see Figure 6.4). Finally, a mapping $f_R \rightarrow R$, *i.e.* range frequency to range, according to (6.1) yields the final time-referenced outputs

$$M\left(R, n\right) \tag{6.5a}$$

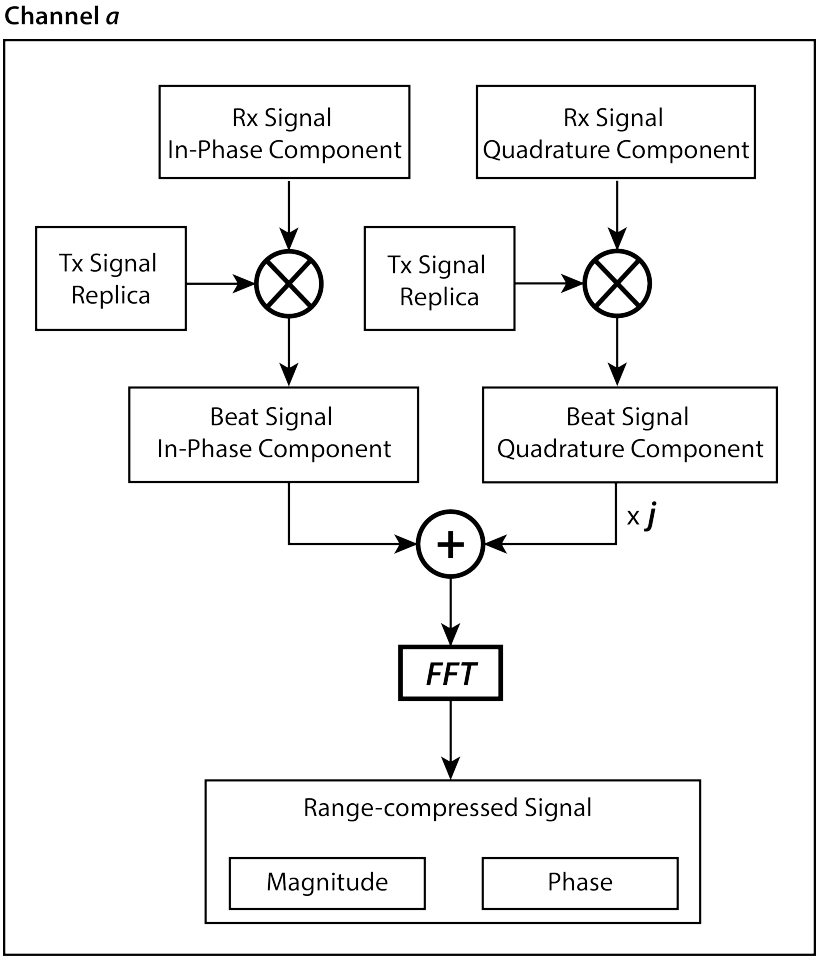

Figure 6.3: Range processing operations at time step n for a-th channel.

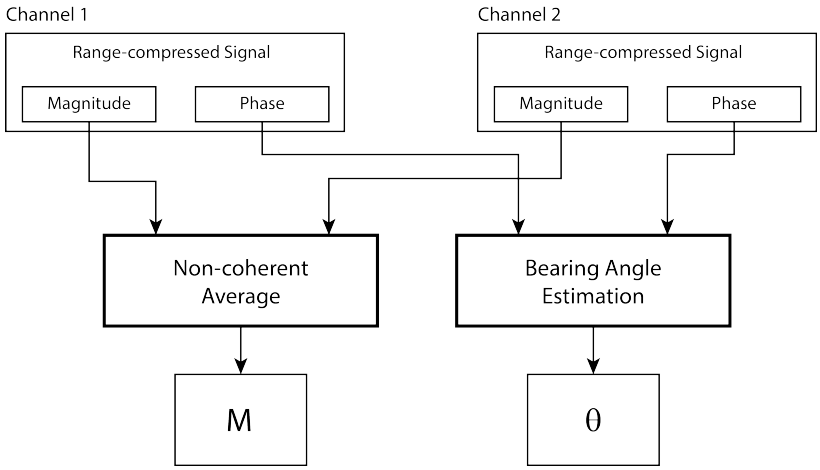

Figure 6.4: Magnitude and Bearing Angle Estimation at time step n. Two channels are active.

$$\theta_{\text{bea}}(R, n) \tag{6.5b}$$

Concerning the presented working principle for the selected radar some further remarks are necessary:

- two or more targets could be at same range but different position along azimuth direction. Since they fall in the same range bin, equation (6.2) fails, *i.e.* it returns a single bearing angle for a single target at that range bin. This could lead to presence of outliers in tracking problem. However, it is unlikely to have outliers for a long time span, being the platform in motion.

- if a target falls in the beam of only one receiving antenna, equation (6.2) yields a wrong bearing information, as one of the phases Φ_a is random. Larger antenna beams restrict this issue to closer range bins.

- when two objects are in adjacent range bins bearing angle of both could experience fluctuations owing to residual phase contribution in response sidelobes.

In any of the previous cases, it is clear that the accuracy of bearing angle measurements could be affected, hence causing errors during tracking operations. Thus, proper strategies are needed to filter these measurements out.

6.2.2 CFAR Detector

Both targets and clutter contribute to amplitude and phase of beat signal (6.3). Consequently, in order to reduce the number of wrong tracks and ease the computational burden within the tracker, it is necessary to filter out the clutter content from signals (6.5) at each time step n.

It is worth recalling that two targets closely spaced could be distinguished in range if their distance along direction of propagation of wave is equal or larger than range resolution [68]. Since range resolution can be conceived as the distance between the points at which the response power is half the peak power response [22, 68] and the square of magnitude (6.5a) is proportional to power [126], the easiest way to discard clutter is setting a constant power threshold. Then, by comparing it with $M^2(R, n)$, for each range cell a target is either present or absent. Despite its simplicity, however, constant threshold has some drawbacks when dealing with MTT. Indeed, farthest targets and weak targets might be discarded if the threshold is set too high (see Figure 6.5). On the contrary, a low threshold might let even clutter pass. In addition, in real radar operations background can vary from time step to time step, thus making ineffective constant threshold and false alarm rate very dependent on environment [128].

Quantitatively, false alarm rate is the ratio of number of false alarms in a single frequency sweep to the number of range cells. Therefore, it holds strong relevance in MTT application [127] and the a commonly accepted requirement is to have constant false alarm rate independent on environmental condition. Constant False Alarm Rate (CFAR) detectors [128]-[136] have been proposed

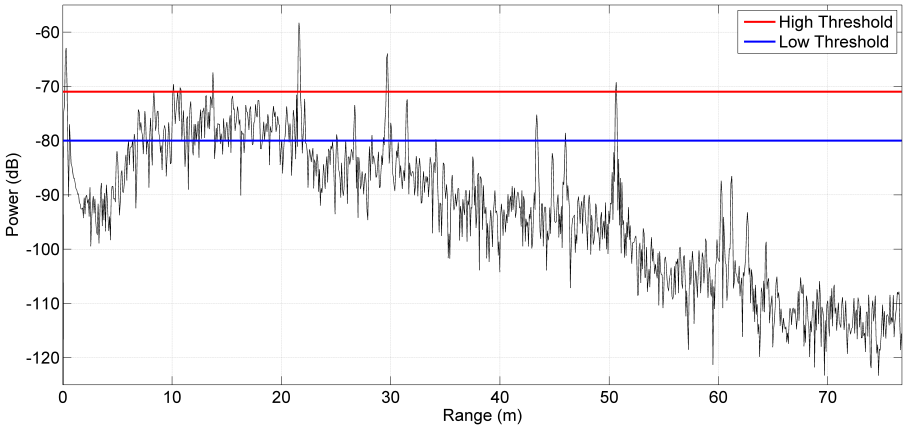

Figure 6.5: Effects of high or low threshold on target detection.

to this reason. For the application presented in this work both Cell Averaging CFAR (CA-CFAR) and Ordered Statistics CFAR (OS-CFAR) [128] have been considered.

Main hypothesis of CA-CFAR detector is that noise and clutter background power levels are represented by independent and identically distributed (i.i.d.) exponential random variables [128]. This is valid when the background is homogeneous. Under the assumption of this statistical model an optimal estimator of noise and clutter level Z_{CA} is obtained by applying the arithmetic mean to power values X_i within a sliding window centered around the Cell Under Test (CUT). That is,

$$Z_{CA} = \frac{1}{N_{CA}} \sum_{i=1}^{N_{CA}} X_i \tag{6.6}$$

where N_{CA} is the number of cell contributing to the average. For each CUT, whose range value is R_{CUT}, the detector compares the power level $M^2\left(R_{CUT}, n\right)$ with the average clutter power times a scaling factor α_{CA}, which is necessary to achieve a probability of false alarm P_{fa}. Therefore, a target is present in CUT if

$$M^2\left(R_{CUT}, n\right) \geq \alpha_{CA} Z_{CA} \tag{6.7}$$

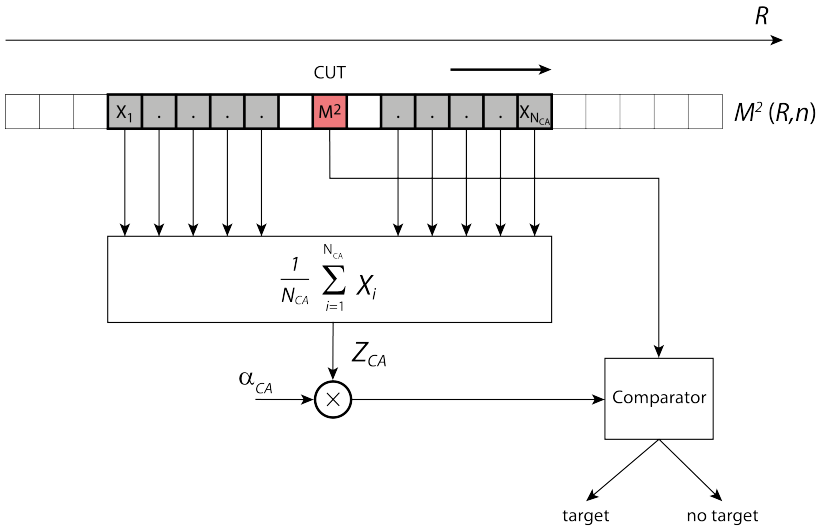

Figure 6.6: CA-CFAR schematic.

CA-CFAR operations are represented in Figure 6.6: CUT is depicted in red and cells within the sliding window (bold outline) contributing to average in grey. It is worth noting that two cells, called guard cells, around the CUT are not used to compute the average. This is to reduce the raise of power due to close interfering targets while estimating Z_{CA}. In general, guard cells could be more than two, depending on the application.

Given a specific length N_{CA} and a desired probability of false alarm P_{fa}, the scaling factor can be obtained by the equation

$$P_{fa} = (1 + \alpha_{CA})^{-N_{CA}} \tag{6.8}$$

which is valid for exponential cumulative distribution function (CDF), as shown in [128].

The choice of length N_{CA} is relevant for resulting estimate of noise power. Indeed a longer sliding window provides a better estimate of noise (6.6), but it is susceptible of variations in statistical distribution of noise. Moreover, CA-CFAR is not robust enough with respect with respect to different clutter background and target situations [129].

OS-CFAR detector, on the contrary, performs better in both cases. The basic idea is that power content X_i of each cell within the sliding window is first rank-ordered according to increasing magnitude [128]. The ordered statistic $X_{(k_{OS})}$ is assumed as noise level. That is,

$$Z_{OS} = X_{(k_{OS})} \tag{6.9}$$

A commonly accepted value for the rank of statistic k_{OS} is $k_{OS} = \frac{3}{4}N_{OS}$ [128]. For each CUT the OS-CFAR detector compares the power level of CUT itself with noise level (6.9) times a scaling factor α_{OS} (see Figure 6.7) and a target is present if

$$M^2 \geq \alpha_{OS} Z_{OS} \tag{6.10}$$

Given a specific length N_{OS} of sliding window and a desired probability of false alarm P_{fa}, when the random variables X_i are exponentially i.i.d. the scaling factor for exponential statistics is obtained, as reported in [128], by

$$P_{fa} = k_{OS} \binom{N_{OS}}{k_{OS}} \frac{(k_{OS}-1)!(\alpha_{OS}+N_{OS}-k_{OS})!}{(\alpha_{OS}+N_{OS})!} \tag{6.11}$$

where $\binom{\cdot}{\cdot}$ indicates the binomial coefficient.

OS-CFAR method can accommodate for different statistical distributions and, in addition, its performance is only slightly affected by the length of sliding windows.

Figure 6.8 shows the output of CA-CFAR and OS-CFAR detectors given as input an actual scene. The probability of false alarm is $P_{fa} = 10^{-3}$ for both cases. It can be seen that both detectors are able to isolate three corner reflectors at around 20 m, 30 m, and 50 m, but CA-CFAR is not able to recognize weaker and close echoes. Detection of such targets is crucial to perform robust radar odometry, so OS-CFAR is preferred in this work.

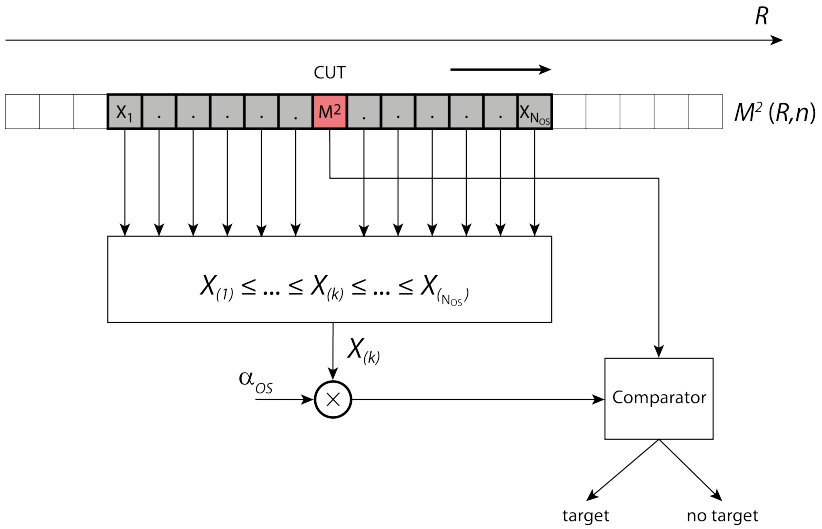

Figure 6.7: OS-CFAR schematic.

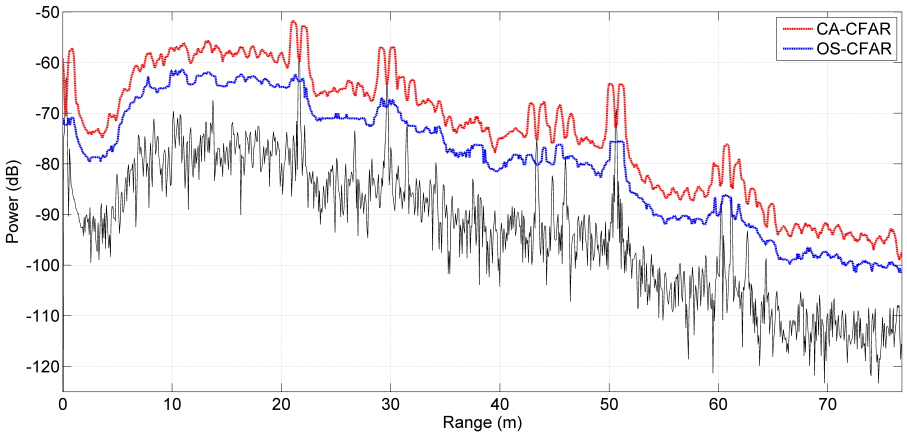

Figure 6.8: Outputs of CA-CFAR (red) and OS-CFAR (blue) with an actual scene. The parameters for CA-CFAR are $\alpha_{CA} = 8.53$, and $N_{CA} = 16$. The parameters for OS-CFAR are $N_{OS} = 24$, $k_{OS} = 18$, and $\alpha_{OS} = 5$. The probability of false alarm is $P_{fa} = 10^{-3}$ for both cases.

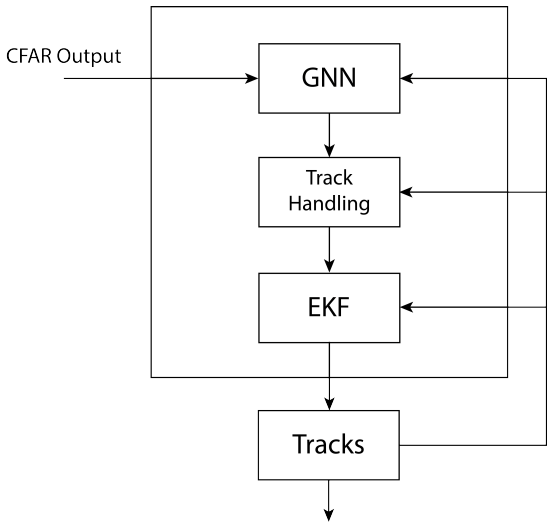

Figure 6.9: Multiple-Target Tracking schematics.

6.3 Multiple-Target Tracking

Several algorithms have been addressed in literature to handle multiple-target tracking problem [127],[137],[138]. In the framework of this work the Global Nearest Neighbor (GNN) algorithm has been implemented since it is fast and reliable method when it is not expected to have a significant amount of densely spaced targets (also considering sensor resolution and sampling time) [127]. The complete logic behind GNN, track handling, and Extended Kalman Filter (EKF) is depicted in Figure 6.9.

6.3.1 Global Nearest Neighbor

The aim of GNN is to associate new measurements with correct available tracks. First step requires the evaluation of the statistical distance between each i-th measurement and each k-th track

$$CM(i,k) = \frac{(R(i) - \hat{R}(k))^2}{\sigma_R^2} + \frac{(\theta_{\text{bea}}(i) - \hat{\theta}_{\text{bea}}(k))^2}{\sigma_{\theta_{\text{bea}}}^2} \tag{6.12}$$

where σ_R and $\sigma_{\theta_{\text{bea}}}$ are the range accuracy and the angular accuracy, respectively, $\hat{R}$ and $\hat{\theta}_{\text{bea}}$ represent the estimates of range and bearing angle at the considered

time step, and CM stands for the distance cost function matrix.

Then, it is necessary to define a decision criterion for either rejecting or accepting the possible matching. This is done by setting a gate G. Since a random Chi-Square distribution can be assumed for CM statistics [127], the gate is $G = 9.21$. This value is the inverse of Chi-Square cumulative distribution function, having 2 degrees of freedom and probabilities in 0.99. It is important to remark that the use of the gate G can be interpreted as the introduction of an ellipse of uncertainty in the $R - \theta_{\text{bea}}$ plane.

Hence, if

$$CM(i,k) > G \tag{6.13}$$

i-th measurement falls outside the ellipse of uncertainty and is discarded for association with k-th track with a probability of correct decision greater than 0.99.

Last step deals with the optimal assignment problem, *i.e.* finding the measurement-track pairs that minimize the cost function. Munkres' algorithm provides the pairing between tracks and measurements with minimum distance [139]. It is worth noting that the Munkres' algorithm was developed for square cost function matrix. However, the algorithm works also when it is rectangular [140], *i.e.* when the number of tracks and the number of measurements are not equal.

6.3.2 Track Handling

The handling of tracks has a crucial role in the whole MTT process, as it involves initiation, maintenance, and termination of tracks. Indeed, handling is in charge for providing proper information to EKF subset in successive time steps.

Typically, two kinds of track can be distinguished, namely tentative tracks and firm tracks. Tentative tracks are initiated whenever new measurements that do not match with existing tracks are present. These tracks are not used for operations until they satisfy specific requirements. When these conditions

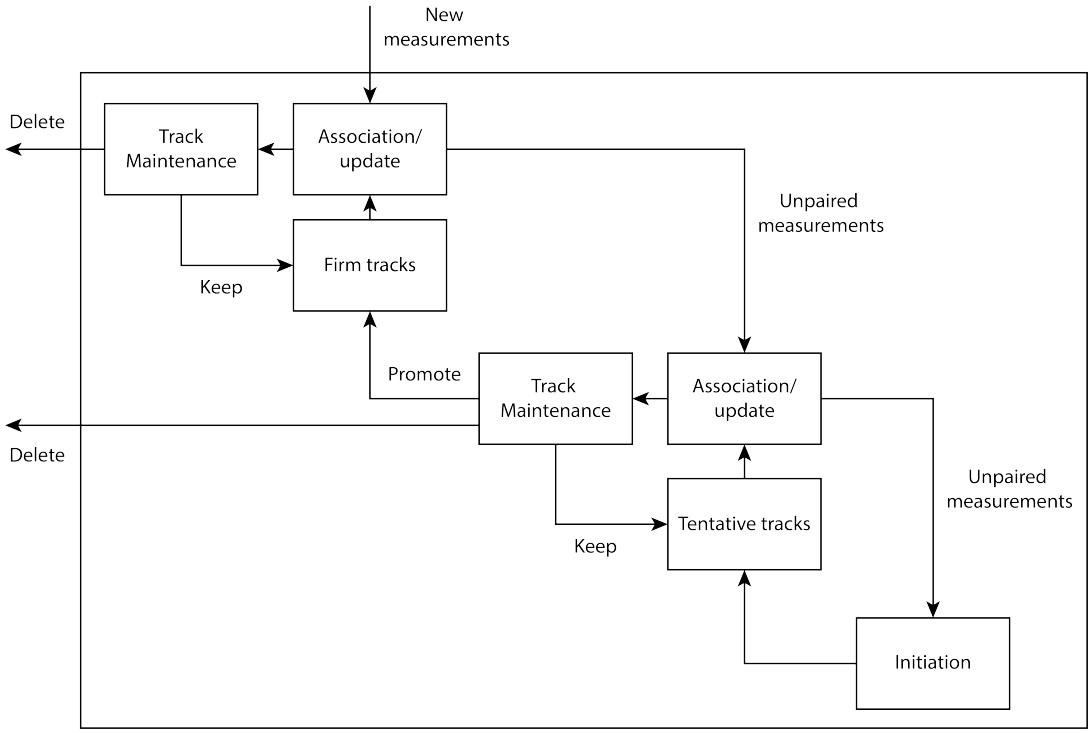

Figure 6.10: Track handling schematics.

occur, they are promoted to firm tracks. Hence firm tracks reasonably represent true targets tracked in the scene, so they can be used for applications, e.g. for odometry.

The logic behind handling of tracks in the presented work is based on *M-out-of-N* quality tests [127]. The complete cycle is explained in the following and shown in Figure 6.10.

At step one, new tentative tracks are initiated from incoming measurements. The initial state vector and covariance matrix to be fed into EKF are represented by $\hat{\mathbf{x}}_0$ and $\hat{\mathbf{P}}_0$. It is worth noting that, when tentative tracks are initiated, a larger initial covariance is set for velocities, which are not equal to zero in the most general case. At successive steps, the GNN algorithm tries to match the new incoming radar measurements with existing tentative tracks. If a tentative track is paired with a measurement, then a flag for promotion of tentative track

to firm track is raised. The measurement $\mathbf{z}_n$ and the estimated state $\bar{\mathbf{x}}_n$ and covariance $\bar{\mathbf{P}}_n$ feed the EKF, generating estimated state and covariance of next position. If after N_t steps at least $M_{t,p}$ flags for association have been raised, then the tentative track is promoted to firm. On the contrary, if there is no match, the estimated state vector and covariance matrix are only propagated according to dynamic model (6.16a) and a deletion flag is raised. If after N_t steps at most $M_{t,d}$ flags for deletion have been raised it is deleted.

Similarly to tentative tracks, if a firm track is paired with measurement then new estimated state vector and covariance matrix are generated by EKF. If no association occurs, a deletion flag is raised and state vector and covariance matrix are propagated with dynamic model (6.16a). When firm tracks are addressed, *M-out-of-N* quality test is active only for deletion. That is, if at least $M_{f,d}$ deletion flags are raised during last N_f steps, then firm track is deleted. The value of $M_{f,d}$ has to be selected carefully. Indeed, if target disappears from the scene, the track is propagated for a time $T_{wp} = \dfrac{M_{f,d}}{f_{update}}$ before deletion. A large value of $M_{f,d}$ could yield wrong results within the odometry block. A small value could degrade tracker efficiency, instead.

It must be remarked that when firm tracks are present, the algorithm tries to associate measurements to firm track first. Measurements not paired with firm tracks are then considered for association with tentative tracks. Finally, new tentative tracks are generated by measurements not associated with any of those. This approach may prevent tentative tracks to be updated with new measurements. On the contrary, it reduces possibility that tentative tracks interfere with and degrade firm tracks.

6.3.3 Extended Kalman Filter

GNN algorithm needs predictions of range and bearing angle to compute statistical distance and pair tracks with measurements. The estimates are generated

in a cartesian reference frame x-y (see Fig6.1) whereas measurements are in two-dimensional polar format, *i.e.* range and bearing angle. Hence, a non-linear estimation problem is set. An adequate non-linear estimator is Extended Kalman Filter [127],[137],[141]. A dynamic model based on 4 states is selected. Therefore, EKF with quasi-constant velocity model is applied. This model assumes that process noise is Gaussian zero mean white noise acceleration. The state vector is given by

$$\mathbf{x} = [x \quad \dot{x} \quad y \quad \dot{y}]^T \tag{6.14}$$

The operator $(\cdot)^T$ indicates transpose operation. $\mathbf{P}$ is the state covariance matrix. Coordinates x and y and respective velocities $\dot{x}$ and $\dot{y}$ refer to radar reference frame shown in Figures 2-3. The discrete-time state dynamics equations at step n are

$$\mathbf{x}_n = \mathbf{F}\mathbf{x}_{n-1} + \mathbf{w}_n \tag{6.15a}$$

$$\mathbf{z}_n = \mathbf{h}\left(\mathbf{x_n}\right) + \mathbf{v}_n \tag{6.15b}$$

where the $\mathbf{F}$ is the linear discrete-time transition matrix, $\mathbf{w}_n$ represents process noise, *i.e.* uncertainties in the quasi-constant velocity model, and has discrete-time covariance matrix $\mathbf{Q}$, $\mathbf{z}_n$ stands for the observation vector, $\mathbf{h}\left(\mathbf{x_n}\right)$ accounts for the non-linear discrete-time observation matrix, and finally $\mathbf{v}_n$ is the measurement noise vector having discrete-time covariance matrix $\mathbf{R}$.

The implementation of EKF is

$$\begin{cases} \bar{\mathbf{x}}_n &= \mathbf{F}\hat{\mathbf{x}}_{n-1} \\ \bar{\mathbf{P}}_n &= \mathbf{F}\hat{\mathbf{P}}_{n-1}\mathbf{F}^T + \mathbf{Q} \end{cases} \tag{6.16a}$$

$$\begin{cases} \mathbf{z}_n &= \begin{bmatrix} R & \theta_{\text{bea}} \end{bmatrix}^T \\ \hat{\mathbf{z}}_n &= \mathbf{H}\bar{\mathbf{x}}_n \\ \varepsilon_n &= \mathbf{z}_n - \hat{\mathbf{z}}_n \\ \mathbf{K}_n &= \bar{\mathbf{P}}_{n-1}\mathbf{H}^T \left[\mathbf{H}\bar{\mathbf{P}}_n\mathbf{H}^T + \mathbf{R}\right]^{-1} \\ \hat{\mathbf{x}}_n &= \bar{\mathbf{x}}_n + \mathbf{K}_n\varepsilon_n \\ \hat{\mathbf{P}}_n &= \left[\mathbf{I} - \mathbf{K}_n\mathbf{H}\right]\bar{\mathbf{P}}_n \end{cases} \tag{6.16b}$$

where the operators $\bar{(\cdot)}$ and $\hat{(\cdot)}$ represent prediction and estimation, and

$$\mathbf{F} = \begin{bmatrix} 1 & \Delta t & 0 & 0 \\ 0 & 1 & 0 & 0 \\ 0 & 0 & 1 & \Delta t \\ 0 & 0 & 0 & 1 \end{bmatrix} \tag{6.17a}$$

$$\mathbf{Q} = \begin{bmatrix} \frac{\Delta t^3}{3} & \frac{\Delta t^2}{2} & 0 & 0 \\ \frac{\Delta t^2}{2} & \Delta t & 0 & 0 \\ 0 & 0 & \frac{\Delta t^3}{3} & \frac{\Delta t^2}{2} \\ 0 & 0 & \frac{\Delta t^2}{2} & \Delta t \end{bmatrix} q \tag{6.17b}$$

$$\mathbf{H} = \left.\frac{\partial \mathbf{h}\left(\mathbf{x_n}\right)}{\partial \mathbf{x}}\right|_{\hat{\mathbf{x}}_0} = \begin{bmatrix} \cos\theta_{\text{bea}} & 0 & \sin\theta_{\text{bea}} & 0 \\ -\frac{\sin\theta_{\text{bea}}}{R} & 0 & \frac{\cos\theta_{\text{bea}}}{R} & 0 \end{bmatrix} \tag{6.17c}$$

$$\mathbf{R} = \begin{bmatrix} \sigma_R^2 & 0 \\ 0 & \sigma_{\theta_{\text{bea}}}^2 \end{bmatrix} \tag{6.17d}$$

and Δt is time interval between successive steps. The error between real and predicted measurements is ε_n and Kalman Gain is $\mathbf{K}_n$. It is worth noting that values of scale factor q in discrete-time process noise covariance matrix $\mathbf{Q}$ depend on the application at hand. In general, these values might be different for x and y so that changes in velocity over the time interval Δt are on the order of $\sqrt{Q_{22}} = \sqrt{q_x \Delta t}$ and $\sqrt{Q_{44}} = \sqrt{q_y \Delta t}$, respectively. However, since in the

present model same acceleration is expected for both coordinates, they are equal, that is, $q_x = q_y = q$.

Finally, when a new track is initiated, the initial state is obtained by radar measurements $\hat{\mathbf{x}}_0 = [R\cos\theta_{\text{bea}} \quad 0 \quad R\sin\theta_{\text{bea}} \quad 0]^T$ and initial covariance $\hat{\mathbf{P}}_0$ is computed in state space using measurement model and initial measurements.

6.4 Radar Odometry

Range and bearing angle data provided by MTT are converted into a point cloud. Since elevation angle is unknown, it is neglected for all the echoes. Given two point clouds acquired in consecutive scans, relative translation and rotation are computed thanks to 3D-to-3D odometry based on Singular Value Decomposition (SVD) [121].

In details, if **PC1** and **PC2** are the point clouds, each comprising N_{pc} points, at times t_1 and t_2, the rotation matrix and the translation vector which transform **PC1** into **PC2** are found as follows. First, the point cloud centroids $\mathbf{C}_1$ and $\mathbf{C}_2$ are calculated. The covariance matrix is computed as

$$\mathbf{H}_{odo} = \sum_{i=1}^{N_{pc}} \left(PC1_i - \mathbf{C_1}\right)\left(PC2_i - \mathbf{C_2}\right)^T \tag{6.18}$$

Then, the rotation matrix $\mathbf{R}_{odo}$ is given by

$$[\mathbf{U}, \mathbf{S}, \mathbf{V}] = SVD\left(\mathbf{H}_{odo}\right) \tag{6.19a}$$

$$\mathbf{R}_{odo} = \mathbf{V}\mathbf{U}^T \tag{6.19b}$$

and the translation vector is obtained as

$$\mathbf{t}_{odo} = -\mathbf{R}_{odo}\mathbf{C_1} + \mathbf{C_2} \tag{6.20}$$

From the odometry point of view, $-\mathbf{t}_{odo}$ and $\mathbf{R}_{odo}^T$ individuate translational and rotational ownship motion. In the considered radar-only odometry a two-

dimensional approximation is introduced, meaning that both roll and pitch angles and vertical translation are neglected (*i.e.*, they are set to zero). This means that translation vector is estimated in the x-y plane together with the heading angle. As previously stated, roll and pitch angles, and vertical coordinate (AGL), are estimated on the basis of different strategies.

It is worth noting that RANSAC processing has not been adopted at odometry level owing to the relatively small number of confirmed tracks, which makes its application impractical. However, particular attention to outlier rejection is dedicated within the tracking algorithm, thus avoiding the processing of unstable and unreliable angle measurements.

6.5 Experimental Results and Validation

The following subsections provide a description operative setup, scene, and present experimental results.

6.5.1 Operative setup and scene

The operative experimental setup includes the 24-GHz SENTIRE Radar, a Toshiba Satellite L855 laptop (Intel Core i7-3610QM – 6GB RAM), u-blox GPS receiver, and a mobile phone camera, all connected and housed onboard a handheld platform (see Figure 6.11). This operative choice does not affect the validity of results and serves as a basis to future experimental tests with setup housed onboard mini- or micro-UAS. The radar is mounted in a forward-looking position and supplies data to laptop via a SPI-to-USB connector. The camera and GPS receiver provide ground truth information, useful to validate results yielded from processing of radar data. Additionally, a script developed in Python language commands radar acquisition and synchronizes data from radar with packets received by GPS receiver. It is worth noting that GPS receiver returns both raw

GPS data and own navigation solution. Reference solution used in this paper as ground truth is computed from raw GPS data via the pseudorange equations [142]. The algorithm for acquisition code is shown in Figure 6.12. The radar has been set with parameters listed in Table 6.1. The transmitted bandwidth yields to range resolution $dr = 15$ cm. The number of radar samples for each time step is 1024. The selected value of sampling frequency corresponds to a maximum detectable distance of 105m.

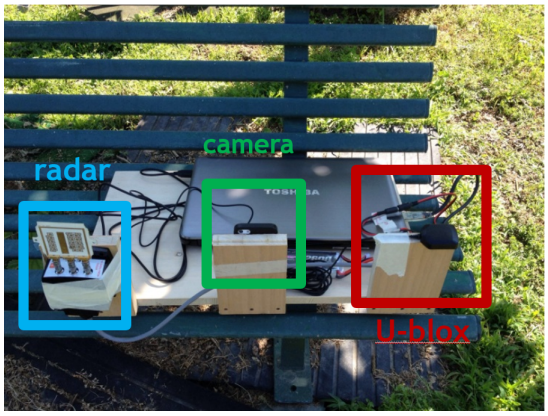

Figure 6.11: Setup: radar, laptop, gps receiver, camera, and platform.

Table 6.1: Radar Settings

Transmitted Bandwidth	$B = 1$GHz
Frequency Modulation	Linear
Ramp Duration	$T = 1$ms
Sampling Frequency	$f_S = 1401.7$kHz

The test site is a non-flat grass field. Man-made objects such as light poles and other metallic scatterers are present in the scene, as well as three trihedral corner reflectors (CRs) equipped with dedicated GPS receivers (see Figure 6.13). It is important to highlight that both CRs and their dedicated GPS receivers

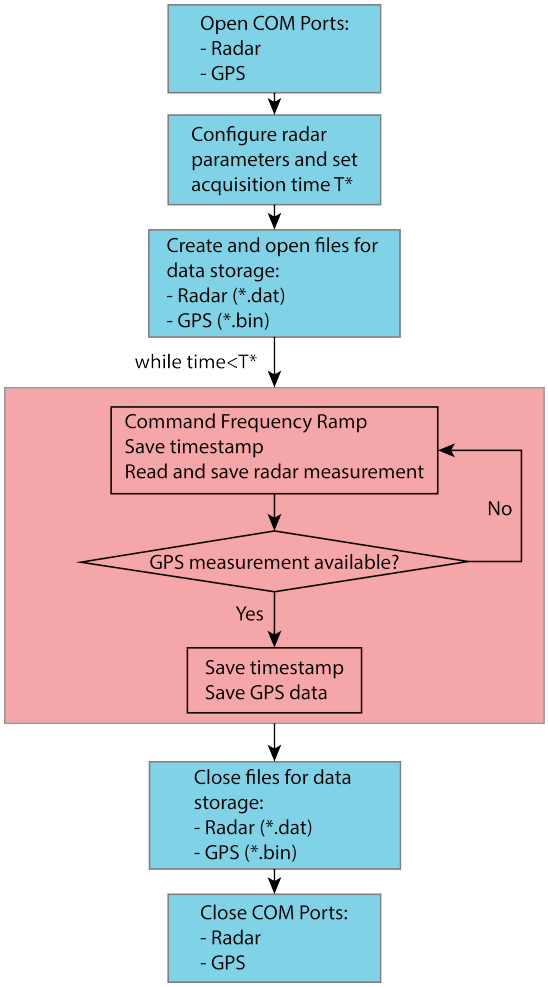

Figure 6.12: Algorithm for combined radar and GPS data acquisition.

are not necessary for tracking purposes but they provide an useful term of comparison when assessing radar detection capabilities. GPS receiver on platform has provided information on the path followed during data acquisition. Total duration of campaign is 300s.

The path covered by the platform during the campaign is shown in Figure 6.14 together with position of CRs, whose identifiers are the same as in Figure 6.13. It is worth noting that both overall path and positions of CRs suffer from limited standalone GPS accuracy. Nevertheless, GPS provides a good indication about relative motion between radar and CRs thus being able to support data

analysis and performance assessment.

Figure 6.13: Test site and environment for measurements. Three CRs are visible in red, blue, and green boxes.

6.5.2 Target Detection

The first part of target detection relies on processing of beat signals (6.3). Indeed, at every time step, each of which corresponding to a successive signal transmission by radar module, magnitude and bearing angle contents are extracted from beat signals of both receiving channels. It has been shown that after FFT one half of signal is discarded. Therefore, an up-sampling factor $k_{ups} = 2$ is selected to operate on the same number of range samples.

Magnitude and bearing angle can be conveniently sorted in two matrices, so to better illustrate results, as shown in Figure 6.15. Each column represents data for a single time step. The magnitude matrix shows a bright constant return at zero range due to power leakage into receiving channels. This return is discarded by further processing steps. Moving to larger ranges a dark area appears. This is due to absence of targets within this range interval and can

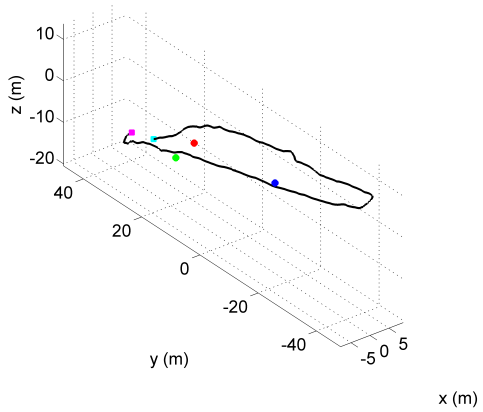

Figure 6.14: Path covered during platform motion as provided by GPS solution. Red, blue, and greed dots are CRs. Magenta and azure squares represent starting and ending points, respectively, during the 300s-long data collection campaign.

be interpreted as thermal noise. Then, bright area appears when targets and clutter are illuminated. The brightest returns are due to CRs and man-made metallic objects. It is worth noting that power levels, and therefore magnitude levels, are decreasing with fourth power of distance. At this point, interpretation of bearing angle matrix is not so easy, though.

When information (6.5a) is available, OS-CFAR detector can be exploited. The parameters of OS-CFAR detector are listed in Table 6.2. It is worth highlighting that these settings yield a probability of false alarm $P_{fa} = 10^{-2}$. This operative choice is acceptable in the framework of this work: indeed, in order to reconstruct motion it is necessary to account even for still and weak targets in the scene. Moreover, the proposed processing chain is expected to be robust against residual false alarms that are likely to be generated by OS-CFAR. Isolated false detections can be filtered out at tracking level thus not impacting the odometry solution.

Output of OS-CFAR detector is shown in Figure 6.16. For each time step,

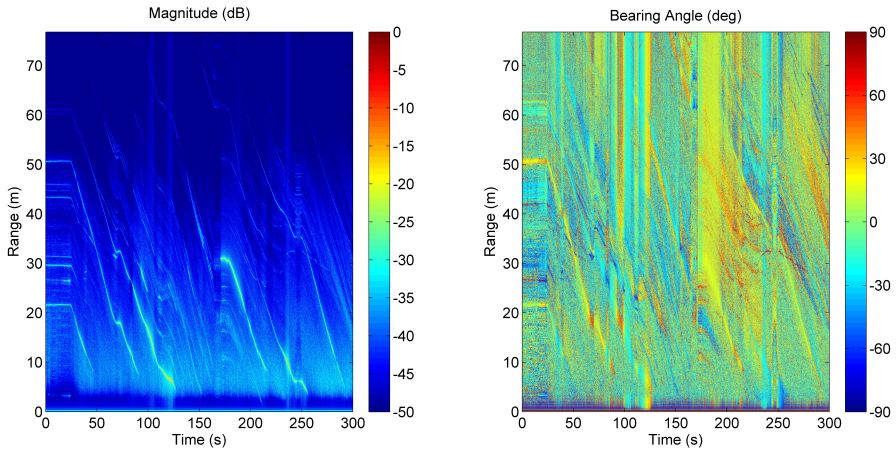

Figure 6.15: Magnitude (left) and bearing angle (right) maps as function of range and time.

Table 6.2: OS-CFAR Settings

Number of cells	$N_{OS} = 24$
Index of selected Ordered Statistic	$k_{OS} = 18$
Scaling Factor	$\alpha_{OS} = 3$

range, bearing angle, and magnitude are extracted. The color of markers corresponds to the sequence of detections, from the closest to the furthest one, e.g. blue marker always indicates the closest detection, green marker is the second closest one, and so on. Hence, the colors of the two plots show that at this point measurements from same targets are not numerically associated in tracks. It is also worth noting that the points corresponding to bearing angles lay within an interval twice as large as the azimuth main beam, that is, the null-to-null aperture. Points at around $\pm 90°$ are outliers due to power leakage and therefore need to be deleted.

Range information provided by GPS is depicted in Figure 6.17 together with range output of OS-CFAR detector and suggests that CRs are properly retained

and other targets, mainly man-made objects, are kept, too. Some remarks on comparison with GPS information are necessary: i) the slight mismatch between radar tracks and GPS tracks is due to both standalone GPS accuracy and latency within the internal buffer of radar sensor; ii) range information provided by GPS does not consider the field of view of radar, therefore the distance between radar and CRs is computed even when CRs are not illuminated, e.g., when CRs are behind the platform.

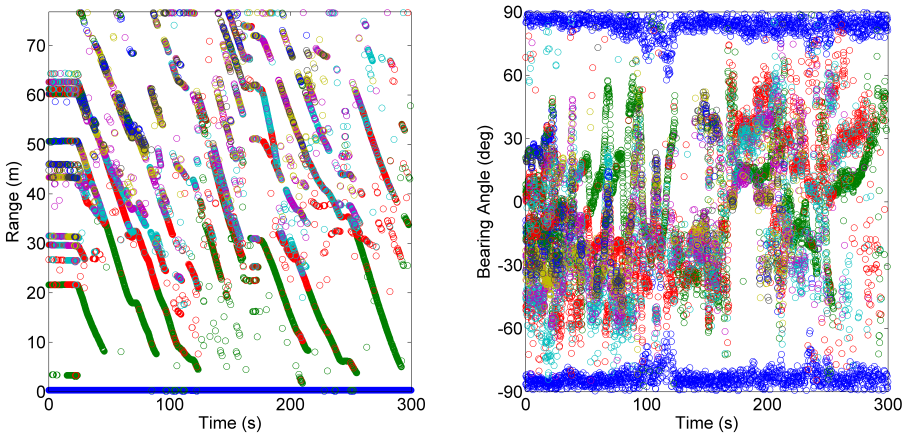

Figure 6.16: Output of OS-CFAR detector: range (left) and bearing angle (right).

6.5.3 Multiple-Target Tracking

The parameters for GNN, EKF, and Track Handling have been set according to radar characteristics and envisaged scenario. Table 6.3 lists settings for both EKF (distance and bearing angle accuracy) and Track Handling. The value of the noise covariance scale factor q depends on the maximum expected acceleration in a time step. The selected value is representative of the slow platform motion.

Untuned values can affect the state prediction and therefore the association process. As for the track handling, decision criteria *M-out-of-N* are listed in

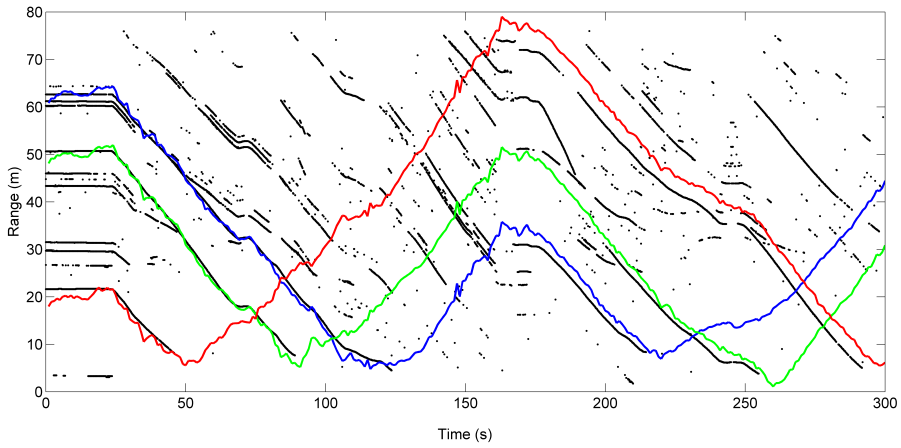

Figure 6.17: Output of OS-CFAR detector and range to CRs provided by GPS receiver.

Table 6.3. If a tentative track is wrongly promoted to firm and then no other measurements are associated, the algorithm deletes the track in just 6 time steps, corresponding to less than 0.7s.

Table 6.3: MTT Settings

EKF	radar range accuracy	$\sigma_R = 10\text{cm}$
	radar angular accuracy	$\sigma_{\theta_{\text{bea}}} = 15°$
	process noise scale factor	$\sqrt{q} = 1\text{m/s}^{1.5}$
Track Handling	test interval for tentative tracks	$N_t = 16$
	deletion of tentative tracks	$M_{t,d} = 6$
	promotion of tentative tracks	$M_{t,p} = 9$
	test interval for firm tracks	$N_f = 16$
	deletion of firm tracks	$M_{f,d} = 6$

The number of different firm tracks generated during the whole campaign is 133. Figure 6.18 shows a comparison, by means of superimposition, of detections provided by OS-CFAR detector with measurements associated to firm tracks.

It can be noted that the tracker is able to follow strong targets and reject bad-quality measurements. Angular measurements are more noisy compared with range measurements but EKF, as expected, is able to provide smoother data (see Figure 6.19). The smoothing has very little effect on range but is significant on bearing angle.

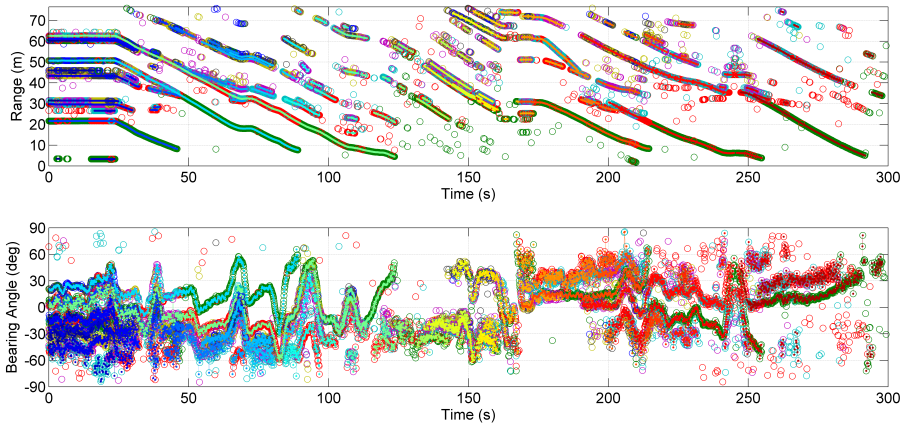

Figure 6.18: Comparison of detections provided by OS-CFAR detector (empty circles with same colour meaning as in Figure 6.16) with measurements associated to tracks (thin lines with different colours for each track).

The number of firm tracks, tentative tracks, and available targets at each time step is shown in Figure 6.20. On average at each time step approximately 4 firm tracks can be exploited.

The relatively limited number of firm tracks is also a consequence of the tested radar geometry. In details, since the platform is moved by a human operator, most of targets are observed with very small grazing angle. This geometry makes radar response from natural targets quite weak, thus limiting the number of both detections and tracks that can result from the processing. It must be remarked, though, that the number of firm tracks is higher when the platform is still, at initial time, and has a drop when the platform exhibits yaw rotations without translation, e.g. around $t = 170$s, when a complete turn has

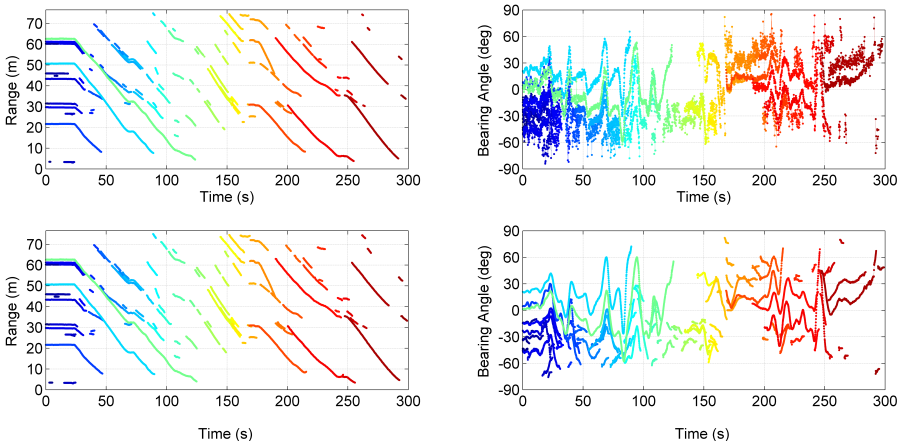

Figure 6.19: Comparison of measurements associated to tracks (top) with smoothed data provided by EKF (bottom).

been made, and around $t = 250$s. This is also due to the low number of targets seen during these operations. Additionally, it can be noted that both number of detections and number of firm tracks exhibit the same trend, whereas the number of tentative tracks is varying, due to presence of low-quality tracks.

In absence of further controls on quality of tracks, the probability of false alarm should not be increased further to avoid wrong tracks affecting quality of odometric results.

6.5.4 Radar Odometry

Firm tracks generated in the MTT block have been fed into the radar odometer. Results have been compared with ground-truth ground-truth obtained with raw GPS data provided by standalone GPS receiver housed onboard the platform. The odometer is started when the platform begins its motion, at time step $n = 200$. The entire duration of odometry with radar only is about 60s. For sake of clarity, the tracks used for odometry are represented in Figure 6.21. The trajectory given by GPS solution and the trajectory reconstructed with radar

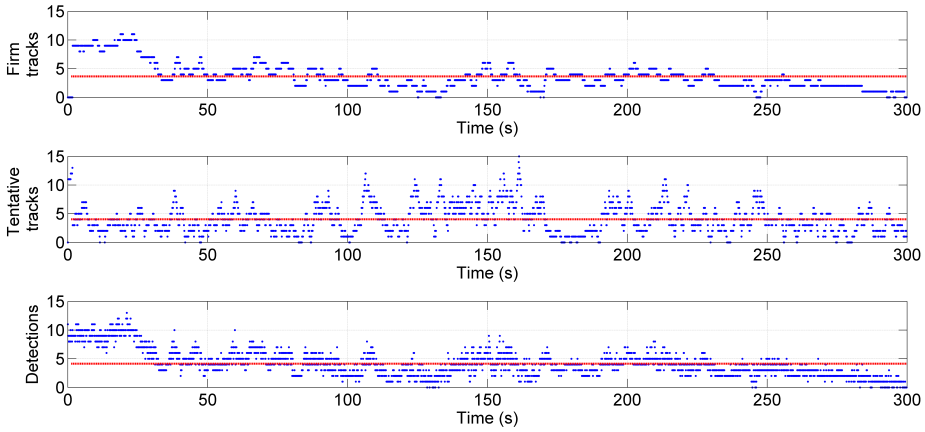

Figure 6.20: Number of firm tracks, tentative tracks, and detections at each time step during the experimental campaign. Red lines represents the average values.

odometry in a North-East reference plane are presented in Figure 6.22.

Qualitatively, the solution obtained with radar-only odometer is acceptable. That is, it is able to follow ownship motion. Challenges are mainly related to the discrimination between rotation and translation. This is amplified when the platform rotates without translation (see Figures 6.23a-6.23b), *i.e.*, in rotation-only phases.

By means of rigid rotation, the North-East plane can be transformed into Forward Range-Cross Range reference plane. This allows a better comprehension of the results. In fact, the error is mostly of the order of standalone GPS uncertainty [142] (see also Table 6.4). Table 6.4 and Figure 6.24 show, as expected, that forward motion is tracked in a more accurate way (see Figure 6.24a) since its accuracy is basically related to range accuracy whereas cross track motion has an oscillatory error (see Figure 6.24b) mainly due to coarse radar angular accuracy.

The explanation for these results is the following. When the platform experiences either rotational-only motion or quasi rotational-only motion, *i.e.* with

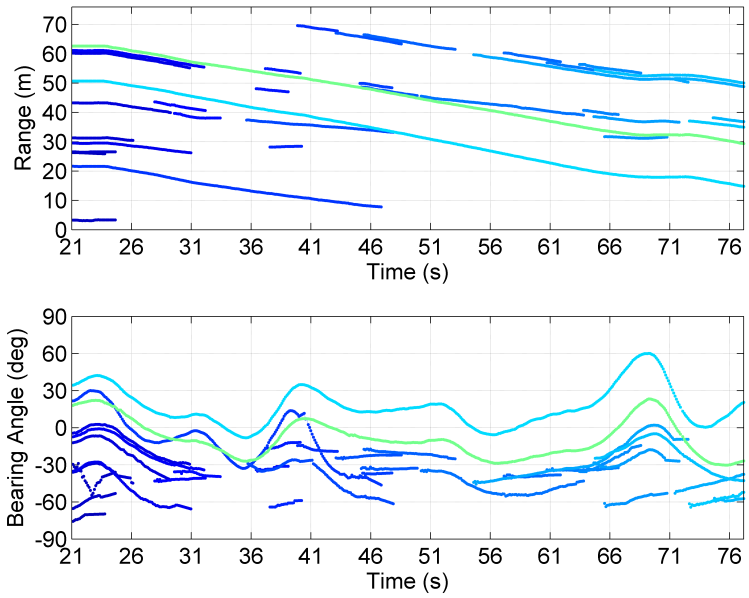

Figure 6.21: Details of firm tracks used for radar odometry. Range (top) and bearing angle (bottom).

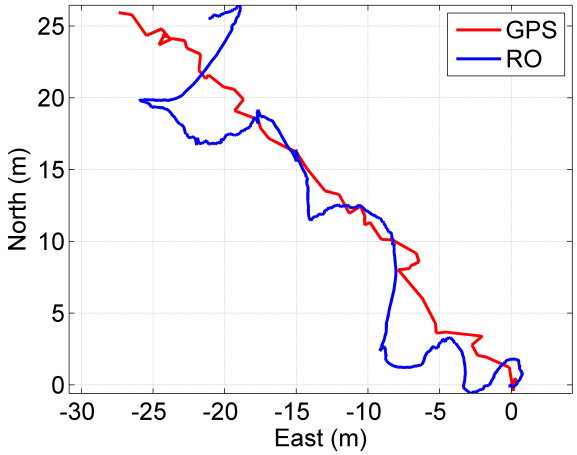

Figure 6.22: North-East trajectory.

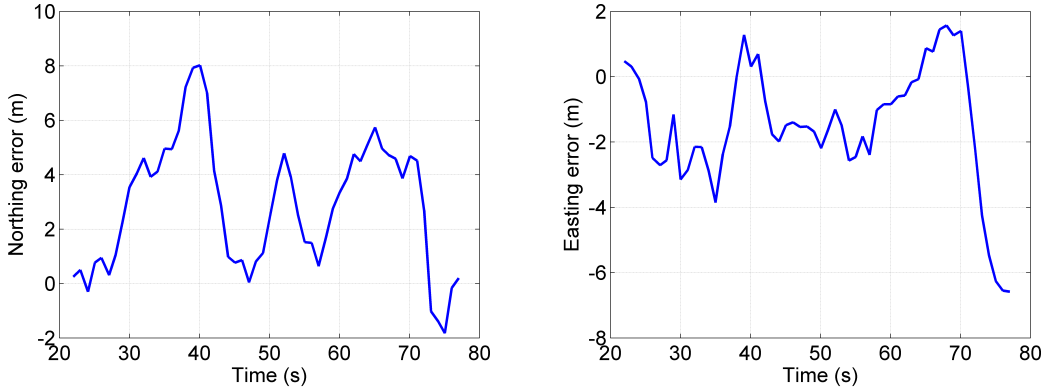

(a) Error in North direction. **(b)** Error in East direction.

Figure 6.23: Errors in North-East plane.

Table 6.4: Statistics of errors

Error	Mean	Root Mean Square	Standard deviation
North	2.89 m	3.72 m	2.36 m
East	-1.50 m	2.41 m	1.91 m
Forward	3.18 m	3.51 m	1.49 m
Cross	0.71 m	2.72 m	2.65 m

very small translation, the current odometer based on SVD has difficulties in differentiating between translation and rotation. Indeed, instantaneous variations of angles, that is, in the small updating time interval, are perceived as combination of both forward- and cross-range motion. Integration with inertial sensors is expected to substantially reduce these solution ambiguities.

6.5.5 Real-Time Capabilities

The entire algorithm has been tested offline on available radar data. However, since the final aim is to operate it online and in real-time, time duration for the

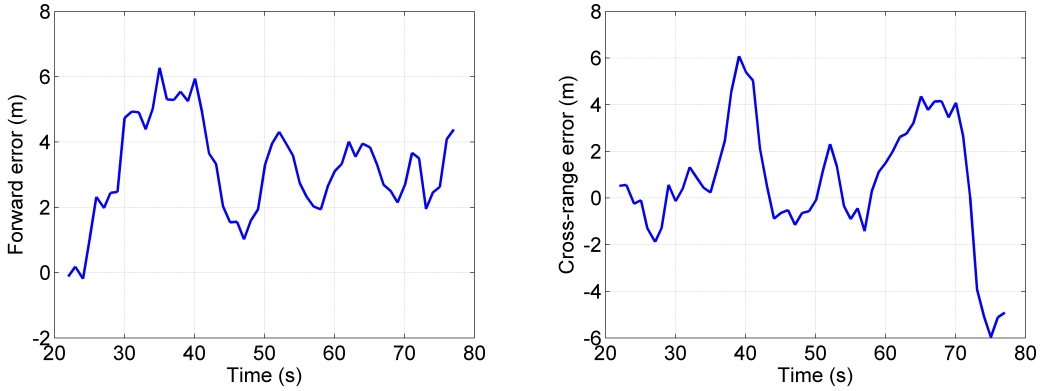

(a) Error in forward direction.

(b) Error in cross-range direction.

Figure 6.24: Errors in Forward-Cross range plane.

whole set of operations at each n-th time step has been analyzed and compared with update frequency f_{upd} of radar data. Table 6.5 lists the duration of each subset. The most time-consuming operation is Multiple-Target Tracking. It is worth noting that time elapsed during MTT strongly depends on the number of outputs transmitted by OS-CFAR.

The overall elapsed time for a single cycle of odometry is $T_{odo} = 0.049$s, that is, $f_{odo} = \dfrac{1}{T_{odo}} \approx 20.4$Hz. The number of time steps for this experimental campaign is $N_{step} = 2710$, that combined with duration leads to an update frequency $f_{upd} = \approx 9$Hz. The comparison of frequencies clearly shows that

$$f_{odo} > f_{upd} \tag{6.21}$$

i.e., odometric information is obtained faster than next set of radar data. Therefore, real time implementation is possible. It must be remarked that these results are valid with reference to Toshiba L855 laptop working in MATLAB® environment, but more efficient algorithm implementation can be foreseen onboard a MAV.

Table 6.5: Offline processing times

Set	Subset	Elapsed Time (ms)
Target Detection	Beat Signal	0.08
	Range FFT	12
	Bearing Estimate	7
	OS-CFAR	3
Multiple-Target Tracking		20
Radar Odometry		7

Chapter 7

Conclusions

Radar sensors have the potential to become a key asset in autonomous operations by mini- and micro-UAS. Sense-and-Avoid, Navigation, and Imaging represent target applications that match with radar features. However, at present time their use is very limited due to very stringent requirements on size, weight and power.

FMCW technology offers a solution to these constraints and allows the use of very simple and cheap technology. This thesis aimed to explore capabilities of radars onboard miniaturized flying platforms. A novel MMW FMCW InSAR has been designed to perform well in each field of autonomous UAS operations. It provides the miniaturized platform with SLAM capabilities, very high 3D resolution and accuracy, and capability to perform real-time onboard processing in order to support autonomous navigation, exploration and mapping in completely unknown and unstructured environments. Simulation environment for the proper assessment of performance in typical scenario provided useful information and suggested actual feasibility of missions. Field tests have been conducted with a 94 GHz SAR at Fraunhofer Institute FHR. At same time commercial ultralight radar has been extensively tested. Multiple-target tracking and radar odometry algorithms have been developed and tested to assess

the potential of radar-aided navigation.

The following novelties have been reached and presented in the thesis:

Design of novel compact mm-wave FMCW InSAR for close-range applications. A novel sensor for operations on mini-UAS has been designed. Since close-range applications hinder the use of well-assessed design processes and approximations, a novel procedure has been developed. Results are encouraging for a practical feasibility.

Analysis of indoor performance of UAS-borne mm-wave FMCW InSAR. Performance of novel mm-wave FMCW InSAR have been analyzed in a simulation environment. As for the design, some approximations, such as parallel rays in SAR Ray Tracing, have been removed and new techniques proposed. Achieved results help with the comprehension of phenomena and design of mission plans.

Radar-aided navigation. A proof-of-concept to navigation with radar odometry proposed. Contrarily to other solutions, the focus is on mini- and micro-UAS and very low altitude scenes, meaning a very cluttered environment. A detailed and critical analysis of the model of radar sensor and the algorithms that have been used is provided. In addition, the entire cycle of radar odometry has been tested during an experimental campaign in a typical scenario with actual data from an existing ultralight radar. The results suggest that the proposed radar-only approach is able to retrieve two-dimensional motion in real-time, even if specific kinds of motion, such as a pure rotation or quasi rotational-only motion, can affect the estimate.

Acknowledgments

Time flew during these last three years. Looking behind me, I can easily picture them as a big jigsaw puzzle to which I added tiles step by step. Clearly, I received a lot of help in completing the picture.

I would like to thank my advisors, Professors Antonio Moccia and Alfredo Renga, for their professional support and for the chance I received to broaden my knowledge. I also want to thank my fellow colleagues and friends, Roberto Opromolla and Amedeo R. Vetrella, with whom I shared a considerably wide part of my PhD path, expectations, joys. Giancarmine Fasano also deserves my deep gratitude. I am especially happy about having been part of Unina Aerospace Systems Football Club (UAS F.C.) for the positive sportive results. But more than that, I enjoyed the possibility to freely share ideas, jokes, thoughts. The whole Aerospace Systems Team needs to be present here, too. Last but not least, thanks to Vittorio Memmolo and Anna Tirri.

My last six months were spent at Fraunhofer Institute FHR, in Wachtberg, with the Millimeterwell und Höchstfrequenzsensoren team. Maybe the coffee there did not work for me, but luckily enough things that matter did. I found a solid group and felt a part of it. Therefore I should say *"vielen Dank"* to Stephan Stanko, Denis Nötel, Axel Hommes and Michael Caris. I also really enjoyed all the conversations during everyday breakfast and lunch with Gregor Biegel, Carsten and Harriet Jacobs, Frank Klöppel, Rolf Schönewald and Yunus Hallac. Even if not cited here, everybody from the team is included. Denis,

Frank, Rainer and Daniel deserve additional huge thanks for their help and efforts with experimental campaigns.

Nominees for best actors and actresses in supporting role: Marco and Gigi, Francesco F., Valeria, Marianna, Ede, Luca D.C., Luca C., Andrea, the Blues Tutors (Francesco and Francesco), India, Mike Tano, Alberto Ci, Jimmy. Well, they all win. Thank you!

I need more than these few lines and little room to thank my family for their continuous support. I am lucky.

Lastly, I feel I deserve special thanks and a smile to a person, *Ale*, with whom I shared a part of my life. She enriched my moments. The events have given us very different paths, but it does not mean that she does not occupies the best place amongst the dear ones.

Bibliography

[1] R. Austin, *Unmanned Aircraft System: UAVS Design, Development and Deployment.* John Wiley & Sons, Ltd: Chichester, UK, 2010.

[2] J. Gundlach, *Designing Unmanned Aircraft Systems: A Comprehensive Approach.* American Institute of Aeronautics and Astronautics, Inc.: Reston, VA, USA, 2012.

[3] K. Dalamagkidis, *Classification of UAVs* in *Handbook of Unmanned Aircraft Systems.* Springer, 2015.

[4] C. De Wagter, S. Tijmons, B.D.W. Remes, and G.C.H.E. de Croon, *Autonomous flight of a 20-gram Flapping Wing MAV with a 4-gram onboard stereo vision system*, Robotics and Automation (ICRA), 2014 IEEE International Conference on, pp. 4982-4987 (2014).

[5] A.R. Vetrella, G. Fasano, A. Renga, and D. Accardo, *Cooperative UAV navigation based on distributed multi-antenna GNSS, vision, and MEMS sensors*, Unmanned Aircraft Systems (ICUAS), 2015 International Conference on, pp. 1128-1137 (2015).

[6] S. Weiss, D. Scaramuzza, and R. Siegwart, *Vision based MAV navigation in unknown and unstructured environments*, Robotics and Automation (ICRA), 2010 IEEE International Conference on, pp. 21-28 (2010).

[7] M. Achtelik, M. Achtelik, S. Weiss, and R. Siegwart, *Onboard IMU and monocular vision based control for MAVs in unknown in- and outdoor environments*, Robotics and Automation (ICRA), 2011 IEEE International Conference on, pp. 3056-3063 (2011).

[8] A.R. Vetrella, A. Savvaris, G. Fasano, and D. Accardo, *RGB-D camera-based quadrotor navigation in GPS-denied and low light environments using known 3D markers*, Unmanned Aircraft Systems (ICUAS), 2015 International Conference on, pp. 185-192 (2015).

[9] D. Accardo, G. Fasano, L. Forlenza, A. Moccia, and A. Rispoli, *Flight test of a radar-based tracking system for UAS sense and avoid*, IEEE Transactions on Aerospace and Electronic Systems, 49, pp.1139-1160 (2013).

[10] E.B. Quist, *UAV Navigation and Radar Odometry*, All Theses and Dissertations. Paper 4439 (2015).

[11] S.M. Duffy, G.A. Brigham, K.S. Newman, P.J. Bell, D.D. Santiago, S.M. Tobin, and J.S. Herd, *Multi-lithic phased array architecture for airborne sense and avoid radar*, Phased Array Systems & Technology, 2013 IEEE International Symposium on, pp.825-830, 15-18 Oct. 2013

[12] E. Itcia, J.-P. Wasselin, S. Mazuel, M. Otten, and A. Huizing, *FMCW Radar for the sense function of sense and avoid systems onboard UAVs.* Proc SPIE 8899, Emerging Technologies in Security and Defence; and Quantum Security II; and Unmanned Sensor Systems X, 889914, (2013).

[13] A. A. Moses, M. J. Rutherford, M. Kontitsis, and K. P. Valavanis, *UAV-borne X-band radar for MAV collision avoidance*, Proc. SPIE 8045, Unmanned Systems Technology XIII, 80450U, (2011).

[14] Available online: http://www.radar-sensor.com/products/radar-modules/sr-1200/

[15] Available online: http://www.timedomain.com/products/pulson-440/

[16] D. Nister, O. Naroditsky, and J. Bergen, *Visual odometry, Computer Vision and Pattern Recognition*, 2004. CVPR 2004. Proceedings of the 2004 IEEE Computer Society Conference on, 1, pp. I-652-I-659 (2004).

[17] E.F. Knott, *Radar Cross Section* in *Radar Handbook*, McGraw Hill, New York (1990).

[18] P. Kopardekar, *Safely Enabling Low-Altitude Airspace Operations: Unmanned Aerial System Traffic Management (UTM)*, (2015) Online: http://ntrs.nasa.gov/archive/nasa/casi.ntrs.nasa.gov/20150006814.pdf

[19] D.K. Barton, and H.R. Ward, *Handbook of Radar Measurements*, Norwood, Mass., Artech House, 1984.

[20] P.E. Howland, H.D. Griffiths, and C.J. Baker. *Passive bistatic radar systems.* In *Bistatic Radars: Emerging Technology*, Wiley, (2008).

[21] A.F. Scannapieco, A. Renga, and A. Moccia, *Preliminary Study of a Millimeter Wave FMCW InSAR for UAS Indoor Navigation*, Sensors, 15 (2), pp. 2309-2335 (2015).

[22] A. Moccia, *Synthetic Aperture Radar* in *Encyclopedia of Aerospace Engineering*, R. Blockley and W. Shyy Eds.; John Wiley & Sons, Ltd.: Chichester, UK, 2010; Volume 5, pp. 1-13.

[23] P.A. Rosen, S. Hensley, I.R. Joughin, F.K. Li, S.N. Madsen, E. Rodriguez, and R.M. Goldstein, *Synthetic aperture radar interferometry.* Proceedings of IEEE, 2000, 88, pp. 331-382.

[24] G. Fornaro, F. Serafino, and F. Soldovieri, *Three-dimensional focusing with multipass SAR data*, Geoscience and Remote Sensing, IEEE Transactions on, vol.41, no.3, pp.507-517, March 2003.

[25] A. Moccia, and A. Renga, *Spaceborne Bistatic Radargrammetry: a robust method for DEM generation*, Synthetic Aperture Radar (EUSAR), 2008 7th European Conference on, pp.1-4, 2-5 June 2008.

[26] E.C. Zaugg, and D. G. Long, *Theory and Application of Motion Compensation for LFM-CW SAR.* Geoscience and Remote Sensing, IEEE Transactions on, 46(10), pp. 2990-2998, Oct. 2008.

[27] J. Hasch, E. Topak, R. Schnabel, T. Zwick, R. Weigel, and C. Waldschmidt, *Millimeter-Wave Technology for Automotive Radar Sensors in the 77 GHz Frequency Band*, IEEE Transactions on Microwave Theory and Techniques, vol. 60, no. 3, pp. 845-860, March 2012.

[28] J. Wenger, *Short range radar - being on the market*, 2007 European Radar Conference, Munich, 2007, pp. 255-258.

[29] Available online: http://www.bosch-mobility-solutions.com/en/products-and-services/passenger-cars-and-light-commercial-vehicles/driver-assistance-systems/predictive-emergency-braking-system/mid-range-radar-sensor-(mrr)/

[30] Available online: http://www.conti-online.com/www/industrial_sensors_de_en/themes/srr20x_en.html

[31] Available online: http://www.bosch-presse.de/pressportal/de/en/bosch-presents-new-radar-sensor-42312.html

[32] Available online: http://www.st.com/content/st_com/en/about/media-center/press-item.html/p3809.html

[33] Available online: http://www.conti-online.com/www/industrial_sensors_de_en/themes/ars_300_en.html

[34] A. Mancini, E. Frontoni, and P. Zingaretti, *Embedded Multisensor System for Safe Point-to-Point Navigation of Impaired Users*, IEEE Transactions on Intelligent Transportation Systems, vol. 16, no. 6, pp. 3543-3555, Dec. 2015.

[35] A. Elfes, J.L. Hall, E.A. Kulczycki, D.S. Clouse, A.C. Morfopoulos, J.F. Montgomery, J.M. Cameron, A. Ansar, and R.J. Machuzak, *Autonomy architecture for Aerobot exploration of Saturnian moon Titan*, IEEE Aerospace and Electronic Systems Magazine, 2008, 23, pp. 16-24.

[36] K. Shrotri, A. Khalid, M.E. Gunduz, K. Manyapu, Y. Fait Sumer, and D.P. Schrage, *Marvin- Near Surface Methane Detection on Mars*, Proceedings of the IEEE Aerospace Conference, Big Sky, MT, USA, 2007; pp. 1-16.

[37] A. Noth, W. Enge, and R. Siegwart, *Recent progresses on the Martian Solar Airplane Sky-Solar*, Proceedings of the 9th ESA Workshop on Advanced Space Technology for Robotics and Automation (ASTRA 2006), ESTEC, Noordwijk, The Netherlands, 2006.

[38] M. Edrich, *Ultra-lightweight synthetic aperture radar based on a 35 GHz FMCW sensor concept and online raw data transmission*, IEE Proceedings of Radar Sonar Navigation, 2006, 153, pp. 129-134.

[39] C.J. Gibbins, and R. Chadha, *Millimetre-wave propagation through hydrocarbon flame*, Proceedings of IEEE, 1987, 134, pp. 169-173.

[40] K. Mphale, and M. Heron, *Absorption and Transmission Power Coefficients for Millimeter Waves in a Weakly Ionised Vegetation Fire*. International Journal of Infrared and Millimeter Waves, 2007, 28, pp. 865-879.

[41] Available online: http://www.ee.sc.edu/classes/Spring14/elct861/Class_Notes/SAND2005-MiniSAR-fact-sheet.pdf.

[42] J.C. Kirk, *Evolution of lite-weight SAR/MTI technology*, Proceedings of IEEE Radar Conference (RadarCon), Pasadena Conference Center, Pasadena, CA, USA, 2009; pp. 1-4.

[43] D. Henke, and E. Meier, *Moving target tracking in single-channel SAR*, Proceedings of the IEEE International Geoscience and Remote Sensing Symposium (IGARSS), Munich, Germany, 2012; pp. 6813-6816.

[44] Available online: http://www.mers.byu.edu/yinsar/microSAR_descrip3.pdf

[45] E. Zaugg, M. Edwards, D. Long, and C. Stringham, *Developments in compact high-performance synthetic aperture radar systems for use on small Unmanned Aircraft*, Proceedings of the IEEE Aerospace Conference, Big Sky, MT, USA, 2011; pp. 1-14.

[46] Available online: http://www.sdl.usu.edu/programs/nusar.pdf

[47] M.L. Wilson, D.L. Von Berg, M. Kruer, N. Holt, S.A. Anderson, D.G. Long, and Y. Margulis, *DUSTER: Demonstration of an Integrated LWIR-VNIR-SAR imaging system*, Proceedings SPIE 6946, Airborne Intelligence, Surveillance, Reconnaissance (ISR) Systems and Applications V, Orlando, FL, USA, 2008.

[48] A. Kinghorn, and A. Nejman, *PicoSAR - An advanced lightweight SAR system.* Proceedings of the European Radar Conference (EuRAD), Rome, Italy, 2009; pp. 168-171.

[49] A.O. Knapskog, S. Brovoll, and B. Torvik, *Characteristics of ships in habour investigated in simultaneous images from TerraSAR-X and PicoSAR.* Proceedings of the IEEE Radar Conference (RadarCon), Marriott Crystal Gateway, Arlington, VA, USA, 2010; pp. 422-427.

[50] P. Almorox-González, J.-T. González-Partida, M. Burgos-García, B.P. Dorta-Naranjo, C. de la Morena-Alvarez-Palencia, and L. Arche-Andradas, *Portable high resolution LFMCW radar sensor in millimeter-wave band.* Proceedings of the International Conference on Sensor Technologies and Applications (SENSORCOMM), Valencia, Spain, 2007; pp. 5-9.

[51] J. González-Partida, P. Almorox-González, M. Burgos-Garcia, and B. Dorta-Naranjo, *SAR System for UAV Operation with Motion Error Compensation beyond the Resolution Cell*, Sensors, 2008, 8, pp. 3384-3405

[52] M. Edwards, D. Madsen, C. Stringham, A. Margulis, B. Wicks, and D. Long, *microASAR: A small, robust LFMCW SAR for operation on UAVs and small aircraft*, Proceedings of the IEEE International Geoscience and Remote Sensing Symposium (IGARSS), Boston, USA, 2008, pp. V-514-V-517.

[53] E. Zaugg, M. Edwards, and A. Margulis, *The SlimSAR: A small, multifrequency, Synthetic Aperture Radar for UAS operation*, Proceedings of the IEEE Radar Conference (RadarCon), Marriott Crystal Gateway, Arlington, VA, USA, 2010; pp. 277-282.

[54] E. Zaugg, and M. Edwards, *Experimental results of repeat-pass SAR employing a visual pilot guidance system*, Proceedings of the IEEE Radar Conference (RadarCon), Atlanta, GA, USA, 2012; pp. 0629-0634.

[55] Available online: http://www.barnardmicrosystems.com/UAV/features/synthetic_aperture_radar.html

[56] Available online: http://www.imsar.com/uploads/files/45_NanoSAR_B_Data_Sheet.pdf.

[57] Available online: http://www.imsar.com/uploads/files/46_NanoSAR_C_Data_Sheet.pdf.

[58] W. Johannes, H. Essen, S. Stanko, R. Sommer, A. Wahlen, J. Wilcke, C. Wagner, M. Schlechtweg, and A. Tessmann, *Miniaturized high resolution Synthetic Aperture Radar at 94 GHz for microlite aircraft or UAV*, Proceedings of the 2011 IEEE Sensors, University of Limerick, Limerick, Ireland, 2011; pp. 2022-2025.

[59] A. Aguasca, R. Acevo-Herrera, A. Broquetas, J.J. Mallorqui, and X. Fabregas, *ARBRES: Light-Weight CW/FM SAR Sensors for Small UAVs*, Sensors , 2013, 13, pp. 3204-3216.

[60] A. Meta, E. Imbembo, C. Trampuz, A. Coccia, and G. De Luca, *A selection of MetaSensing airborne campaigns at L-, X- and Ku-band.* Proceedings of the IEEE International Geoscience and Remote Sensing Symposium (IGARSS), Munich, Germany, 2012; pp. 4571-4574.

[61] E.K. Reedy, and G.W. Ewell, *Millimeter Radar*, in *Infrared and Millimeter Waves, vol. 4*, K.J. Button and J.C. Wiltse, Eds. New York: Academic Press Inc., 1981, pp.23-93.

[62] M. Rüegg, M. Hägelen, E. Meier, and D. Nüesch, *Moving Target Indication with Dual Frequency Millimeter Wave SAR*, Proceedings of IEEE RADAR, pp. 350-357, April 2006.

[63] G.M. Brooker, R. Hennessy, C. Lobsey, M. Bishop, and E. Widzyk-Capehart, *Seeing through dust and water vapor: millimeter wave radar sensors for mining applications*, Journal of Field Robot, vol. 24, pp. 527-557, July 2007.

[64] D. Nüßler, H. Essen, N. von Wahl, R. Zimmermann, S. Rötzel, and I. Willms, *Millimeter wave propagation through dust*, Proc. SPIE 7108, Optics in Atmospheric Propagation and Adaptive Systems XI, October 2008.

[65] M.I. Skolnik, *Millimeter waves and beyond*, in *Introduction to Radar Systems*, F.J. Cerra Ed. Singapore: McGraw-Hill, 1980.

[66] H.D. Griffiths, *New ideas in FM radar*, Electronics & Communication Engineering Journal, 1990, 2, pp. 185-194.

[67] G.M. Brooker, *High Range-Resolution Techniques*, in *Introduction to Sensors for Ranging and Imaging*; SciTech Publishing: 2009; pp. 303-356.

[68] F.T. Ulaby, R.K. Moore, and A.K. Fung, *Microwave remote sensing: Active and Passive, Vol. II – Radar Remote Sensing and Surface Scattering and Emission Theory*, Addison-Wesley, Reading, MA (1982).

[69] A. Meta, P. Hoogeboom, L. Ligthart, *Signal processing for FMCW SAR.* IEEE Transactions on Geoscience and Remote Sensing, 2007, 45, pp. 3519-3532.

[70] A. Meta, *Signal Processing of FMCW Synthetic Aperture Radar Data*, Ph.D. Dissertation, Delft University of Technology, Delft, The Netherlands, 2006.

[71] H.-P. Hou, C.-W. Qu, H.-B. Sun, and R.-G. Song, *Research on FMCW SAR signal characteristic and improved azimuth matched filtering algorithm*, Proceedings of the 2nd Asian-Pacific Conference on Synthetic Aperture Radar (APSAR), Xian, Shanxi, China, 2009; pp. 290-293.

[72] J.C. Curlander, and N.R. McDonough, *The Radar Equation*, in *Synthetic Aperture Radar Systems and Signal Processing*; Wiley-Interscience: New York, NY, USA, 1991; pp. 71-125.

[73] R.E. Collin, *Receiving Antennas*, in *Antennas and Radiowave Propagation*, 4th ed.; McGraw-Hill: New York, NY, USA, 1985; pp. 293-336.

[74] M.I. Skolnik, *Radar Antennas*, in *Introduction to Radar Systems*, 2nd ed.; McGraw-Hill: New York, NY, USA, 1980; pp. 223-277.

[75] G. Franceschetti, and R. Lanari, *Fundamentals*, in *Synthetic Aperture Radar Processing*; CRC Press: Boca Raton, FL, USA, 1999; pp. 1-71.

[76] G.L. Charvat, *Frequency Modulated Continuous Wave (FMCW) Radar*, in *Small and Short-Range Radar Systems*, 1st ed.; CRC Press: 2014; pp. 69-135.

[77] A. F. Scannapieco, A. Renga and A. Moccia, *Performance Analysis of Millimeter Wave FMCW InSAR for UAS Indoor Operations* IEEE International Geoscience and Remote Sensing Symposium 2015 (IGARSS 2015), Milan, July 2015, pp. 806-809.

[78] V. Degli Esposti, F. Fuschini, E. M. Vitucci, and G. Falciasecca *Measurement and Modelling of Scattering From Buildings*, IEEE Transactions on Antennas and Propagation, 2007, 55(1), pp.143-153.

[79] J. Amanatides, and A. Woo, *A fast voxel traversal algorithm for ray tracing*, in Proc. Eurographics, 1987, pp.3-10.

[80] R. Navarro, and E. Moreno-Barriuso, *Laser ray-tracing method for optical testing*, in Opt Lett. 1999; 24: pp. 1-3.

[81] R. Opromolla, G. Fasano, G. Rufino, and M. Grassi, *Uncooperative pose estimation with a LIDAR-based system.* ActaAstronautica, 2015, 110, pp.287-297.

[82] D. Maturana, and S. Scherer, *3D Convolutional Neural Networks for Landing Zone Detection from LiDAR*, in ICRA, 2015.

[83] S. Auer, S. Hinz, and R. Bamler, *Ray-tracing simulation techniques for understanding high-resolution SAR images.* IEEE Transactions on Geoscience and Remote Sensing, 2010, 48(3), pp. 1445-1456.

[84] T. Balz, H. Hammer, and S. Auer, *Potentials and limitations of SAR image simulators – A comparative study of three simulation approaches.* ISPRS Journal of Photogrammetry and Remote Sensing, 2015, 101, pp.102-109.

[85] N. Peinecke, H.-U. Doehler, and B. R. Korn, *Phong-like lighting for MMW radar simulation*, in Proc. SPIE 7117, Millimetre Wave and Terahertz Sensors and Technology, 71170M, 2008.

[86] L. Subrt, P. Pechac, and S. Zvanovec. *New Approach to Modeling of Diffuse Reflection and Scattering for Millimeter-wave Systems in Indoor Scenarios*, PIERS Online, 2010, 8(6), pp.719-722.

[87] C. W. Trueman, R. Paknys, J. Zhao, D. Davis, and B. Segal, *Ray tracing algorithm for indoor propagation*, in Proc 16th Annual Review of Progress in Applied Computational Electromagnetics, Monterey, CA., 2000, pp. 493-500.

[88] K.H. Ng, E.K. Tameh, and A.R. Nix, *A new hybrid geometrical optics and radiance based scattering model for ray tracing applications*, in Communications, 2005. ICC 2005. 2005 IEEE International Conference on, 2015, pp. 2168-2172.

[89] R.G. Kouyoumjian, *Asymptotic High-Frequency Methods*, Proceedings of IEEE,Vol.53, No. 8, pp. 864-876, August 1965.

[90] F.E. Nicodemus, J.C. Richmond, J.J. Hsia, I.W. Ginsberg, and T. Limperis, *Geometrical Considerations and Nomenclature for Reflectance, issued by U.S. Department of Commerce, National Bureau of Standards*, 1977.

[91] M. Moallem, and K. Sarabandi, *Polarimetric Study of MMW Imaging Radars for Indoor Navigation and Mapping.* IEEE Transactions on Antennas and Propagation, 2014, 62(1), pp.500-504.

[92] K. Sato, H. Kozima, H. Masuzawa, T. Manabe, T. Ihara, Y. Kasashima, and K. Yamaki, *Measurements of reflection characteristics and refractive indices of interior construction materials in millimeter-wave bands*, Vehicular Technology Conference, 1995 IEEE 45th, 1995, pp.449-453.

[93] T. Teshirogi and T. Yoneyama, *Millimeter-Wave Propagation*, Modern Millimeter-wave Technologies. Tokyo: Ohmsha Ltd, 1999, pp.127-164.

[94] A. Moccia, S. Vetrella, and S. Ponte, *Passive and Active Calibrators Characterization by using a Spaceborne SAR System Simulator*, IEEE Transactions on Geoscience and Remote Sensing, 1994, 32(3), pp.715-721.

[95] A. Ribalta, *Time-Domain Reconstruction Algorithms for FMCW-SAR*, Geoscience and Remote Sensing Letters, IEEE, 8(3), pp. 396-400, May 2011.

[96] R. Bamler, *A comparison of Range-Doppler and Wavenumber Domain SAR Focusing Algorithms*, Geoscience and Remote Sensing, IEEE Transactions on, 30(4), pp. 706-713, Jul 1992.

[97] R. Wang, O. Loffeld, H. Nies, S. Knedlik, M. Hagelen, and H. Essen. *Focus FMCW SAR Data Using the Wavenumber Domain Algorithm*, Geoscience and Remote Sensing, IEEE Transactions on, 48(4), pp. 2109-2118, April 2010.

[98] A.F. Yegulalp, *Fast backprojection algorithm for synthetic aperture radar*, Radar Conference, 1999. The Record of the 1999 IEEE, pp. 60-65, 1999.

[99] D.A. Ausherman, A. Kozma, J.L. Walker, H.M. Jones, and E.C. Poggio, *Developments in radar imaging*, Aerospace and Electronic Systems, IEEE Transactions on, AES-20(4), pp. 363-400, July 1984.

[100] D.C. Munson, Jr., J.D. O'Brien, and W.K. Jenkins, *A tomographic formulation of spotlight-mode synthetic aperture radar*, Proceedings of the IEEE, 71(8), pp. 917-925, Aug 1983.

[101] H. Hellsten, and L.E. Andersson, *An inverse method for the processing of synthetic aperture radar data*, Inverse Problems, 3(1), pp. 111-124, 1987.

[102] D. Meng, D. Hu, and C. Ding, *Precise Focusing of Airborne SAR Data With Wide Apertures Large Trajectory Deviations: A Chirp Modulated Back-Projection Approach*, Geoscience and Remote Sensing, IEEE Transactions on, 53(5), pp. 2510-2519, May 2015.

[103] I.G. Cumming, and F.H. Wong. *Digital Processing of Synthetic Aperture Radar Data: Algorithms and Implementation*. Artech House. 2005.

[104] J. Mittermayer, A. Moreira, and O. Loffeld, *Spotlight SAR data processing using the frequency scaling algorithm*, Geoscience and Remote Sensing, IEEE Transactions on, 37(5), pp. 2198-2214, Sep 1999.

[105] R. Sullivan, *Synthetic aperture radar*, in *Radar Handbook*; Skolnik, M.I., Ed.; McGraw-Hill: New York, NY, USA,2008; pp. 17.1-17.37.

[106] A. Moccia, and A. Renga, *Spatial Resolution of Bistatic Synthetic Aperture Radar: Impact of Acquisition Geometry on Imaging Performance*, IEEE Transactions on Geoscience and Remote Sensing, 2011, 49, pp. 3487-3503.

[107] A. Thiele, E. Cadario, K. Schulz, U. Thoennessen, and U. Soergel, *Building recognition from multi-aspect high-resolution InSAR data in urban areas*, IEEE Transactions on Geoscience and Remote Sensing, 2007, 45, pp. 3583-3593.

[108] A. F. Scannapieco, A. Renga, and A. Moccia, *Compact Millimeter Wave FMCW InSAR for UAS Indoor Navigation*, Metrology for Aerospace (MetroAeroSpace), 2015 IEEE, pp.551-556, June 2015.

[109] M. Caris et al., *mm-Wave SAR demonstrator as a test bed for advanced solutions in microwave imaging*, in IEEE Aerospace and Electronic Systems Magazine, vol. 29, no. 7, pp. 8-15, July 2014.

[110] H. Gulan, C. Rusch, S. Beer, T. Zwick, M. Kuri, and A. Tessmann, *Lens coupled broadband slot antenna for W-band imaging applications*, 2013 IEEE Antennas and Propagation Society International Symposium (APSURSI), Orlando, FL, 2013, pp. 424-425.

[111] Available online: https://www.rcgroups.com/forums/showthread.php?2071772-DJI-NAZA-Phantom-A2-CAN-bus-communication-protocol-NazaCanDecoder-Arduino-library

[112] Available online: https://www.pjrc.com/teensy/teensy31.html

[113] Available online: https://www.xsens.com/products/mti-g-710/

[114] W. Simon, T. Klein, and O. Litschke, *Small and light 24 GHz multi-channel radar*, Antennas and Propagation Society International Symposium (APSURSI), 2014 IEEE, pp. 987-988 (2014).

[115] A. F. Scannapieco, A. Renga and A. Moccia, *Investigation on radar-based applications for mini-UAS and MAVs*, 2016 17th International Radar Symposium (IRS), pp. 1-6 (2016).

[116] A. F. Scannapieco, A. Renga, G. Fasano and A. Moccia, *Ultralight radar sensor for autonomous operations by micro-UAS*, 2016 International Conference on Unmanned Aircraft Systems (ICUAS), pp. 727-735 (2016).

[117] J. Zhang, and S. Singh, *Low-drift and Real-time Lidar Odometry and Mapping*, Autonomous Robots. vol. 41, no. 2, pp. 401–416, 2017.

[118] K. Kauffman, J. Raquet, Y.T.J. Morton, and D. Garmatyuk, *Real-time UWB-OFDM radar-based navigation in unknown terrain*, IEEE Transactions on Aerospace and Electronic Systems, 49(3), pp. 1453–1466 (2013).

[119] E. Quist, and R. Beard, *Radar Odometry on Fixed-Wing Small Unmanned Aircraft*, IEEE Transactions on Aerospace and Electronic Systems, 52(1), pp. 396 - 410 (2016)

[120] E. Quist, P. Niedfeldt, and R. Beard, *Radar Odometry with Recursive-RANSAC*, IEEE Transactions on Aerospace and Electronic Systems, 52(4), pp. 1618 - 1630 (2016).

[121] D. Scaramuzza and F. Fraundorfer, *Visual Odometry Part I: The First 30 Years and Fundamentals*, IEEE Robotics & Automation Magazine, (2011).

[122] S. Kohlbrecher, O. von Stryk, J. Meyer, and U. Klingauf, *A flexible and scalable slam system with full 3d motion estimation*, 2011 IEEE International Symposium on Safety, Security, and Rescue Robotics, pp. 155-160 (2011).

[123] F. Steinbrücker, J. Sturm, and D. Cremers, *Real-Time Visual Odometry from Dense RGB-D Images*, 2011 IEEE International Conference on Computer Vision Workshops (ICCV Workshops), pp. 719 - 722 (2011).

[124] E. De Lellis, F. Corraro, G. Greco, G. Fasano, and D. Accardo, *Exploiting Forward Looking Radar Measurements and Digital Map Data Fusion for Altimetry Estimation during Low-altitude Flight*, Infotech@Aerospace, (2011).

[125] C.E. Cook, and M. Bernfeld, *Radar Signals, An Introduction to Theory and Application*, Artech House (1993).

[126] A.V. Oppenheim, A.S. Willsky, and S.H. Nawab, *Signals and systems*. Prentice-Hall, (1983).

[127] S. Blackman, and R. Popoli, *Design and Analysis of Modem Tracking Systems*, Artech House, Boston (1999).

[128] H. Rohling, *Radar CFAR Thresholding in Clutter and Multiple Target Situations*, IEEE Transactions on Aerospace and Electronic Systems, AES-19 (4), pp. 608 - 621 (1983).

[129] H. Rohling, *Some radar topics: Waveform Design, Range CFAR and Target Recognition*, Advances in Sensing with Security Applications, pp. 293-322, Springer Netherlands, (2006).

[130] L.M. Novak, *Radar target detection and map-matching algorithm studies*, IEEE Transactions on Aerospace and Electronics Systems, AES-16, pp. 620 625 (1980).

[131] V.C. Hansent, and J.H. Sawyers, *Detectability loss due to 'greatest of' selection in a cell-averaging CFAR*, IEEE Transactions on Aerospace and Electronics Systems, AES-16, pp. 115-118 (1980).

[132] J.D. Moore, and N.B. Lawrence, *Comparison of two CFAR methods used with square law detection of Swerling I targets*, IEEE International Radar Conference. Washington, D.C., (1980).

[133] M. Weiss, *Analysis of some modified cell averaging CFAR proecssors in multiple-target situations*, IEEE Transactions on Aerospace and Electronics Systems, AES-18, pp. 102-114 (1982).

[134] G.V. Trunk, *Range resolution of targets using automatic detectors*, IEEE Transactions on Aerospace and Electronics Systems, AES-14, pp. 750-755 (1978).

[135] J.T. Rickard, and G.M. Dillard, *Adaptive detection algorithms for multiple-target situations*, IEEE Transactions on Aerospace and Electronics Systems, AES-13, pp. 338-343 (1977).

[136] G.M. Dillard, and J.T. Rickard, *A distribution-free Doppler processor*, IEEE Transactions on Aerospace and Electronics Systems, 26, pp. 479-486 (1974).

[137] S. Blackman, *Multiple hypothesis tracking for multiple target tracking*, IEEE Aerospace and Electronic Systems Magazine, 19 (1), pp. 5-18 (2004).

[138] Y. Bar-Shalom, and X.-R. Li, *Estimation and Tracking: Principles, Techniques and Software*, Artech House, Dedham, MA (1993).

[139] J. Munkres, *Algorithms for the Assignment and Transportation Problems*, Journal of the Society of Industrial and Applied Mathematics, 5, pp. 32-38 (1957).

[140] F. Bourgeois, and J.-C.Lassalle, *An Extension of the Munkres Algorithm for the Assignment Problem to Rectangular Matrices*, Communications of the ACM, 14 (12), pp. 802-804 (1971).

[141] R.S. Bucy, and P.D. Joseph, *Filtering for Stochastic Processes with Applications to Guidance*, Interscience Publishers, New York (1968).

[142] E.D. Kaplan and C. Hegarty, *Understanding GPS: Principles and Applications*, Artech House (2005).